Jean-Sebastian Tempel

Nonlinearities in Semiconductor Microcavities: A Correlation Spectroscopy Study

Nonlinearities in Semiconductor Microcavities: A Correlation Spectroscopy Study

Dissertation

presented to the Faculty of Physics of the
TU Dortmund University, Germany,
in partial fulfilment of the requirements for the degree of

Doktor rer. nat.

by

Jean-Sebastian Tempel

technische universität
dortmund

Dortmund, November 2012

Accepted by the Faculty of Physics of the TU Dortmund University, Germany.

Day of the oral examination: 31st January 2013

Examination board:
Prof. Dr. Manfred Bayer (primary reviewer)
Prof. Dr. Carsten Westphal (secondary reviewer)
Prof. Dr. Götz S. Uhrig
Dr. Bärbel Siegmann

Contents

Chapter 1

Motivation

Since the first realisation of a laser half a century ago [Mai60], optical technologies have made enormous progress. Today, coherent light sources are used as powerful tools in many different areas of research, such as the natural and life sciences [Dud12, Muq11]. Furthermore, advances in academic and industrial research have led to innumerable applications of laser devices, e.g. in the fields of medicine, entertainment, and industrial material treatment.

However, the area in which high-quality laser sources are of essential relevance is the domain of modern telecommunication, i.e. optical data transmission. The importance of this technology was recently emphasised, when the Nobel Prize in Physics 2009 was partly awarded to Charles K. Kao, pioneer in the development of fibre optics [Kao66]. In order to couple this technology to common electronic circuits, optoelectronic devices are required. These devices are generally based on semiconductor lasers. The advances in semiconductor technology, especially with respect to epitaxial growth methods, have led to the development of miniaturised laser devices using semiconductor nanostructures, in particular quantum wells, as gain material [Tel90]. The most prominent outcome of these research efforts is the vertical-cavity surface-emitting laser (VCSEL) [Cho97]. Recently, it has been shown that data-transfer rates of 100 Gbit/s can be achieved by using a single VCSEL device [Rod12]. Nevertheless, the growing demand for broadband internet services in all areas of everyday life continues to drive a worldwide increase of network traffic. Accordingly, there is a need to develop optical networks able to process larger data volumes at higher speeds. Faster optoelectronic circuits, in turn, require improved sources of coherent radiation with lower operating currents. A number of different approaches can be considered to achieve this.

In order to achieve stable lasing operation, population inversion has to be established inside the whole active medium. Consequently, one viable way to lower the threshold-carrier density of microcavity lasers is to further reduce the dimensionality of the gain medium. The use of self-assembled quantum dots, embedded in the resonator during epitaxial growth, turns out to be very promising [Led11]. In quantum dots, charge carriers are confined in all three dimensions, leading to discrete

energy levels. As a result, quantum-dot lasers are assumed to provide stable output characteristics over a wide range of temperatures. Furthermore, the β-factor, i.e. the spontaneous emission rate of a quantum dot into the lasing mode divided by the total spontaneous emission into all available modes, can be substantially enhanced in a quantum-dot microresonator laser [Yam91]. This strongly increases the efficiency and, consequently, lowers the threshold-carrier density of microcavity lasers. The general drawback of high-β lasers lies in the difficulty to exactly identify the threshold, as the typical kink in the input-output curve becomes smoother and finally disappears in the ultimate case of $\beta = 1$, which would provide the thresholdless laser [Bjö91].

While quantum-dot lasers typically operate in the weak-coupling regime, another possibility to further reduce the threshold-carrier density is to use quantum-well microcavities in the strong-coupling regime. In this regime, energy is continuously exchanged between excitons in the quantum well and photons in the cavity [Khi06]. As a result, mixed states of light and matter are created which form new eigenmodes of the coupled system: microcavity polaritons [Wei92]. These quasi-particles are composite bosons. Under specific conditions, they are known to undergo a phase transition similar to Bose-Einstein condensation and accumulate in large numbers in the ground state. Due to their photonic content, polaritons have a small effective mass, which in principle allows for condensation at temperatures up to room temperature in certain material systems [Chr07, Lu12]. Such a polariton condensate is completely phase-coherent. Thus, it is expected to act as a coherent light source without the need for population inversion. It is called the polariton laser [Ima96].

In the framework of this thesis, both approaches mentioned above are investigated. First, the emission from pillar-shaped microcavities using quantum dots as optically active material is considered. To this end, the lasing transition is analysed in terms of the excitation-power dependent emitted intensity and the degree of linear polarisation. The first-order as well as the second-order correlations of the emission are also evaluated. In this way, the coherence time τ_c and the photon statistics of the emitted light field are determined. It is shown that a nonlinearity in τ_c can be used to identify the threshold. Moreover, a theoretical model is introduced which connects first-order and second-order correlations. Hence, a full characterisation of the lasing transition of GaAs-based micropillars is given. Second, a quantum-well microresonator operating in the strong-coupling regime is examined. It is demonstrated that the different emission regimes of such a microcavity—thermal emission, polariton lasing, and photon lasing—are separated by two distinct thresholds. These two nonlinearities are observed in different quantities, i.e. the main emission intensity and energy, the energy-dispersion relation, as well as the emission-pulse duration. A special emphasis is placed on photon correlations, allowing to determine the degree of second-order coherence of the cavity emission. Using a recently introduced photon-correlation spectroscopy technique, the degree of coherence is quantified across the different emission regimes of a microcavity-polariton system. Furthermore, the temperature-dependence of pulsed polariton lasing is analysed.

This thesis is organised as follows. First, the theoretical background describing

the interaction of light and matter in microcavities is provided in chapter 2. This chapter also contains an introduction to optical correlation functions, which are used to characterise different states of light emitted by the microcavity samples. The applied experimental methods, i.e. Michelson interferometry, Fourier-plane imaging and photon-correlation spectroscopy, are presented in chapter 3. In the subsequent chapters, the results of the experimental studies are discussed: in chapter 4, the lasing transition of GaAs-based quantum-dot micropillar lasers is characterised. In chapter 5, the two-threshold behaviour of a quantum-well microcavity is demonstrated. Finally, a summary of the main results of this thesis combined with an outlook is given in chapter 6.

Chapter 2

Theoretical Background

The characteristics of semiconductor light sources can be efficiently controlled in different ways. Within the present thesis, the coupling strength of light and matter in semiconductor microcavities is of major importance. Two possible regimes will be treated: In chapter 4, the investigations on a weakly coupled micropillar resonator system will be discussed. In chapter 5, a study of a planar microcavity in the strong coupling regime will be presented. In order to adequately describe the experimental results, the current chapter provides the corresponding theoretical background.

This chapter is organised as follows. First, basic electronic and optical properties of semiconductor nanostructures, which are used as optically active material in semiconductor microresonators, are presented in section 2.1. Second, the fundamental physics of semiconductor microcavities are discussed in section 2.2. The interaction of both, carrier eigenstates in nanostructures and the light field inside a resonator, is treated in section 2.3. Finally, the main methods applied in this work to characterise states of light, i.e. the system of optical correlation functions, is described in section 2.4.

2.1 Semiconductor Nanostructures

Many electronic and optical properties of semiconductor materials can be described by their electronic band structure. Probably the most prominent parameter of semiconductor band structures is the energy gap E_{gap} between the valence band (VB) maximum and the conduction band (CB) minimum. In the context of this work, materials based on the III-V compound semiconductors gallium arsenide (GaAs) and aluminium arsenide (AlAs) are investigated. While both GaAs and AlAs condense in the zincblende structure, they differ significantly in their energy band-gap.[1] However, as their lattice constants are similar, these two semiconductors are well suited for

[1] While GaAs exhibits a band-gap energy of about $E_{\mathrm{gap}}^{\mathrm{GaAs}} = 1.42\,\mathrm{eV}$ at room temperature, the band-gap of AlAs is $E_{\mathrm{gap}}^{\mathrm{AlAs}} \approx 3\,\mathrm{eV}$ at 300 K. The lattice constants of GaAs and AlAs are $a_{\mathrm{GaAs}} = 5.65\,\text{Å}$ and $a_{\mathrm{AlAs}} = 5.66\,\text{Å}$, respectively. Data taken from references [Ada85] and [Kri91].

high-quality epitaxial growth using almost arbitrary percentages x in $Ga_{1-x}Al_xAs$ [Gru06].

In this section the reader is reminded of the basic electronic properties of semiconductors in general (subsection 2.1.1) and occurring peculiarities when the dimensionality is reduced (subsection 2.1.2). The discussion is focused on the properties of GaAs-based compound semiconductors and follows the textbooks by Gaponenko [Gap98], Grundmann [Gru06], Klingshirn [Kli05], and Weisbuch [Wei91], unless specified otherwise.

2.1.1 Carrier eigenstates in semiconductors

In order to describe the properties of electrons in a solid with its $\sim 10^{23}$ atoms, one has to account for Coulomb interactions with all other electrons as well as with the lattice ions. This generally results in a computational problem being ab-initio unsolvable in explicit form, as the number of particles and the overall degrees of freedom are simply too large. It is however possible to decouple the initial hierarchy of N coupled one-particle equations by considering the collective effects of carriers and nuclei as an average crystal potential $U_{\mathrm{ave}}(\vec{r})$. A simplified form of the single-particle Hamiltonian H can then be written as

$$H\psi = \left[-\frac{\hbar^2}{2m}\nabla^2 + U_{\mathrm{ave}}(\vec{r})\right]\psi = E\psi \ . \tag{2.1}$$

Taking further into account the periodicity of the crystal, the electron energy-eigenfunctions can be described by a product of a lattice-periodic wave function $u_{n,\vec{k}}(\vec{r})$ modulated by a plane wave [Ash76]:

$$\psi_{n,\vec{k}}(\vec{r}) = e^{i\vec{k}\vec{r}}u_{n,\vec{k}}(\vec{r}) \ . \tag{2.2}$$

Here, n denotes the band index. The solutions given by equation (2.2) are generally known as Bloch waves.

When calculating the band structure of a semiconductor, the particular crystal symmetry is of great importance. As mentioned above, GaAs and alloys of the form $Ga_{1-x}Al_xAs$ crystallise in the zincblende structure; they consist of two interpenetrating face-centred-cubic lattices. GaAs is a direct band-gap semiconductor, meaning that the lowest CB energy and the highest VB energy occur at the same crystal momentum $\vec{k}$, namely at the centre of the Brillouin zone (Γ-point) [Ash76]. The conduction band has a parabolic form around the Γ-point, and electrons can thus be described as quasi-particles with an effective mass m_{e}^* which is inversely proportional to the curvature of the CB. As the Bloch wave function has an s-type symmetry, the CB in GaAs and AlAs is two-fold degenerate due to the two possible realisations of the electron spin.

The valence band, on the other hand, has a p-type symmetry with angular momentum $L = 1$, which results in a six-fold degeneracy. The band with total angular

momentum $J = 1/2$, however, is split from the band with $J = 3/2$ due to spin-orbit effects. Furthermore, the valence band with $J = 3/2$ has an underlying fine structure:[2] When the crystal momentum is along the z-axis, the angular momentum can be quantised along z. Further, except at the Γ-point, the band $|J = 3/2, J_z = 1/2\rangle$ and the band $|J = 3/2, J_z = 3/2\rangle$ split due to their different effective masses. Here, the band $|J = 3/2, J_z = 1/2\rangle$ with lighter effective mass m^*_{lh} is called the light hole (lh), while the band $|J = 3/2, J_z = 3/2\rangle$ with heavier effective mass m^*_{hh} is denominated as the heavy hole (hh). In this thesis, only these two valence sub-bands will be considered.

2.1.2 Carrier eigenstates in low-dimensional structures

With the technological progress of epitaxial growth techniques, such as molecular beam epitaxy (MBE) and metalorganic vapour phase epitaxy, semiconductor materials can be fabricated with atomic monolayer precision. These advances gave birth to low-dimensional heterostructures such as two-dimensional quantum wells (QWs), one-dimensional quantum wires, and finally zero-dimensional quantum dots (QDs). In these nanostructures the motion degree of freedom of charge carriers is constrained in one or more dimensions on the order of their thermal de Broglie wavelength,

$$\lambda^{\mathrm{dB}}_{\mathrm{e,h}} = 2\pi\hbar \left[3 m^*_{\mathrm{e,h}} k_{\mathrm{B}} T\right]^{-(1/2)} \ . \tag{2.3}$$

Here, k_{B} denotes the Boltzmann constant and T the carrier temperature. Consequently, due to the confinement, the carrier eigenstates change significantly. Quantisation effects become prominent, which manifest particularly in the density of states, which in turn specifies the number of available carrier eigenstates within an infinitesimal interval $\mathrm{d}E$ around a certain energy E. The dependence of the density of states $D(E)$ of CB electrons on the dimensionality is reflected in the following equations:

$$D_{\text{3-dim}}(E) = \frac{1}{2\pi^2}\left(\frac{2m^*_{\mathrm{e}}}{\hbar^2}\right)^{3/2} \sqrt{E - E_{\mathrm{CB}}} \ , \tag{2.4a}$$

$$D_{\text{2-dim}}(E) = \frac{m^*_{\mathrm{e}}}{\pi\hbar^2} \sum_i \Theta(E - E_{\mathrm{CB}} - \Delta E_i) \ , \tag{2.4b}$$

$$D_{\text{1-dim}}(E) = \frac{1}{\pi}\left(\frac{2m^*_{\mathrm{e}}}{\hbar^2}\right) \sum_i \left[\frac{n_i \Theta(E - E_{\mathrm{CB}} - \Delta E_i)}{\sqrt{E - E_{\mathrm{CB}} - \Delta E_i}}\right] \ , \tag{2.4c}$$

$$D_{\text{0-dim}}(E) = \sum_i n_i \delta(E - E_{\mathrm{CB}} - \Delta E_i) \ . \tag{2.4d}$$

The dimensionality-dependent quantisation effect is further illustrated in figure 2-1. Within the framework of this thesis, microcavity systems with type-I QDs as well as systems using type-I QWs as optically active material are investigated.[3] While the density of states is described by a sum of step functions in the case of a QW, it is given by delta peaks in the case of a QD.

[2] For details on the fine structure of the hole bands, see, e.g., the discussion in reference [Wei91].

[3] The evolution of the band-gap energy of type-I nanostructures is shown schematically in panel (b) of figure 2-2. Here, both the electron and the hole are confined inside the QW layer. In

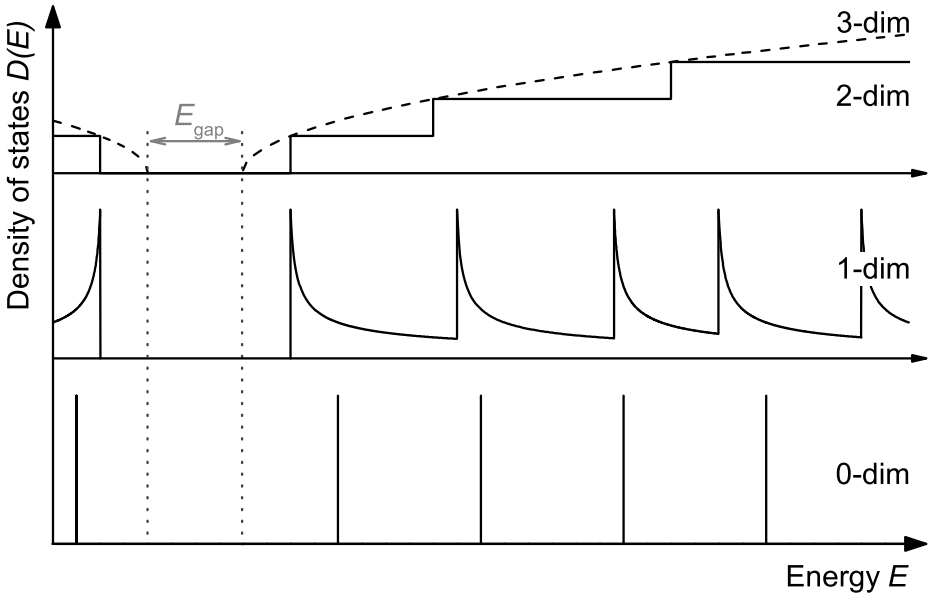

Figure 2-1: Schematic illustration of the electronic density of states for various dimensionality. Figure is adapted from reference [Gap98].

Semiconductor quantum wells

A semiconductor quantum well is typically formed by growing a thin film of a material A with energy band-gap $E_{\mathrm{gap}}^{\mathrm{A}}$ between two layers of material B with larger energy band-gap $E_{\mathrm{gap}}^{\mathrm{B}}$. The layer sequence and the evolution of the band-gap energy of such a heterostructure are shown schematically in figures 2-2(a) and 2-2(b), respectively. In such a QW, the wave function of the CB electron reads

$$\psi_{\vec{k}}^{\mathrm{A,B}}(\vec{r}) = \exp\left\{ i\vec{k}_{||} \cdot \vec{r} \right\} \; u_{n,\vec{k}}^{\mathrm{A,B}}(\vec{r}) \; \chi_n(z) \; , \tag{2.5}$$

where $u_{n,\vec{k}}^{\mathrm{A,B}}(\vec{r})$ is the Bloch wave function of the carrier in material A or B, and z is the growth direction of the structure. Inside the QW plane, the electron can move freely. Here, its wave function is described by a plane wave with a direction of propagation $k_{||}$. The envelope function $\chi_n(z)$ indicates the influence of the barrier layers and is assumed to vary slowly with z. $\chi_n(z)$ satisfies a Schrödinger equation which takes into account both the particular effective electron mass and the individual position of the CB minimum in the different materials A and B. In such a QW structure, the solutions for the confined electron wave functions are characterised by a sinusoidal form inside the QW and an exponential decay outside the QW layer.

Due to the QW confinement potential both the CB minimum and the VB maximum are shifted, resulting in a larger energy band-gap $E_{\mathrm{gap}}^{\mathrm{A,QW}}$ as compared to the bulk case $E_{\mathrm{gap}}^{\mathrm{A,BULK}}$. This is illustrated in panel (c) of figure 2-2. Also, the hh and lh bands are known to split at the Γ-point, which is a result of the different confinement

heterostructures with type-II band alignment, however, the evolution of the band-gap energy is described by a staggered gap and, thus, electron and hole will localise in different materials [Gru06, Vas99, Wei91].

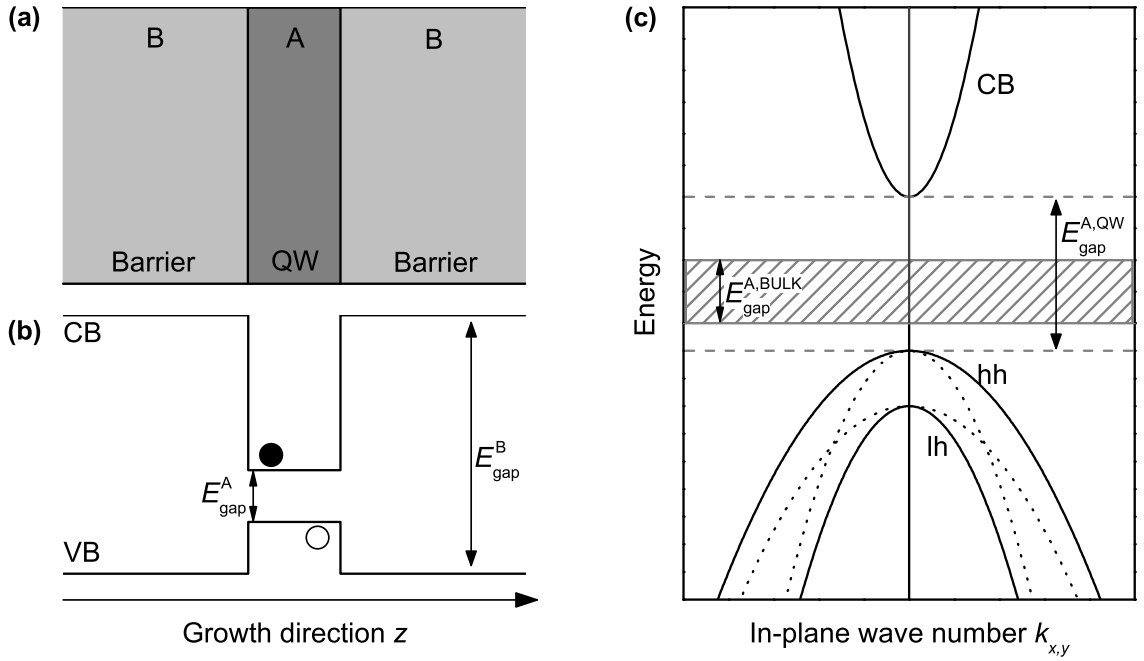

Figure 2-2: Schematic illustration of a type-I quantum-well structure. Panel (a) shows a typical barrier-QW-barrier layer structure. The corresponding evolution of the energy gap E_{gap} along the structure growth direction is sketched in panel (b): The QW material A with smaller energy gap $E^{\mathrm{A}}_{\mathrm{gap}}$ is sandwiched between the barrier material B with larger energy gap $E^{\mathrm{B}}_{\mathrm{gap}}$. A conduction-band electron (valence-band hole) captured by the QW confinement potential is shown as filled (open) circle. A sketch of the two-dimensional zincblende QW band structure is presented in panel (c). The band-gap energy $E^{\mathrm{A,QW}}_{\mathrm{gap}}$ is larger in the QW as compared to the energy gap $E^{\mathrm{A,BULK}}_{\mathrm{gap}}$ in bulk material due to the confinement. Also, the degeneracy of the two hole bands is lifted for $k_{x,y} = 0$ due the different hh and lh confinement energies in growth direction of the QW. In a first approximation, the hh has a lighter in-plane mass as the lh (dotted lines). In general, these two bands anti-cross, resulting in the bands shown as solid lines, as described by the so-called Luttinger Hamiltonian [Kli05, Wei91].

energies in growth direction for hh and lh. Furthermore, in a first approximation, the hh band exhibits a smaller in-plane mass $m^{x,y}_{\mathrm{hh}}$ than the lh band, as depicted by the dotted lines. Typically, these two bands anti-cross at some finite in-plane wave number $k_{x,y}$, forming the hh and lh bands shown by the solid lines in figure 2-2(c).[4]

As can be depicted from panel (b) of figure 2-2, electrons and holes can be trapped inside such a QW layer, and, thus, the electron and hole wave functions overlap. Consequently, the Coulomb interaction between electrons and holes has to be considered in order to adequately describe their dynamics, especially with respect to radiative recombination processes. When an electron in the CB and a hole (say a hh) in the VB are bound by their Coulomb interaction, they are typically referred to as com-

[4]Note that, in general, the VB fine structure of a GaAs/AlGaAs QW is much richer. However, a full description is beyond the scope of this thesis. A detailed discussion of the QW-VB fine structure can be found, e.g., in reference [Cha85].

pound quasi-particle, called the exciton.[5] Essentially, an exciton in a QW can be described by the same equations as the two-dimensional hydrogen atom.[6] Here, the problem can be separated into the centre of mass motion and the relative motion of the constituents. While the centre of mass motion is characterised by plane waves, the relative motion problem is more complex. It requires solving a one-body problem in a Coulomb potential, where the reduced mass $1/m_{\mathrm{X}}^{*} = 1/m_{\mathrm{e}}^{*} + 1/m_{\mathrm{h}}^{*}$ of the exciton has to be taken into account. In a perfectly two-dimensional environment, this results in the $1s$-state of the exciton being described by a wave function

$$\psi_{1s}(r_{\text{e-h}}) = \frac{1}{\alpha_{1s}\sqrt{2\pi}} \exp\left\{-\frac{r_{\text{e-h}}}{2\alpha_{1s}}\right\} , \tag{2.6}$$

where the QW exciton Bohr radius reads

$$\alpha_{1s} = \frac{1}{2}\frac{m_0}{m_{\mathrm{X}}^{*}}\epsilon_r a_{\mathrm{B}} = 0.5 \cdot \alpha_{1s}^{\text{3-dim}} . \tag{2.7}$$

Here, m_0 is the free electron mass and a_{B} is the Bohr radius of the hydrogen atom. The relative distance between the electron and the hole is given by $r_{\text{e-h}}$. The exciton binding energy is then calculated to be

$$E_{\mathrm{b},1s}^{\mathrm{QW}} = -\frac{4}{\epsilon_r^2}\frac{m_{\mathrm{X}}^{*}}{m_0}\frac{m_0 e^4}{(4\pi\epsilon_0\hbar)^2} \approx 4E_{\mathrm{b}}^{\text{3-dim}} , \tag{2.8}$$

where the third term is identified as the atomic Rydberg energy $E_{\mathrm{Ry}} = 13.6\,\mathrm{eV}$. For two-dimensional excitons, the theoretically possible binding energy is thus about four times larger than in the case of excitons in bulk semiconductors.

From equations (2.7) and (2.8), the exciton Bohr radius and binding energy in a GaAs QW are calculated to be $\alpha_{1s} \approx 11\,\mathrm{nm}$ and $|E_{\mathrm{b},1s}^{\mathrm{QW}}| \approx 21\,\mathrm{meV}$, respectively.[7] These parameter values would be true if the QW exciton was perfectly two-dimensional. Due to the finite QW barrier height, however, the exciton wave function spreads in z direction. In the QW microcavity sample investigated in this work, the GaAs/AlAs QWs have a thickness of 7 nm. Their exciton binding energy is assumed to be $|E_{\mathrm{b},1s}^{\mathrm{QW}}| \approx 10\,\mathrm{meV}$. Due to this increased binding energy as compared to the bulk excitons, the QW exciton is less susceptible to ionisation. In contrast to the case of a GaAs bulk crystal, it is therefore possible to measure excitonic photoluminescence in GaAs QWs at temperatures up to room temperature [Che88].

[5] In the present work, the excitons are typically so-called Wannier-Mott excitons, characterised by a relatively large exciton Bohr radius compared to the lattice constant. In contrast to Wannier-Mott excitons, Frenkel excitons appear if electron and hole are localised at the same lattice atom. This is usually the case in ionic crystals as well as in molecular solids [Kop07].

[6] While the three-dimensional hydrogen atom is a standard textbook example, the mathematical treatment of the limiting case of a two-dimensional hydrogen atom is not. A detailed discussion of the two-dimensional problem can be found, e.g., in the appendix of reference [Rou11].

[7] Here, the effective masses $m_{\mathrm{e}}^{*} = 0.067m_0$ and $m_{\mathrm{h}}^{*} = 0.5m_0$ as well as a permittivity of $\epsilon_r = 12.4$ were used. Parameters taken from reference [Li00].

For experiments where a quantum well is embedded in a microcavity,[8] the energy dispersion relation of a QW exciton with respect to its in-plane momentum is of particular interest. Using the electron and hole dispersions in parabolic approximation, the dispersion of a QW exciton at small $k_{x,y}$ values is given by

$$E_{\mathrm{X}}^{\mathrm{QW}}(k_{x,y}) = E_{\mathrm{gap}}^{\mathrm{QW}} + E_{\mathrm{e}}^{\mathrm{QW}} + E_{\mathrm{h}}^{\mathrm{QW}} + E_{\mathrm{b},1s}^{\mathrm{QW}} \tag{2.9}$$

$$\approx E_{\mathrm{X}}^{\mathrm{QW}}(0) + \frac{\hbar^2 k_{x,y}^2}{2m_{\mathrm{X}}^*} \ . \tag{2.10}$$

However, in the experimentally accessible $k_{x,y}$-range of typically a few inverse micrometres, the exciton dispersion can be assumed to be essentially flat.

Semiconductor quantum dots

While smooth and flat interfaces are desirable to optimise QWs, the actual lattice constant mismatch of different semiconductor materials is the key to the self-assembled growth of semiconductor quantum dots. The most important method to fabricate high-quality self-assembled QDs, especially with respect to GaAs-based materials, is the Stranski-Krastanov process [Leo94, Leo98]: Using a GaAs substrate, monolayers of a material with smaller band-gap energy, like (In,Ga)As, are deposited subsequently, creating the so-called wetting layer. As soon as the wetting layer reaches a critical thickness, the strain in the layer surface is minimised by developing distinct islands. With further deposition of InAs monolayers, these islands start to grow until they reach a height of several nanometres. Typically, the QDs are then covered with a thick layer of GaAs. In a simplified picture, the evolution of the band-gap energy in all three dimensions can thus be described as shown in panel (b) of figure 2-2.

In GaAs-based materials, such self-organised QDs typically reveal a shape close to cylindrical lateral symmetry along with a strong in-plane carrier confinement [Bay02]. This means, that the QD radius r_{QD} is smaller than the exciton Bohr radius $\alpha_{1s}^{\mathrm{QD}}$. In an idealised picture of a perfectly spherical QD, the exciton can be described taking the Coulomb interaction and the dot confinement potential $U(r)$ into account. This results in the Hamiltonian

$$H_{\mathrm{X}}^{\mathrm{QD}} = -\frac{\hbar^2}{2m_{\mathrm{e}}^*}\nabla^2 - \frac{\hbar^2}{2m_{\mathrm{h}}^*}\nabla^2 - \frac{e^2}{\epsilon|\vec{r}_{\mathrm{e}} - \vec{r}_{\mathrm{h}}|} + U^{\mathrm{QD}}(r) \tag{2.11}$$

It leads to a ground electron-hole pair state ($1s1s$) energy, which in terms of the three-dimensional exciton Rydberg energy $E_{\mathrm{Ry}}^* = E_{\mathrm{Ry}} \cdot m_{\mathrm{X}}^*/(\epsilon_r^2 m_0)$ reads[9]

$$E_{1s,1s}^{\mathrm{QD}} = E_{\mathrm{gap}} + \pi^2 \left(\frac{\alpha_{1s}^{\mathrm{QD}}}{r_{\mathrm{QD}}}\right)^2 E_{\mathrm{Ry}}^* - 1.786\frac{\alpha_{1s}^{\mathrm{QD}}}{r_{\mathrm{QD}}}E_{\mathrm{Ry}}^* - 0.248E_{\mathrm{Ry}}^* \ . \tag{2.12}$$

[8] Compare section 2.3 of this chapter. Experimental results obtained on a microcavity with embedded quantum wells are discussed in chapter 5.

[9] It should be noted that equation (2.12) is only valid in the limit $r_{\mathrm{QD}} \ll a_{\mathrm{B}}$. Furthermore, note that equation (2.12) does not account for the fact that holes are typically of p-type symmetry in GaAs-based materials, as mentioned in section 2.1.1. For a detailed discussion of the electron-hole pair ground-state energy, please refer to chapter 2 of reference [Gap98] and references given therein.

The creation of excitonic states in QDs can be realised by excitation of carriers through optical or electrical pumping into the continuum of barrier states. Subsequently, the carriers are captured into the confinement potential of the QDs. Due to fast non-radiative relaxation processes on a typical time scale of a picosecond [Gie07], the carriers finally occupy the lowest-energy shell states inside the QDs. The lowest state in (In,Ga)As-based quantum dots, whose energy can be approximated by equation (2.12), is composed of combinations of the electron with spin $S_{\mathrm{e},z} = \pm 1/2$ and the heavy-hole state with spin $S_{\mathrm{hh},z} = \pm 3/2$.

The ground-state emission spectrum from a single semiconductor QD can be described by a Lorentzian profile with $E^{\mathrm{QD}}_{1s,1s}$ as centre energy. The width ΔE^{QD} of this emission line is directly related to the lifetime τ_{X} of the exciton by $\Delta E^{\mathrm{QD}} \approx \hbar/\tau_{\mathrm{X}}$. However, when ensembles of QDs are studied, the emission spectrum is generally broadened as individual QDs differ in size, shape and material composition due to the growth technique. The emission spectrum is then characterised by a Gaussian envelope function.

In general, there are several other aspects which have to be considered when describing the emission spectra as well as the carrier dynamics, e.g. biexcitons, charged QD states, and exchange interactions [Bay99, Bry90, Hin01]. These topics, however, go beyond the scope of the present thesis.

2.2 Semiconductor Microcavities

Optical semiconductor microcavities are characterised by their resonator length being of the order of the wavelength λ_{cav} for which they are designed. These resonators have been fabricated and studied in many different geometries, such as microdiscs, microspheres, photonic crystal cavities as well as Bragg resonators.[10] In this thesis, microcavities based on Bragg resonators are investigated. The corresponding physical concepts are presented in this section. The discussion follows Savona et al. [Sav95], unless indicated otherwise.

2.2.1 Bragg resonators

In principle, a Bragg resonator is a Fabry-Pérot-style optical resonator, i.e. two planar mirrors facing each other at a distance L_{cav}. With n_{cav} being the refractive index of the medium inside the cavity, the free spectral range $\Delta\lambda$ between adjacent longitudinal cavity modes is given by

$$\Delta\lambda = \frac{\lambda^2}{2 n_{\mathrm{cav}} L_{\mathrm{cav}}} \ . \tag{2.13}$$

In a macroscopic resonator with this geometry ($L_{\mathrm{cav}} \gg \lambda$), the different cavity modes are closely spaced. However, when $L_{\mathrm{cav}} \sim \lambda_{\mathrm{cav}}/n_{\mathrm{cav}}$ as in a microcavity, the modes

[10] For a general overview on microcavities, see, e.g., the publications by Kavokin et al. [Kav07] and Vahala [Vah03] and references given therein.

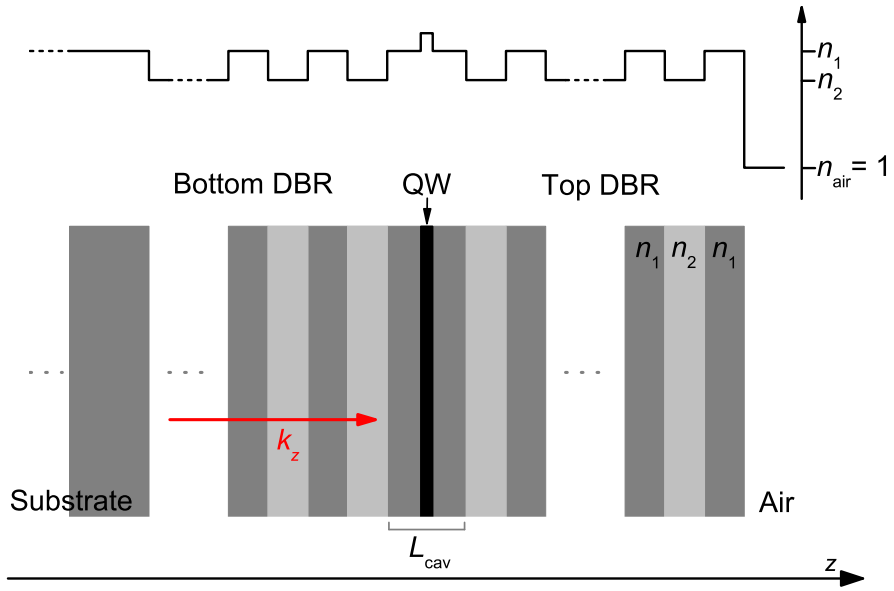

Figure 2-3: Schematic illustration of an optical Bragg resonator containing a single QW as optically active medium at the centre of the half-wavelength cavity layer. The black horizontal arrow indicates the direction of growth z, which coincides with the direction of hindered photon propagation k_z (red arrow). The top and bottom DBR mirrors are made of alternating layers of two different semiconductor materials with unequal indices of refraction n_1 and n_2, respectively. The evolution of the refractive index is shown at the top. In this example, the cavity layer with thickness $L_{\mathrm{cav}} = \lambda/2$ is made from the same material as the substrate. It should be noted that, while this illustration shows a QW embedded in the cavity layer, the discussion in section 2.2 is strictly speaking only valid for an empty microcavity. This figure is adapted from reference [Den10].

are spectrally strongly separated, which essentially allows single-mode emission.

In such a Bragg resonator, the mirrors are realised by so-called distributed Bragg reflectors (DBRs). A schematic diagram of such a microresonator is shown in figure 2-3. The DBR surrounding the central cavity consists of periodic stacks of two $\lambda_{\mathrm{Br}}/4$ layers with different refractive indices, where λ_{Br} is the Bragg design wavelength. In the samples studied in this thesis these layers are typically made of GaAs (refractive index n_{GaAs}) and AlAs (n_{AlAs}). In that way, the DBR creates a photonic band gap, the so-called stopband. It is characterised by a spectral range of high reflectivity around λ_{Br}. The stopband is accompanied by oscillating side-lobes on either side of the reflection spectrum. In the theoretical case of an infinite DBR stack, the spectral width $\Delta\lambda_{\mathrm{SB}}$ of the stopband can be approximated by [Yeh88]

$$\Delta\lambda_{\mathrm{SB}} \approx \frac{4\lambda_{\mathrm{Br}}}{\pi} \arcsin\left(\frac{n_{\mathrm{GaAs}} - n_{\mathrm{AlAs}}}{n_{\mathrm{GaAs}} + n_{\mathrm{AlAs}}}\right) . \tag{2.14}$$

It results in $\Delta\lambda_{\mathrm{SB}} \approx 100\,\mathrm{nm}$ when supposing a resonance wavelength of $\lambda_{\mathrm{cav}} = 850\,\mathrm{nm}$. The transmission of photons propagating in the direction of the DBR periodicity, which is usually the growth direction of the resonator, is thus suppressed and photons

are efficiently reflected. The maximum peak reflectivity of the DBR stack is calculated by

$$R = 1 - \frac{4}{n_{\mathrm{cav}}} \left(\frac{n_{\mathrm{AlAs}}}{n_{\mathrm{GaAs}}} \right)^{2N} , \tag{2.15}$$

and thus depends on both the refractive index contrast ($n_{\mathrm{AlAs}}/n_{\mathrm{GaAs}}$) and the number of quarter-wave layer pairs N. The latter is also connected to the quality factor of the cavity, Q. In terms of the experimentally accessible emission spectrum, the cavity Q-factor can be approximated by

$$Q = \frac{\lambda_{\mathrm{cav}}}{\Delta\lambda_{\mathrm{cav}}} , \tag{2.16}$$

with $\Delta\lambda_{\mathrm{cav}}$ being the spectral width of the cavity mode.

In such a Bragg microresonator, the electromagnetic field inside the cavity can be described as a standing wave with antinodes at the centre of the cavity as well as at the interface of the cavity layer to the DBR stack. Accordingly, this wave penetrates into the Bragg structure up to a penetration depth which is given by

$$L_{\mathrm{DBR}} = \frac{\lambda_{\mathrm{cav}}}{2n_{\mathrm{GaAs}}} \cdot \frac{n_{\mathrm{AlAs}} n_{\mathrm{GaAs}}}{n_{\mathrm{GaAs}} - n_{\mathrm{AlAs}}} . \tag{2.17}$$

This results in a total effective cavity length of $L_{\mathrm{eff}} = L_{\mathrm{cav}} + L_{\mathrm{DBR}}$. Moreover, as a consequence of possible growth imperfections, the stopband center frequency ω_{SB} and the frequency ω_{cav} corresponding to L_{cav} are not necessarily identical. In general, the resonant frequency of the Bragg resonator then reads [Pan99]

$$\omega_{\mathrm{res}} = \frac{\omega_{\mathrm{cav}} L_{\mathrm{cav}} + \omega_{\mathrm{SB}} L_{\mathrm{DBR}}}{L_{\mathrm{eff}}} . \tag{2.18}$$

In a microcavity structure as shown in figure 2-3, a photon is confined only along the growth axis z. Consequently, a cavity photon will show an energy dispersion, which can be described by

$$E_0(k) = \frac{\hbar c}{n_{\mathrm{cav}}} \sqrt{\left(\frac{2\pi}{L_{\mathrm{cav}}} \right)^2 + k_{||}^2} , \tag{2.19}$$

where $k_{||}$ is the photon in-plane wave vector. This dispersion has a parabolic shape for small $k_{||}$, thus describing an effective photon mass $m_{\mathrm{cav}} = h n_{\mathrm{cav}}/(c L_{\mathrm{cav}})$. This effective mass is known to be in the order of $10^{-5}\, m_0$ [Whi96]. Moreover, the energy dispersion relation given in equation (2.19) has the advantage that it can easily be accessed experimentally: The angle of the emission from the microcavity (θ) is directly related to the photon in-plane wave vector by $k_{||} = k \sin(\theta)$.

2.2.2 Micropillar cavities

In a Bragg resonator as described in the previous subsection, in-plane photon states are unaffected by the cavity confinement. However, in order to further reduce the mode volume, it is necessary to confine photons in the lateral direction as well. This

is usually achieved by further processing of a planar Bragg resonator: Using reactive ion etching techniques, pillar-like structures with almost arbitrary cross-section can be realised [Löf05, Rei07].

In this thesis, only micropillar cavities with nominally circular cross-section are examined. The calculation of the corresponding cavity modes is thus a problem with rotational symmetry. As a result, the energy of the fundamental as well as higher-order modes is highly dependent on the diameter d of the pillar [Gut98]:

$$E_{n_\phi,n_r} = \sqrt{E_0^2 + \frac{\hbar^2 c^2}{n_{\text{cav}}^2} \frac{x_{n_\phi,n_r}^2}{[d/2]^2}} \ . \tag{2.20}$$

Here, x_{n_ϕ,n_r} is the n_r-th zero of the Bessel function $J_{n_\phi}(x_{n_\phi,n_r} r/[d/2])$ [Abr72], and $E_0 = \hbar c k_0 / n_{\text{cav}}$ gives the quantisation energy in the direction of growth z, as it follows from equation (2.19). It is thus possible to shift the mode spectrum into the blue by reducing the pillar diameter.

Such a cylindrically shaped pillar microcavity exhibits distinct features. The rotational symmetry of its emission, e.g., makes it favourable for coupling into optical fibres. Moreover, the free-spectral range between adjacent lateral modes can be further increased when decreasing the pillar diameter. Thereby higher-order modes may shift out of the high-reflectivity stopband. However, when the micropillar cross-section is perfectly circular, a drawback lies in the two-fold degeneracy of the fundamental emission mode. This can deteriorate the polarisation stability of micropillar lasers. A study of the polarisation and coherence properties of micropillar lasers with QDs as active material will be presented in chapter 4.

2.3 Coupling of Light and Matter in Semiconductor Microcavities

As implied in the schematic illustration of a Bragg resonator shown in figure 2-3, a semiconductor nanostructure such as a quantum well or a quantum dot can be embedded in a microcavity and thus be used as optically active medium. In order to maximise cavity-induced effects, the nanostructure is generally positioned at an antinode of the intra-cavity electromagnetic field distribution, i.e. at the centre of the cavity layer in the case of a half-wavelength cavity as shown in figure 2-3. The main operation characteristics of the microcavity are then strongly influenced by the coupling strength between excitons in the nanostructure and the fundamental cavity-photon mode. In principle, one has to distinguish between the regimes of strong and weak light-matter coupling.

The basic concepts of light-matter interaction are presented in this section. The discussion follows essentially the publications by Kavokin et al. [Kav07] and by Deng et al. [Den10], unless indicated otherwise.

2.3.1 Weak coupling in microcavities

The regime of weak coupling is characterised by the alteration of the spontaneous emission (SE) rate of an optically active emitter embedded in a microcavity, which is generally known as the Purcell effect [Pur46].

The Purcell effect can theoretically be described by perturbation theory, i.e. by the use of Fermi's golden rule. Consider an optical emitter characterised by an electric dipole $\vec{d}$ which interacts with the electromagnetic field $\vec{E}(\vec{r},t)$ at position $\vec{r}$ and time t. If the emission energy of the emitter is given by $\hbar\omega_{\mathrm{em}}$, the SE rate of that emitter, γ_{sp}, can be written as

$$\gamma_{\mathrm{sp}} = \frac{1}{\tau_{\mathrm{sp}}} = \frac{2\pi}{\hbar^2}\left|\vec{d}\cdot\vec{E}(\vec{r},t)\right|^2 \cdot \rho_{\mathrm{vac}}(\omega_{\mathrm{em}}) \ . \tag{2.21}$$

Here, $\rho_{\mathrm{vac}}(\omega_{\mathrm{em}})$ is the density of states of the electromagnetic field in the vacuum, evaluated at the specific frequency of the emitter. In general, for a mode volume V and an index of refraction n it is given by:

$$\rho_{\mathrm{vac}}(\omega) = \frac{\omega^2 V n^3}{\pi^2 c^3} \ . \tag{2.22}$$

The electromagnetic field inside a resonator, however, is altered. Considering a microcavity with fundamental mode frequency ω_{cav} and a quality factor of $Q = \omega_{\mathrm{cav}}/\Delta\omega_{\mathrm{cav}}$, the photon density of states reads:

$$\rho_{\mathrm{cav}}(\omega) = \frac{2}{\pi}\frac{\Delta\omega_{\mathrm{cav}}}{4(\omega-\omega_{\mathrm{cav}})^2 + \Delta\omega_{\mathrm{cav}}^2} \ . \tag{2.23}$$

As a consequence, the spontaneous emission rate into the cavity mode ω_{cav} is changed as well. In comparison to the SE rate into the vacuum, it is enhanced by a factor of

$$F_{\mathrm{p}} = \frac{3}{4\pi^2}\cdot\frac{\lambda_{\mathrm{cav}}^3}{n_{\mathrm{cav}}^3}\cdot\frac{Q}{V_{\mathrm{eff}}} \ , \tag{2.24}$$

where V_{eff} is the effective mode volume, and λ_{cav} and n_{cav} are the design wavelength and the effective index of refraction of the microcavity, respectively. The factor F_{p} given by equation (2.24) is known as the Purcell factor. The influence of the altered photonic density of states is sketched in figure 2-4: In the case of an emitter (QD1) being in resonance with the cavity-photon field, the SE rate is enhanced, i.e. its emission line broadened. For an off-resonant emitter (QD2), the SE rate remains unchanged as in vacuum. Thus, by tailoring the photon field as by enclosing it in a microresonator, the emission from an optically active medium can be used more efficiently to generate optical gain.

Microcavities operating in the weak coupling regime are often used to realise low-threshold lasing operation [Bjö94, McC92, Rei08]. A large Purcell factor can be used to increase the so-called β-factor of the lasing mode, which is defined as the SE rate into that specific mode divided by the total SE into all available resonator modes. In

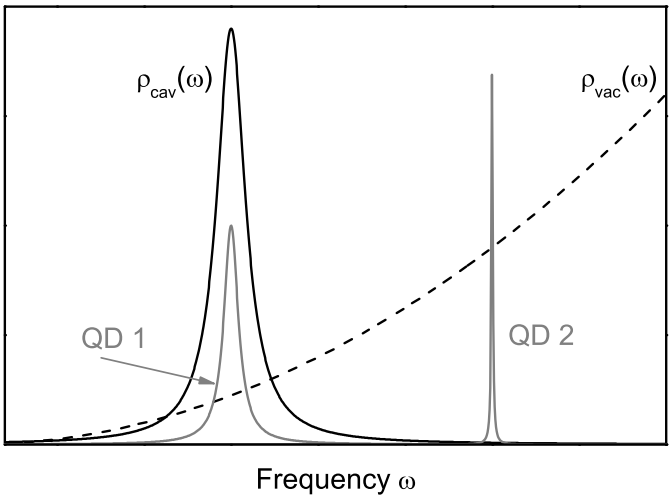

Figure 2-4: Photon density of states in the vacuum $\rho_{\mathrm{vac}}(\omega)$ (dashed black) compared to a microcavity single mode $\rho_{\mathrm{cav}}(\omega)$ (solid black). The Lorentzian emission lines of two quantum dots are sketched for two different cases. In the case of QD1, the emitter is in resonance with the cavity mode, and its spontaneous emission rate is enhanced. In the case of QD2, the emitter is strongly detuned with no final state to decay to. Consequently, the lifetime of QD2 is increased, corresponding to a narrow emission line. Figure is adapted from reference [Kav07].

a microresonator, the β-factor can reach values close to unity. This has a significant influence on the emission characteristics of the microcavity, i.e. its lasing threshold becomes more difficult to identify [Ric94, Yam91]. A thorough characterisation of the lasing threshold of pillar-shaped Bragg microresonators with high Q-factors and high β-factors is the main topic of the experimental study presented in chapter 4.

2.3.2 Strong coupling in microcavities

If the Q-factor of a microcavity is high enough, it is possible that a photon which has been emitted into the resonator is re-absorbed by the optically active medium. In such a case, a description of the system using perturbation theory and Fermi's golden rule is no longer valid. Instead, the coupling between the cavity-photon field and the electronic excitation in the nanostructure has to be considered. Consequently, the system is then denoted to be in the regime of strong coupling. In this section, the nanostructure embedded in the microcavity is assumed to be a quantum well, as illustrated in figure 2-3.

Using the so-called rotating wave approximation, the Hamiltonian of a microcavity containing a QW is composed of the individual Hamilton operators of the quantum-well exciton and the cavity photon, $\hat{H}_{\mathrm{X}}$ and $\hat{H}_{\mathrm{C}}$, respectively. In addition, the coupling of photon and exciton has to be accounted for. If the direction of growth of the cavity—and thus the direction of photonic confinement—is assumed to be in z-direction, only the in-plane dynamics corresponding to a wave vector $k_{||}$ are essential.

Using $k = k_{||}$ for simplicity, the Hamiltonian then reads[11]

$$\begin{aligned}\hat{H} = &\quad \hat{H}_{\mathrm{X}} &+ &\quad \hat{H}_{\mathrm{C}} &+ &\quad \hat{H}_{\mathrm{coupling}} \\ = &\sum_k E_{\mathrm{X}}(k)\, \hat{a}_k^\dagger \hat{a}_k &+ &\sum_k E_{\mathrm{C}}(k)\, \hat{b}_k^\dagger \hat{b}_k &+ &\sum_k \hbar g(k) \left(\hat{a}_k^\dagger \hat{b}_k + \hat{a}_k \hat{b}_k^\dagger\right) \ . \end{aligned} \tag{2.25}$$

Here, $\hat{a}_k^\dagger$ and $\hat{a}_k$ are the creation and annihilation operators of an exciton with in-plane wave vector k. Accordingly, $\hat{b}_k^\dagger$ and $\hat{b}_k$ are the photonic counterparts. The exciton-photon coupling is given by

$$\hbar g(k) = \mu_{cv} \varphi_{1s} \sqrt{E_{\mathrm{C}}(k) / \left(2\epsilon_0 \epsilon_r\right)} \ , \tag{2.26}$$

where μ_{cv} is the dipole matrix element describing the interaction of electron and hole, and φ_{1s} is the Fourier transformed envelope function of the 1s-exciton [compare equation (2.6)]. The coupling term $\hbar g(k)$ is non-zero only between modes with the same in-plane wave vector.

The creation and annihilation operators of the photon mode are obviously bosonic. Provided that the operators $\hat{a}_k^\dagger$ and $\hat{a}_k$ obey the bosonic algebra as well, i.e. $[\hat{a}_k \hat{a}_k^\dagger] = 1$, the Hamiltonian in equation (2.25) can be diagonalised. For that purpose, a so-called Hopfield transformation is applied, which defines new operators $\hat{p}_k$ and $\hat{q}_k$:

$$\hat{p}_k \equiv X_k \hat{a}_k - C_k \hat{b}_k \ , \tag{2.27a}$$

$$\hat{q}_k \equiv C_k \hat{a}_k + X_k \hat{b}_k \ . \tag{2.27b}$$

Here, the Hopfield coefficients C_k and X_k are introduced. As a result of the diagonalisation procedure, the microcavity Hamiltonian can be re-written as

$$\hat{H} = \sum_k E_{\mathrm{UP}}(k)\, \hat{q}_k^\dagger \hat{q}_k + \sum_k E_{\mathrm{LP}}(k)\, \hat{p}_k^\dagger \hat{p}_k \ . \tag{2.28}$$

The operators $(\hat{p}_k^\dagger, \hat{p}_k)$ and $(\hat{q}_k^\dagger, \hat{q}_k)$ describe the creation and annihilation operators of new eigenstates of the system. These new quasi-particles are called the upper polariton (UP) and lower polariton (LP), according to the two branches of higher and lower eigenenergies, respectively.[12] Their energy dispersion relations are denoted as $E_{\mathrm{UP}}(k)$ and $E_{\mathrm{LP}}(k)$ and are deduced from the diagonalisation as

$$E_{\mathrm{UP,LP}}(k) = \frac{1}{2}\left[E_{\mathrm{X}}(k) + E_{\mathrm{C}}(k)\right] \pm \frac{1}{2}\sqrt{\Delta_k^2 + 4\left[\hbar g(k)\right]^2} \ . \tag{2.29}$$

The splitting between the two polariton branches is thus dependent on the light-matter interaction strength $2\hbar g$ as well as on the detuning between the energies of the bare cavity mode and the bare exciton state given by

$$\Delta_k \equiv E_{\mathrm{C}}(k) - E_{\mathrm{X}}(k) \ . \tag{2.30}$$

[11] It should be noted that in the present description different spin states as well as other states than the 1s-exciton are neglected.

[12] The term polariton in general refers to an interacting system of a photon with another quasi-particle. The latter can be any optically accessible excitation of matter, e.g. a phonon, a plasmon or a magnon. A more general overview on polaritonic systems can be found, e.g., in reference [Kli05]. Within this thesis, the term polariton refers solely to exciton-polaritons in quantum-well Bragg resonators.

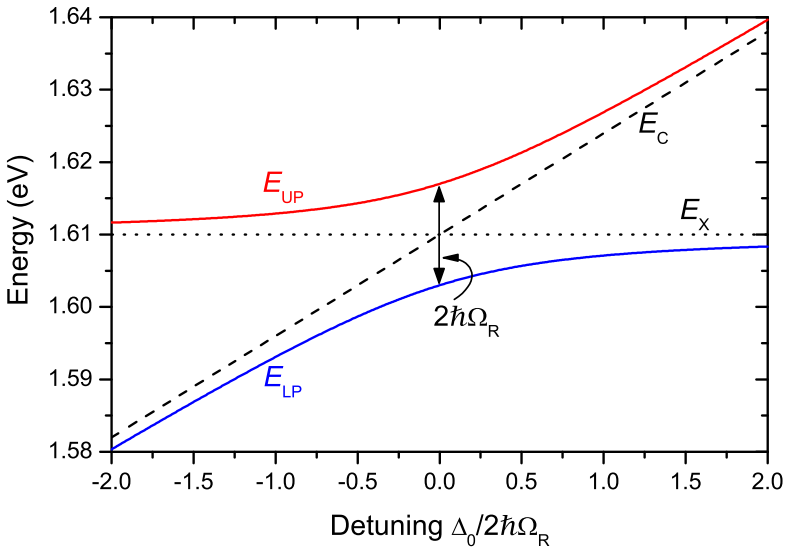

Figure 2-5: Energy levels of the upper and lower polaritons at zero in-plane wave vector as a function of the cavity-exciton detuning Δ_0. The polariton energies E_{UP} (red line) and E_{LP} (blue line) are obtained using equation (2.29). Parameters ($E_{\mathrm{X}} = 1.610\,\mathrm{eV}$, $2\hbar g(0) = 2\hbar\Omega_{\mathrm{R}} = 14\,\mathrm{meV}$) are chosen in order to match those of the microcavity sample examined in chapter 5. The energy dispersions of the cavity-photon and the bare exciton are shown as dashed and dotted lines, respectively.

As an example, the detuning dependence of the UP and LP energy levels at $k = 0$ is shown in figure 2-5, using parameters of $E_{\mathrm{X}} = 1.610\,\mathrm{eV}$ and $2\hbar g(0) = 14\,\mathrm{meV}$. These parameters are chosen in order to match those of the microcavity sample examined in chapter 5.

As a result, a polariton can be described as a linear superposition of a cavity photon and a semiconductor exciton, both having the same in-plane wave vector k. The bare photon and exciton modes are hence only transient states that periodically exchange their energy. The average photonic and excitonic fractions of a polariton are then given by the amplitude squared of the Hopfield coefficients, $|C_k|^2$ and $|X_k|^2$, which satisfy the relation $|C_k|^2 + |X_k|^2 = 1$. These coefficients can be calculated by

$$|C_k|^2 = \frac{E_{\mathrm{UP}}(k)E_{\mathrm{X}}(k) - E_{\mathrm{LP}}(k)E_{\mathrm{C}}(k)}{[E_{\mathrm{C}}(k) + E_{\mathrm{X}}(k)]\sqrt{\Delta_k^2 + 4\,[\hbar g(k)]^2}} = \frac{1}{2}\left(1 - \frac{\Delta_k}{\sqrt{\Delta_k^2 + 4\,[\hbar g(k)]^2}}\right), \tag{2.31a}$$

$$|X_k|^2 = \frac{E_{\mathrm{UP}}(k)E_{\mathrm{C}}(k) - E_{\mathrm{LP}}(k)E_{\mathrm{X}}(k)}{[E_{\mathrm{C}}(k) + E_{\mathrm{X}}(k)]\sqrt{\Delta_k^2 + 4\,[\hbar g(k)]^2}} = \frac{1}{2}\left(1 + \frac{\Delta_k}{\sqrt{\Delta_k^2 + 4\,[\hbar g(k)]^2}}\right). \tag{2.31b}$$

In the case of the LP, its excitonic fraction is given by $|X_k|^2$, while its photonic fraction is given by $|C_k|^2$. In the case of the UP, the behaviour is opposite.

Example dispersion relations $E_{\mathrm{UP,LP}}(k)$ and the corresponding amplitude-squared Hopfield coefficients are shown in figure 2-6 for different values of the cavity-photon detuning Δ_0. Here, the following observations can be made. The general behaviour at larger k is found to be independent of the detuning: In that case, the LP asymptotically follows the bare exciton dispersion, while the UP asymptotically follows the bare cavity-photon dispersion. At negative detuning, the LP has a higher photon fraction around $k = 0$, while the UP has a larger exciton fraction. In contrast to this, the LP is more exciton-like at positive detuning, while the UP is more photon-like. In the special case of the cavity and the exciton modes being in resonance, i.e. $E_{\mathrm{C}}(0) = E_{\mathrm{X}}(0)$ (middle column of figure 2-6), the squared Hopfield coefficients are $|C_0|^2 = |X_0|^2 = 1/2$. Thus, both the LP and the UP are exactly half-photon and half-exciton at zero in-plane momentum. As can be seen from the example dispersion curves, the actual value of the detuning at $k = 0$ has a strong influence on the curvature of the dispersion relations.

In the optically accessible momentum space around $k = 0$, the polariton dispersions can be approximated by parabolic functions as

$$E_{\mathrm{LP,UP}}(k) \approx E_{\mathrm{LP,UP}}(0) + \frac{\hbar^2 k^2}{2m_{\mathrm{LP,UP}}} \ . \tag{2.32}$$

Thereby, the effective masses of the LP and UP are defined. They can be expressed by the exciton and cavity-photon masses, m_{X} and m_{C}, as follows:

$$\frac{1}{m_{\mathrm{UP}}} = \frac{|C_0|^2}{m_{\mathrm{X}}} + \frac{|X_0|^2}{m_{\mathrm{C}}} \ , \tag{2.33a}$$

$$\frac{1}{m_{\mathrm{LP}}} = \frac{|X_0|^2}{m_{\mathrm{X}}} + \frac{|C_0|^2}{m_{\mathrm{C}}} \ . \tag{2.33b}$$

As the effective photon mass is generally much lighter than the effective mass of the exciton, $m_{\mathrm{C}} \ll m_{\mathrm{X}}$, the polariton masses can be approximated by

$$m_{\mathrm{UP}} = m_{\mathrm{C}}/|X_0|^2 \ , \tag{2.34a}$$

$$m_{\mathrm{LP}} = m_{\mathrm{C}}/|C_0|^2 \ . \tag{2.34b}$$

It is worth noting that the effective mass of the LP is of the order of $m_{\mathrm{LP}} \sim 10^{-4} m_{\mathrm{X}}$ and, thus, much lighter than the exciton mass. This will be of major importance when treating polariton lasing in chapter 5.

In the same way as the Hopfield coefficients affect the polariton effective masses, they also have a significant influence on the lifetime of the polariton states. The lifetimes of polaritons with wave vector k are given by

$$\frac{1}{\tau_{\mathrm{UP},k}} = \frac{|C_k|^2}{\tau_{\mathrm{X},k}} + \frac{|X_k|^2}{\tau_{\mathrm{C},k}} \ , \tag{2.35a}$$

$$\frac{1}{\tau_{\mathrm{LP},k}} = \frac{|X_k|^2}{\tau_{\mathrm{X},k}} + \frac{|C_k|^2}{\tau_{\mathrm{C},k}} \ . \tag{2.35b}$$

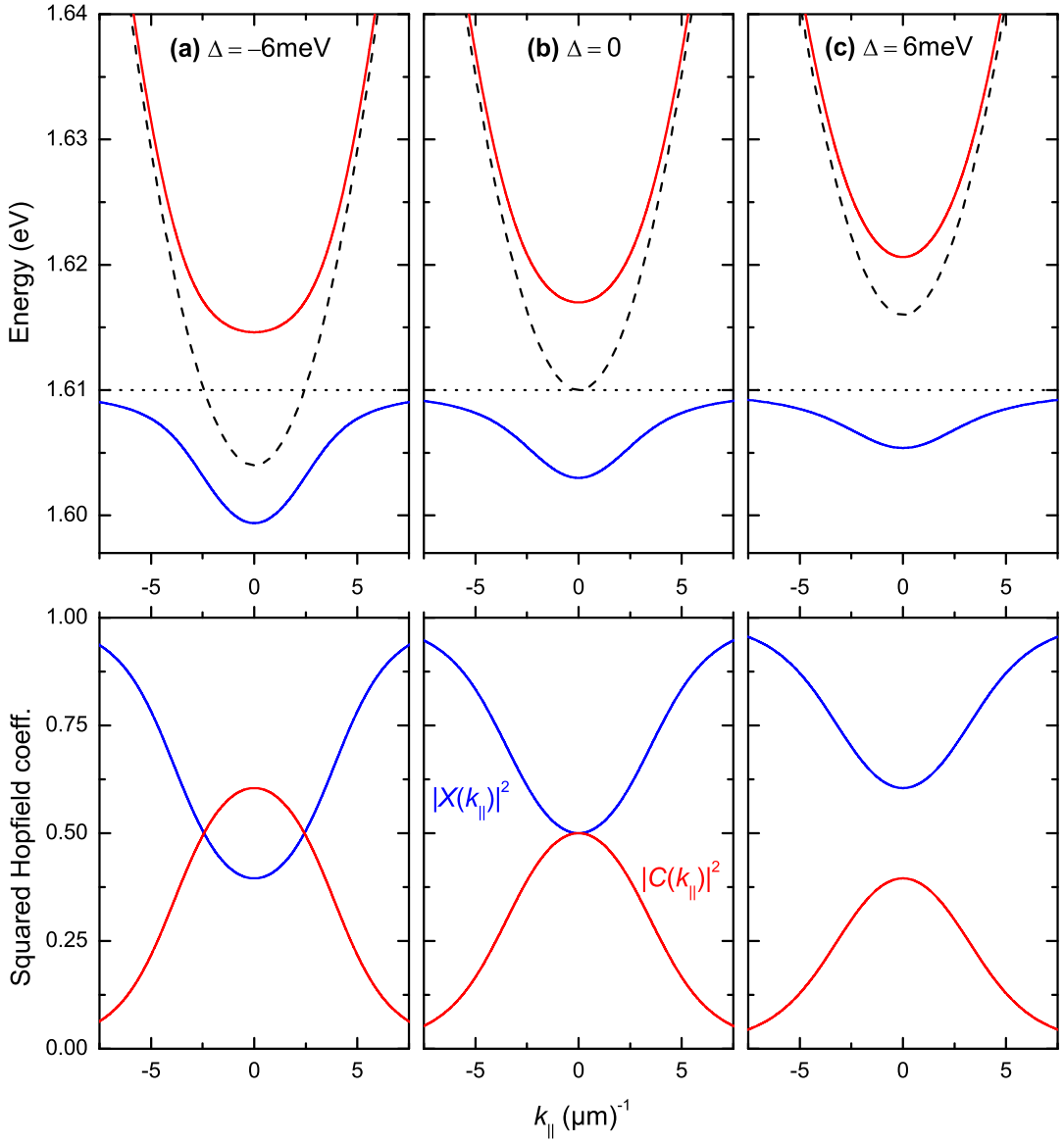

Figure 2-6: *Top row*: Dispersion relations $E(k_{||})$ at different cavity-exciton detunings of (a) $\Delta_0 = -6\,\text{meV}$, (b) $0\,\text{meV}$ and (c) $+6\,\text{meV}$. The dispersion relations of the LP (blue line) and the UP (red line) are obtained using equation (2.29). The exciton energy at $k_{||} = 0$ and the interaction strength are chosen to be $E_\text{X}(k_{||} = 0) = 1.61\,\text{eV}$ and $2\hbar g = 14\,\text{meV}$, respectively. These parameters correspond approximately to those of the sample examined in chapter 5. The bare cavity photon dispersion is based on equation (2.19), while the bare exciton dispersion (dotted line) is assumed to be essentially flat in the $k_{||}$-range shown. *Bottom row*: Corresponding amplitude-squared Hopfield coefficients at the same cavity-exciton detunings as in the upper row, calculated by means of equations (2.31a) and (2.31b).

While quantum-well excitons can have lifetimes of $\tau_{\mathrm{X},0} \sim 1\,\mathrm{ns}$, the cavity-photon lifetime is rarely higher than a few picoseconds. The lifetime of the polaritons is thus limited by the cavity-photon lifetime, which is proportional to the cavity Q-factor.

When the eigenstates of a combined system of a microcavity and a quantum well can be described by the lower and upper polariton branches, the system is denoted to be in the strong coupling (SC) regime.[13] Although it may be suggested by equation (2.29), a quantum-well microcavity is not generally in the strong coupling regime. To outline the circumstances in which such a system is indeed characterised by polaritonic signatures, the finite lifetimes of both the cavity photon and the quantum-well exciton have to be considered. When the leakage of photons out of the cavity and non-radiative exciton recombination processes are governed by the decay rates γ_{C} and γ_{X}, respectively, the polariton dispersions read

$$\begin{aligned} E_{\mathrm{UP,LP}}(k) = \frac{1}{2}\left[E_{\mathrm{X}}(k) + E_{\mathrm{C}}(k) - i\gamma_{\mathrm{X}} - i\gamma_{\mathrm{C}}\right] \\ \pm \frac{1}{2}\sqrt{4\hbar^2\Omega_{\mathrm{R}}^2 - \left[\Delta_k - i(\gamma_{\mathrm{X}} - \gamma_{\mathrm{C}})\right]^2}\,. \end{aligned} \tag{2.36}$$

Here, Ω_{R} describes the so-called Rabi frequency, at which the photon and exciton modes exchange energy. In the specific case of zero cavity-exciton detuning, $\Delta_0 = 0$, this equation can be simplified to

$$E_{\mathrm{UP,LP}}(k) = E_{\mathrm{X}}(k) - i\frac{\gamma_{\mathrm{X}} + \gamma_{\mathrm{C}}}{2} \pm \frac{1}{2}\sqrt{4\hbar^2\Omega_{\mathrm{R}}^2 - (\gamma_{\mathrm{X}} - \gamma_{\mathrm{C}})^2}\,. \tag{2.37}$$

The result of the expressions (2.36) and (2.37) will strongly depend on the sign of the square-root argument. This demonstrates that the physical behaviour of the system is determined by the interrelation of the exciton-photon coupling strength and dissipative terms. Only in the case of $2\hbar\Omega_{\mathrm{R}} > |\gamma_{\mathrm{C}} - \gamma_{\mathrm{X}}|$, the two polariton branches appear and the system is in the SC regime. Experimental investigations on such a quantum-well microcavity with a Rabi splitting of $\hbar\Omega_{\mathrm{R}} \approx 14\,\mathrm{meV}$ are presented in chapter 5.

When the sign below the square root in equation (2.36) is negative, i.e. $2\hbar\Omega_{\mathrm{R}} < |\gamma_{\mathrm{C}} - \gamma_{\mathrm{X}}|$, the last term of the equation becomes purely imaginary. In this case, the bare cavity-photon and exciton dispersion modes are recovered and the system is operating in the weak coupling regime described in subsection 2.3.1.

2.4 Characterisation of Light Fields

The most common properties of light are certainly its intensity, its wavelength or frequency, as well as its polarisation. There are, however, further characteristic pa-

[13] In the scientific community working on quantum-well microcavity systems, the terminology of *strong coupling* is generally accepted. Note, however, that this regime is not identical with strong coupling in terms of quantum optics. In a true quantum-optical strong coupling system, the absorption of a single photon should alter the system. For better differentiation, the appearance of the two polariton branches in quantum-well microcavities is often referred to as non-perturbative normal-mode splitting [Jah96, Khi06].

rameters, which manifest in the coherence properties of light. In this section, the terminology used to describe the coherence properties of the emission from semiconductor light sources is explained.[14]

2.4.1 Optical correlation functions

In classical physics, an ideal electromagnetic wave can be described as a plane wave with frequency ω_0 and complex amplitude $\mathcal{E}(t) = A(t) \cdot \exp[-i\Phi(t)]$. Disregarding the polarisation degree of freedom, the electric field part of an optical wave can be written as:

$$E(t) = \frac{1}{2}\mathcal{E}(t) \cdot \exp(-i\omega_0 t) \; + \; \frac{1}{2}\mathcal{E}^*(t) \cdot \exp(i\omega_0 t) \tag{2.38}$$

$$= \qquad E^+(t) \qquad + \qquad E^-(t) \qquad . \tag{2.39}$$

Such a perfectly monochromatic optical wave does not exist in nature: The natural spectral linewidth of any light source results in an electromagnetic wave with finite extension in time.

The finite spectral linewidth has significant implications for any phase relations of the wave. Consider the state of the wave $E(t)$ at two arbitrary points in time, say t_1 and $t_1 + \tau$. The common way to quantify phase relations between these points is to take the product of both and to average this product over many different times t_1. Thereby, the product is taken as hermitian: $\left\langle E^+(t_1) \cdot E^-(t_1 + \tau) \right\rangle$. If the wave is coherent, the state of the wave at time t_1 defines its state at time $t_1 + \tau$. Consequently, the product should have a specific expectation value. On the other hand, if the wave is not coherent, arbitrary points in time will not be correlated and the average of the product will be zero. For any real light source, it is then interesting to determine the evolution of the product with τ. Furthermore, the above mentioned quantity should be evaluated for any arbitrary point in time t. This is usually done by introducing the first-order correlation function,

$$G^{(1)}(\tau) = \langle \mathcal{E}(t) \cdot \mathcal{E}^*(t + \tau) \rangle \cdot \exp(-i\omega_0 \tau) \; , \tag{2.40}$$

which mainly reduces the problem to the complex amplitude $\mathcal{E}(t)$ of the optical wave. In order to facilitate the comparison of that quantity for different light sources, the first-order correlation function is often written in its normalised form, which reads:

$$g^{(1)}(\tau) = \frac{G^{(1)}(\tau)}{G^{(1)}(0)} = \frac{\langle \mathcal{E}(t) \cdot \mathcal{E}^*(t + \tau) \rangle}{\langle |\mathcal{E}|^2 \rangle} \cdot \exp(-i\omega_0 \tau) \; . \tag{2.41}$$

The first-order correlation function is thus a complex number which satisfies the following properties:

$$g^{(1)}(0) = 1 \; , \tag{2.42a}$$

$$g^{(1)}(\tau) = g^{(1)}(-\tau) \; . \tag{2.42b}$$

[14] An introduction to the theory of quantum-optical correlation functions can be found, e.g., in the textbooks by Loudon [Lou73] and by Mandel and Wolf [Man95].

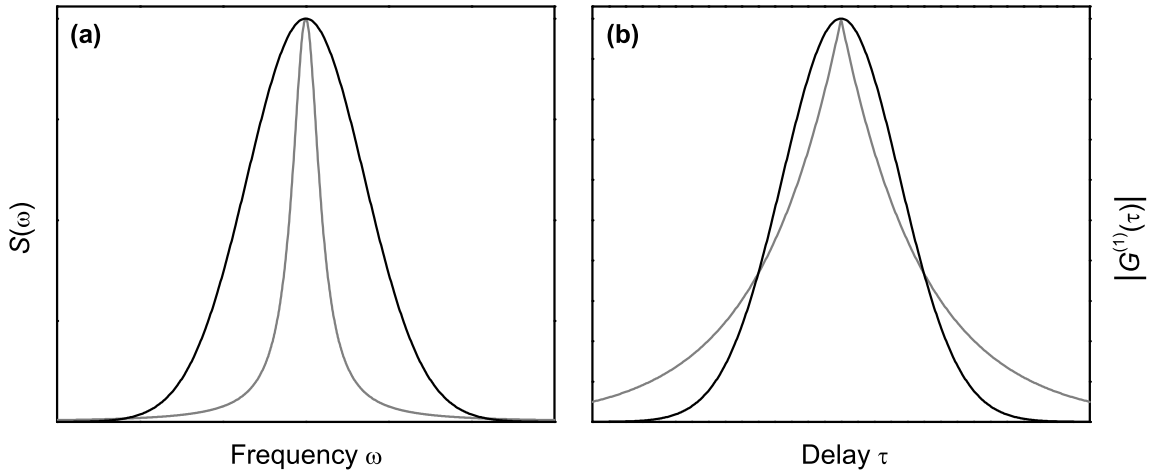

Figure 2-7: Spectral density $S(\omega)$ (a) and corresponding first-order correlation function (b) of different emission lines, illustrating the Wiener-Khinchin theorem [equation (2.44)]. The first-order correlation function of a Gaussian emission spectrum (black line) is again a Gaussian function. A Lorentzian emission line (grey line) results in an exponentially decaying $G^{(1)}(\tau)$.

Moreover, for any real light source, $g^{(1)}(\tau)$ decreases to zero for delay times $\tau \to \infty$. The characteristic time describing the decrease is called the coherence time and can be calculated by

$$\tau_c = \int_{-\infty}^{+\infty} |g^{(1)}(\tau)|^2 \ \mathrm{d}\tau \ . \tag{2.43}$$

Hence, the coherence time specifies the range of delay times τ in which phase relations of the wave are constant in time.

The coherence time of a light wave is also directly connected to the power spectral density $S(\omega)$ of the light source. As stated by the Wiener-Khinchin theorem [Khi34], $G^{(1)}(\tau)$ and $S(\omega)$ are related by

$$G^{(1)}(\tau) = \frac{1}{\sqrt{2\pi}} \int_{-\infty}^{+\infty} \exp(i\omega\tau) \cdot S(\omega) \ \mathrm{d}\omega \ . \tag{2.44}$$

This relation, which is a special case of the Fourier transformation, is illustrated in figure 2-7: If $S(\omega)$ displays a Gaussian shape, the first-order correlation function has a Gaussian shape, too. In the case of a Lorentzian power spectral density, $G^{(1)}(\tau)$ is characterised by an exponential decay.

Hence, first-order correlations can be used to determine the spectral shape of an emission line as well as its coherence time τ_c. However, in order to obtain a full characterisation of the coherence properties of light, it is necessary to consider higher-order correlations as well. Consequently, the introduced correlation function is extended to second-order. Thus, fluctuations in the light intensity instead of the amplitude are considered: The intensity of a photon mode at time t is compared to the intensity at time $t + \tau$. The corresponding correlation function then reads

$$G^{(2)}(\tau) = \langle I(t) \ I(t+\tau) \rangle \ . \tag{2.45}$$

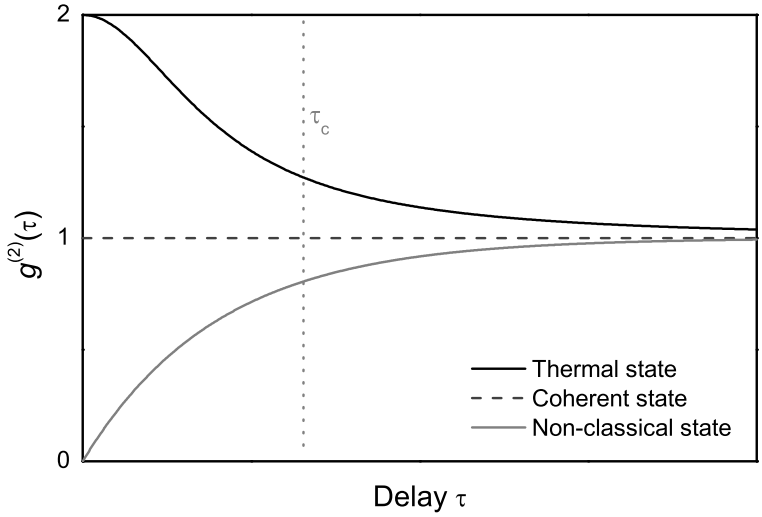

Figure 2-8: Second-order correlation function $g^{(2)}(\tau)$ of different light states. A thermal state (solid black) typically displays photon bunching around zero delay; $g^{(2)}(\tau)$ then decreases towards unity for larger delay times. A coherent state (dashed dark grey) is characterised by $g^{(2)}(\tau) \equiv 1$. Non-classical light (solid grey) exhibits second-order correlation values below unity, i.e. $g^{(2)}(\tau = 0) = 0$ in the case of a single photon source. Note the characteristic differences between the states at zero delay.

Again, in order to provide comparability with other light sources of different absolute intensity, the second-order correlation function is normalised:

$$g^{(2)}(\tau) = \frac{G^{(2)}(\tau)}{\langle I(t)\rangle \langle I(t+\tau)\rangle} = \frac{\langle I(t)\ I(t+\tau)\rangle}{\langle I(t)\rangle \langle I(t+\tau)\rangle} \ . \tag{2.46}$$

Moreover, to take non-classical effects into account, it is necessary to write $g^{(2)}(\tau)$ in terms of the time-dependent bosonic creation and annihilation operators, $\hat{b}^\dagger(t)$ and $\hat{b}(t)$, respectively. Following the theory developed by Glauber [Gla63], the normalised second-order correlation function is then given by

$$g^{(2)}(\tau) = \frac{\left\langle \hat{b}^\dagger(t)\ \hat{b}^\dagger(t+\tau)\ \hat{b}(t)\ \hat{b}(t+\tau)\right\rangle}{\left\langle \hat{b}^\dagger(t)\ \hat{b}(t)\right\rangle \left\langle \hat{b}^\dagger(t+\tau)\ \hat{b}(t+\tau)\right\rangle} \ . \tag{2.47}$$

Here, the normal ordering of the operators is explicitly needed, as otherwise the change of the state of the optical field due to the measurement of one photon would not be accounted for. Equation (2.47) thus describes the conditional probability to detect a second photon at a delay τ after the detection of the first photon at time t, divided by the probability of photon detections at the same times t and $t+\tau$ in the case of photons emitted statistically independent of each other.

Example $g^{(2)}(\tau)$ curves for three different kinds of light states are shown in figure 2-8. For very large delay times, $\tau \to \infty$, second-order correlations have generally a value of $g^{(2)}(\tau \to \infty) = 1$. This is due to the fact that photon emission events with large delay are essentially uncorrelated, independent of the actual light state. At zero

delay, however, these three basic kinds of light states can clearly be distinguished. The differences lie in the probability of the simultaneous detection of two photons being increased, unchanged or decreased, as compared to the case of $g^{(2)}(\tau \to \infty)$. Using the photon number operator of the mode of interest, $\hat{n} = \hat{b}^\dagger \hat{b}$, the value of the second-order correlation function in the case of equal arrival time of two photons ($\tau = 0$) is calculated as follows:

$$g^{(2)}(0) = \frac{\langle \hat{n}(t) \cdot [\hat{n}(t) - 1] \rangle}{\langle \hat{n}(t) \rangle^2} \tag{2.48}$$

$$= 1 + \frac{\left\langle [\Delta \hat{n}(t)]^2 \right\rangle - \langle \hat{n}(t) \rangle}{\langle \hat{n}(t) \rangle^2}$$

$$= 1 - \frac{1}{\langle \hat{n}(t) \rangle} + \frac{\left\langle [\Delta \hat{n}(t)]^2 \right\rangle}{\langle \hat{n}(t) \rangle^2} \ . \tag{2.49}$$

This last expression is composed of three characteristic terms. The first term is constant and thus independent of the light state. The second term, which has a negative sign, accounts for the change of the light state caused by the detection of the first photon at time t. It is inversely proportional to the number of photons in the mode of interest: the larger the number of photons, the smaller the effect of this term. Finally, the third term is related to the photon-number variance $\langle [\Delta \hat{n}(t)]^2 \rangle$ and accounts for the intrinsic noise of the photon-emission processes, which is characteristic of the light state under investigation.

Equation (2.47) reflects the correlations between two photons emitted at times t and $t+\tau$. In general, correlations can be calculated up to arbitrary order. If the order is chosen to be m, the corresponding correlation function describes the probability of m-photon detections. Generally, the correlation function of mth-order is defined as

$$g^{(m)}(t_1, t_2, \cdots, t_m) = \frac{\langle : \prod_{i=1}^{m} \hat{n}(t_i) : \rangle}{\langle \prod_{i=1}^{m} \hat{n}(t_i) \rangle} \ , \tag{2.50}$$

where the colons assure normal ordering of the underlying creation and annihilation operators. The times $t_1, t_2, \cdots, t_m$ denote the detection times of the first, second, $\cdots$, and mth photon, respectively. From a practical point of view, however, the investigation of light states is often restricted to correlations up to second or third order.

2.4.2 Commonly encountered light states

The three different light states shown in figure 2-8, namely thermal, coherent and non-classical light states, display characteristic features in their photon statistics, i.e. the photon-number distribution. These differences in the photon statistics are directly reflected in different values of the equal-time correlation functions of second and higher order. The characteristics of these most commonly encountered states of light are presented in this section.

Non-classical states

Non-classical light states cannot be described by classical electromagnetism. Probably the most prominent non-classical light states are the so-called Fock states, which are eigenstates of the photon-number operator $\hat{n}$. The photon-number distribution of an m-photon Fock state is defined as

$$P_{\text{Fock}}(n) \equiv \begin{cases} 1 & \text{if } n = m \ , \\ 0 & \text{if } n \neq m \ . \end{cases} \tag{2.51}$$

This distribution is obviously of sub-Poissonian character, which especially manifests in a vanishing variance: $\langle (\Delta n_{\text{Fock}})^2 \rangle = 0$. As this state is defined by the number of photons in the light mode of interest, the probability of observing more than one photon at a time is highly dependent on n, too. The equal-time correlations of second order, as defined by equation (2.49), are then given by:

$$g^{(2)}_{\text{Fock}}(0) \equiv 1 - \frac{1}{\langle n \rangle} \ . \tag{2.52}$$

In the case of a Fock state with $n = 1$, as shown by the solid grey line in figure 2-8, $g^{(2)}(0)$ thus vanishes. This effect is commonly used to characterise single-photon sources.

In principle, any light state which exhibits $g^{(2)}(0) < 1$ is a non-classical state, as a quantum-mechanical treatment is necessary to describe it.

Coherent states

The light field irradiated by an ideal single-mode laser is described by a Poissonian photon-number distribution, as the individual photon-emission processes are uncorrelated. With $\langle n \rangle$ denoting the mean photon number per time unit, the probability of n photons actually being in the light mode of interest can be calculated by

$$P_{\text{coh}}(n) = \frac{\langle n \rangle^n}{n!} \exp\left(-\langle n \rangle\right) \ . \tag{2.53}$$

Here, the most probable photon number coincides with the mean photon number. Furthermore, the variance of this Poissonian distribution is given by $\langle (\Delta n_{\text{coh}})^2 \rangle = \langle n \rangle$. Following the relation given by equation (2.49), this results in equal-time correlations of second-order of exactly

$$g^{(2)}_{\text{coh}}(0) \equiv 1 \ . \tag{2.54}$$

Moreover, as shown by the dashed grey line in figure 2-8, $g^{(2)}(\tau)$ is equal to unity independent of the delay τ. This means that an ideal laser is indeed characterised by uncorrelated photon-emission events. Accordingly, the enumerator and the denominator in equation (2.47) are identical in this case.

In general, equation (2.54) represents a state that is coherent in second-order. A perfectly coherent state, however, is described to be coherent up to arbitrary order.

Consequently, a perfectly coherent state is characterised by

$$g_{\mathrm{coh}}^{(m)}(0) \equiv 1 \tag{2.55}$$

for all m.

Thermal states

The textbook example of a thermal emitter is the black body. A radiation field in a thermal state can thus be described to be in thermal equilibrium with a black body which acts as an emitter: Emission and absorption processes are in thermal equilibrium, i.e. they cancel each other out. Furthermore, the only parameter needed to specify the quantised radiation field is its temperature T. It can be shown that the photon-number distribution of a single thermal mode of such a radiation field is given by

$$P_{\mathrm{the}}(n) = \frac{\langle n \rangle^n}{(\langle n \rangle + 1)^{n+1}} \ , \tag{2.56}$$

where the effective temperature of the system defines the mean photon number $\langle n \rangle = [\exp(\hbar\omega / k_{\mathrm{B}} T) - 1]^{-1}$. Equation (2.56) thus follows a Bose-Einstein distribution with a variance of $\langle (\Delta n_{\mathrm{the}})^2 \rangle = \langle n \rangle + \langle n \rangle^2$. Here, the first term is identical to the Poissonian noise of a coherent state, while the second term reflects intensity fluctuations in the mode of interest.

The increase in photon-number fluctuations results in the characteristic bunching peak observed in second-order correlations, namely in

$$g_{\mathrm{the}}^{(2)}(0) \equiv 2 \ . \tag{2.57}$$

This can be understood as follows: The detection of a photon indicates the high probability that the intensity at the moment of detection is much higher than the mean intensity. It is thus very likely that a second photon is detected simultaneously with the first one. This photon bunching peak has a characteristic width around $\tau = 0$, as described by the Siegert relation:

$$g^{(2)}(\tau) = 1 + \left| g^{(1)}(\tau) \right|^2 \ . \tag{2.58}$$

Apparently, any bunching effect disappears for delays τ larger than the coherence time τ_c of the light state, as shown by the solid black line in figure 2-8.

Finally, it can be demonstrated that a thermal state is also described by characteristic values of higher-order correlations. In mth order, the equal-time correlations are defined as:

$$g_{\mathrm{the}}^{(m)}(0) \equiv m! \ . \tag{2.59}$$

Chapter 3

Experimental Methods

Correlation techniques have been widely used in different fields of science working with optical spectroscopy methods. Field autocorrelation techniques are utilised in various disciplines, ranging from fundamental sciences, e.g. Fourier transform infrared spectroscopy [Smi09], to medical applications such as optical coherence tomography [Hua91]. Interferometric autocorrelators are applied to measure the temporal duration of short laser pulses [Dem03]. Photon correlation techniques using Hanbury Brown-Twiss (HBT) setups are employed [HB56], e.g., to characterise single-photon sources [Lou05]. All these examples illustrate the benefit of optical correlation techniques for the characterisation of different light-emitting model systems.

In this thesis, two different optical correlation quantities of light are investigated. From the emission of QD micropillar lasers, both the first-order and the second-order correlation function are determined. The emission of a planar microcavity polariton laser is analysed in a regime of strong non-equilibrium using non-resonant ultra-short picosecond-pulsed excitation. Here, the focus lies on second-order correlation spectroscopy combined with time-resolved photoluminescence as well as angle-resolved spectroscopy. In this chapter, the utilised experimental techniques are presented.

In section 3.1, the optical setup and the different components used to conduct Michelson interferometry and micro-photoluminescence (micro-PL) measurements on QD micropillars are described. In the subsequent sections, the experimental methods used to investigate the planar microcavity sample are introduced. First, the experimental method used to perform angle-resolved spectroscopy is described in section 3.2. Finally, the technique applied to measure time-resolved PL as well as second-order correlations is discussed in section 3.3.

3.1 Michelson Interferometry

A sketch of the optical setup used for the investigations of the QD pillar microcavities is shown in figure 3-1. A continuous wave (cw) diode laser, that operates at an emission wavelength of 785 nm, is used to excite the samples. Two neutral density

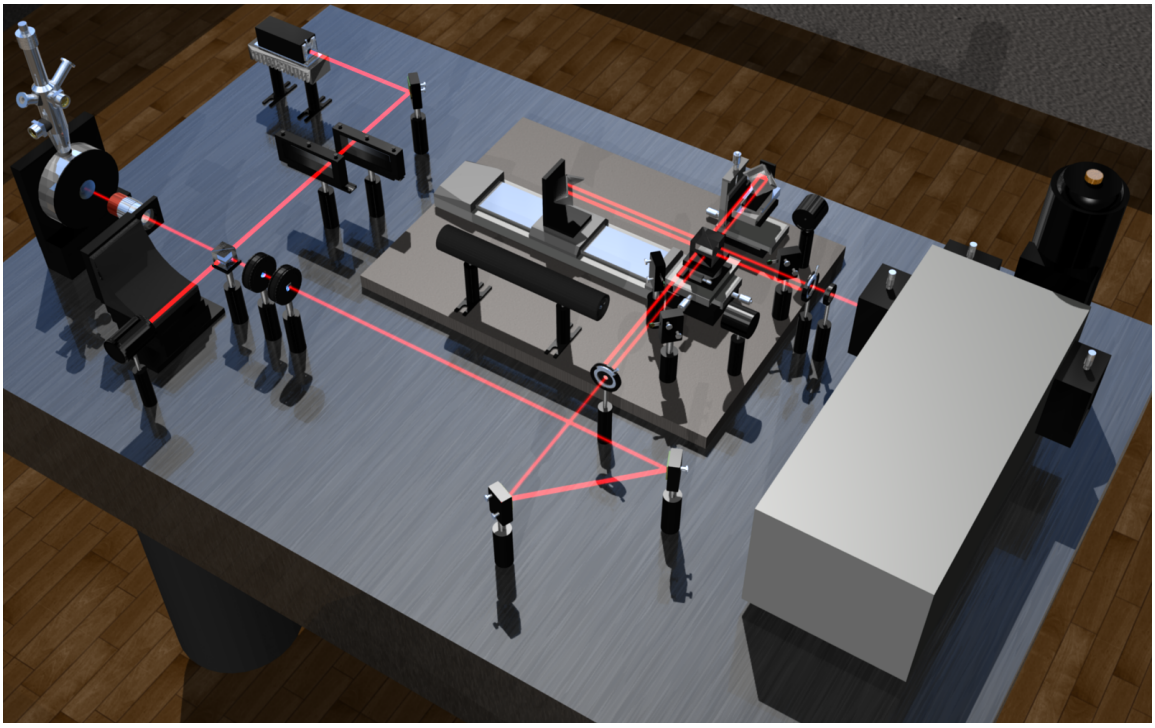

Figure 3-1: Sketch of the optical setup utilised for the investigation of QD micropillars; see chapter 4. The sample is excited using a cw diode laser operating at a wavelength of 785 nm. Via a beam splitter and a microscope objective, the excitation laser is focused onto the sample which is held at low temperatures in a He-flow cryostat. Photoluminescence is collected using the same MO. A specific polarisation component of the emission can be selected using a half-wave plate and a Glan-Taylor prism. The emission light beam is then transferred to the Michelson interferometer. At the output of the MI, the signal is recorded by a CCD camera connected to an optical monochromator. In this illustration, the reference laser of the interferometer is switched off for clarity; a closeup of the interferometer is shown in figure 3-2. A detailed description of the individual components is given in the main text.

attenuators are used to control the excitation intensity. The excitation laser beam is directed via a beam splitter onto an axis perpendicular to the sample surface and focused onto the sample using a microscope objective (MO). Depending on the lateral size of the micropillar, different objectives with adequate numerical apertures (NAs) and magnification are used.[1] The use of MOs allows for small spot diameters in the range of 1–10 µm. Furthermore, in order to be able to selectively investigate individual micropillars, the objective is mounted on piezo-driven actuators thereby allowing for positioning with sub-micron resolution.

The micropillar sample is fixed in the liquid-helium flow cryostat shown in figure 3-1 at the left hand end of the optical table. The temperature at the position of

[1] Different microscope objectives are utilised, depending on the experimental requirements. The available MOs (Mitutoyo "M Plan APO") are optimised for the near-infrared spectral region and have the following specifications:
MO1: 10x magnification, NA = 0.26, working distance 30.5 mm.
MO2: 50x magnification, NA = 0.42, working distance 17.0 mm.
MO3: 100x magnification, NA = 0.5, working distance 12.0 mm.

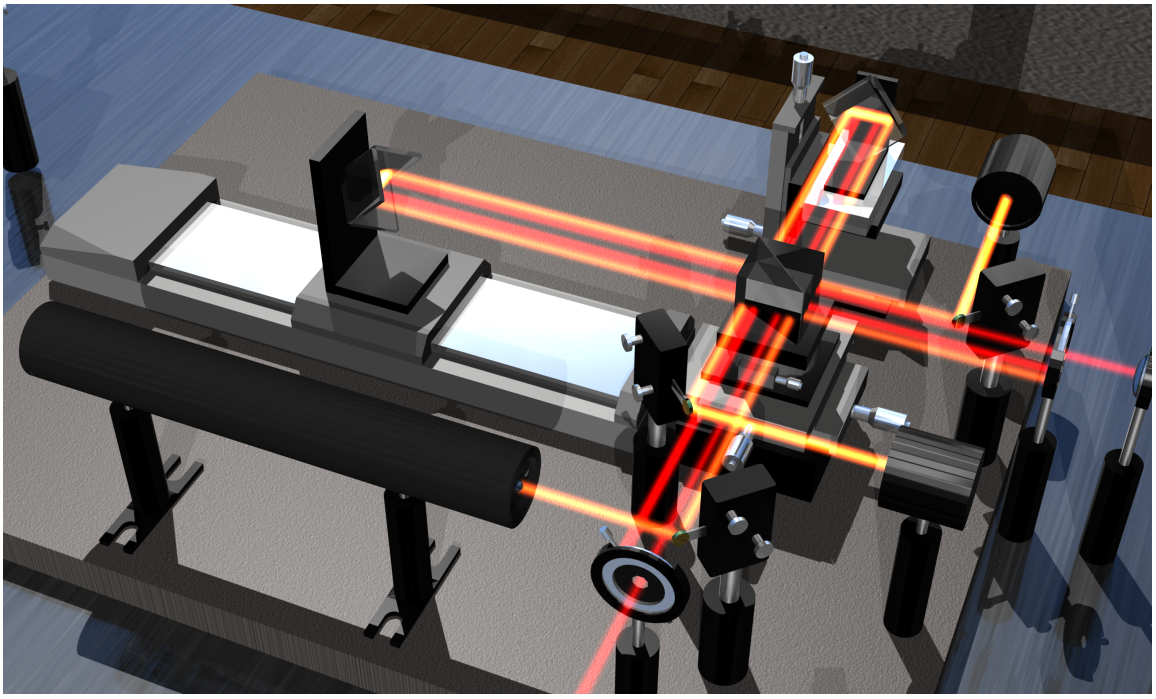

Figure 3-2: Closeup view of the Michelson interferometer, which consists of a non-polarising 50/50 beam splitter cube and two retroreflector mirrors each mounted on specific translation units. The interference pattern of the HeNe-laser (orange colour) is recorded by two standard silicon photodiodes and used as a reference for the computer-controlled stabilisation algorithm. The emission from the sample under investigation (red colour) is directed parallel to the beam of the reference laser.

the sample can be varied in the range of 10 –325 K. The cryostat is mounted on a set of three translation stages, each equipped with a differential micrometer screw. This configuration allows for a coarse positioning of the cryostat and the sample with respect to the MO and to the optical excitation and detection axis. The photoluminescence of the sample is collected using the MO described before and passes through the beam splitter. A specific polarisation component is selected using a set of polarisation optics, namely a half-wave plate and a Glan-Taylor prism. Here, the prism is kept fixed during all experiments, while the wave plate is adjusted in order to select a certain polarisation direction from the emission of the samples. The PL is then directed towards the Michelson interferometer (MI), which is shown in figure 3-2.

The Michelson interferometer consists mainly of a 50/50 beam splitter cube and two retroreflector mirrors each attached to a delay unit. The beam splitter is non-polarising and features a high-degree anti-reflection coating to minimise secondary reflections in the interference signal. The light beam under investigation is directed to the beam splitter cube and split into two parts of equal intensity. Each part is sent towards a retroreflector mirror which guides the light beam back towards the beam splitter. Both retroreflector mirrors are aligned such that the different parts of the beam are fully overlapping when they finally join again at the beam splitter and exit the interferometer. Here, the interference of the two beams can be measured with an

appropriate detector, as will be further described below.

In order to investigate the dependence of interference effects on the optical path difference, each retroreflector mirror is attached to a translation stage.[2] The first mirror is mounted on a mechanical stage controlled by a rotary pulse encoder. It can be moved by 306 mm at most with a step resolution of less than 0.5 µm. The second mirror is mounted on a piezo-driven actuator which can be moved over a maximal distance of 15 µm. The actuator is regulated by a closed-loop control system based on an electronic proportional-integral element. Thereby, typical deficiencies of piezo-elements like thermal drifts, hysteresis, and creeping can be almost fully avoided. This enables a stable displacement of the mirror with an accuracy of less than a nanometre. In the configuration applied here, these two translation stages allow for changes of the optical path difference in the range of $\Delta l_{\mathrm{min}} = -530\,\mathrm{mm}$ to $\Delta l_{\mathrm{max}} = 82\,\mathrm{mm}$.

The Michelson interferometer is further equipped with a standard cw helium-neon laser, as shown in the bottom left part of figure 3-2. The use of this auxiliary laser, emitting at a wavelength of about 632.8 nm, has two purposes. First, primary alignment of the interferometer is easily achieved using the visible light from the HeNe-laser. By positioning scriber templates at distances much larger than the maximal movement range of the translation stages, it is assured that the recombined beams at the output port of the MI are both highly parallel and overlapping, independent from the actual position of the translation stages. Second, using two standard Si photodiodes as shown in figure 3-2, the interference pattern of the HeNe-laser emission can be monitored simultaneously with the actual interference measurement of the cavity emission. Thereby, any mechanical disturbances in the interferometric setup can directly be detected and accounted for during the data analysis. Alternatively, the piezo-driven actuator in the interferometer can be used to compensate for any perturbation in real time allowing stable measurements on longer time scales. The stabilisation can be switched on or off depending on the current experimental conditions. In the experiments described in this thesis, stabilisation is used whenever the acquisition of single intensity data points lasted longer than 100 ms.

Changing the optical path length of one or both of the beams enables the measurement of interference fringes. To measure the interference pattern of the different emission modes of QD micropillar lasers, a spectrometer is attached to the output port of the interferometer.[3] Via a 100 mm lens, the interference signal is focused onto the entrance slit of a monochromator with a focal length of 500 mm. The monochromator is equipped with a motorised turret carrying three optical diffraction gratings with different groove densities. The spectrally resolved light cone is then

[2] The interferometer is equipped with a M-531 linear positioning stage and a P-752 high precision nanopositioning stage, both manufactured by Physik Instrumente (PI) GmbH & Co. KG.

[3] The spectrometer consists of a SpectraPro 2500i monochromator by Acton Research Corporation and a Spec-10:400/UV/LN Si CCD camera by Roper Scientific. The monochromator features a motorised turret carrying three gratings with different groove densities. The available gratings feature groove densities of 300, 600 and 1200 grooves/mm. The gratings with 300 and 1200 grooves/mm are blazed at a wavelength of 1 µm. The grating with 600 grooves/mm is blazed at 500 nm. The CCD camera has a resolution of 1340 by 400 pixels, where each pixel has an edge length of 20 µm.

recorded by a liquid-nitrogen cooled charge-coupled device (CCD) camera.[4] Under perfect alignment conditions, the overall spectral resolution of the spectrometer is roughly 100 μeV. By using the spectrometer instead of a simple photodiode, it is possible to simultaneously record first-order correlations of the different spectral components of the sample under investigation.

For the present work, the aim of Michelson interferometry is to measure the first-order correlation function $g^{(1)}(\tau)$ and to determine the coherence time of the QD micropillar cavity emission. Accordingly, the typical measurement procedure is as follows. While the position of the mechanical translation stage is kept fixed, the piezo-driven actuator is moved step-by-step and the intensity of the interference signal is measured simultaneously. Thereby, the actuator is moved over a total distance that equals approximately the wavelength of the signal under investigation. This results in typical interference fringes which directly reflect the evolution of $g^{(1)}(\tau)$. While the oscillation period of the first-order correlation function is thus known, the quantity of interest is the so-called visibility V of the fringes which is defined as

$$V = \frac{I_{\max} - I_{\min}}{I_{\max} + I_{\min}} \, . \tag{3.1}$$

Here, $I_{\max}$ and $I_{\min}$ are the maximal and minimal intensity of the measured interference signal, respectively. Both values are obtained by fitting a cosine function to the data. By repeating this sequence for different positions of the mechanical translation stage, the dependence of the visibility on the delay time τ between both beams can be measured. The resulting quantity $V(\tau)$ is directly related to $g^{(1)}(\tau)$, as can be derived from equation (2.41):

$$V(\tau) = \frac{I_{\max}(\tau) - I_{\min}(\tau)}{I_{\max}(\tau) + I_{\min}(\tau)} = \left| g^{(1)}(\tau) \right| \, . \tag{3.2}$$

Accordingly, the measurement of $V(\tau)$ corresponds to a direct measure of the envelope function of the first-order correlation function $g^{(1)}(\tau)$. This gives direct access to the coherence time, as will be shown in chapter 4.3.

The Michelson interferometer is fully computer-controlled. A software application was written in Labview which features a graphical user interface. This application controls the positioning of the two delay units, initialises measurements by the spectrometer, enables data acquisition, and actively stabilises the interferometer using the interference signal from the HeNe-laser, as described above.

The experimental setup presented in figure 3-1 can further be used to perform standard micro-PL spectroscopy measurements by blocking one of the interferometer arms, thereby avoiding interference effects.

[4] The CCD camera was typically operated at a temperature of −100°C.

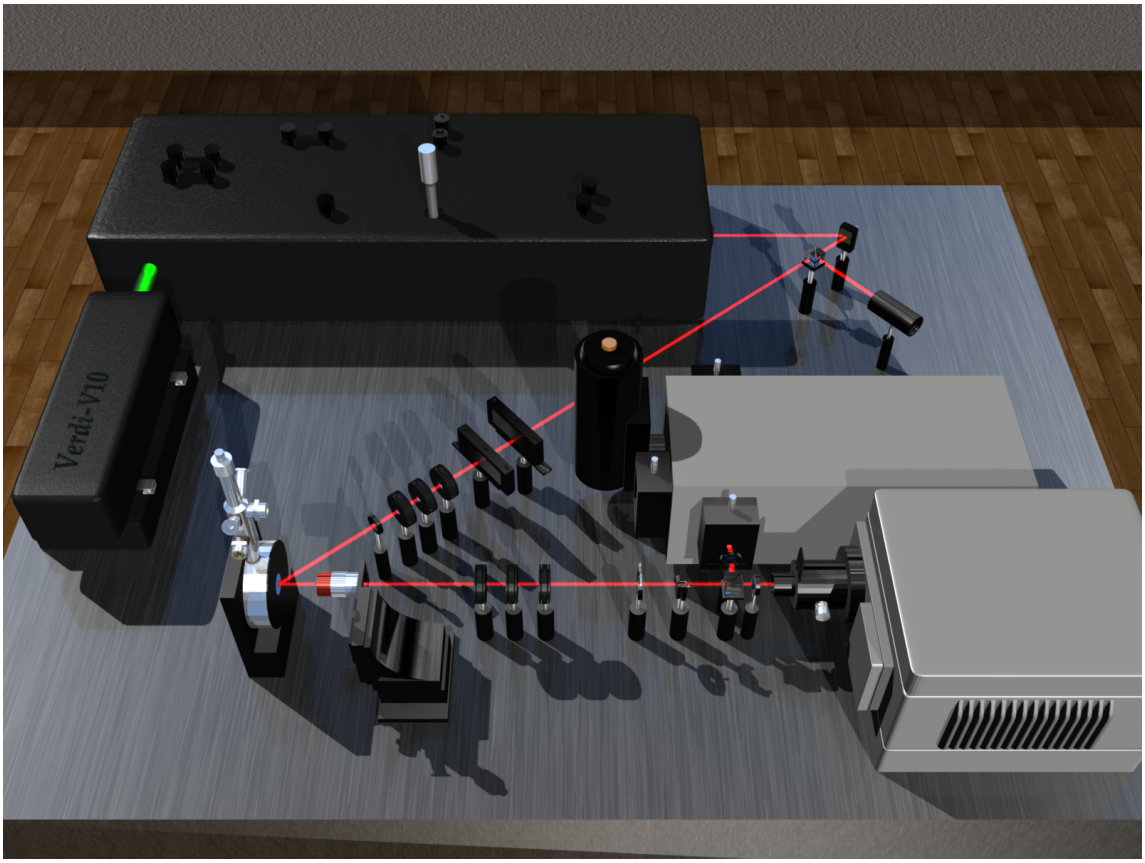

Figure 3-3: Sketch of the experimental setup utilised to perform Fourier-plane imaging as well as streak camera measurements. It consists of an excitation laser system, various optical elements to bring the excitation laser to the sample, a liquid-helium flow cryostat, optical elements to collect light emission from the sample, and two different optical detectors. The first detector is an optical spectrometer (mid right), as presented in the previous section. Here, it is used for Fourier-plane imaging and PL spectroscopy. The second detector is the streak camera (bottom right), whose functionality is covered in section 3.3. Detailed information about each part of the setup is given in the main text and in the caption of figure 3-5.

3.2 Fourier-Plane Imaging

To investigate the strongly-coupled planar microcavity sample, mainly two different techniques are applied. First, Fourier-plane imaging is performed to measure the in-plane dispersion of the cavity emission. From this data, different excitation-power dependent quantities can be derived, namely the actual shape of the dispersion, the energy, the intensity, as well as the linewidth of the emission. Second, photon-correlation spectroscopy and time-resolved PL is employed. All measurements are realised using the optical setup shown in figure 3-3. In this section, the different opto-mechanical components of the setup as well as the working principle of Fourier-plane imaging are described. The technique used for photon correlation spectroscopy and time-resolved PL will be covered in section 3.3.

In order to optically excite the samples, a picosecond-pulsed laser system is

utilised. This laser system consists of a Nd:YVO_4-based cw laser emitting at a wavelength of 532 nm, which pumps a mode-locked Ti:sapphire laser oscillator.[5] The emission wavelength of the mode-locked laser can be tuned in the range of 700–1000 nm. Here, the emission wavelength is configured to either correspond to the first reflection minimum of the DBR stopband of the investigated cavity sample ($\lambda \approx 744$ nm) or to be quasi-resonant with the lower polariton branch under the specific angle of incidence. The laser cavity is set to produce optical pulses with pulse durations of 2 ps at a pulse repetition rate of 75.39 MHz.

Using a beam splitter, a minor part of the excitation beam is directed to a fast photodiode in order to synchronise the excitation laser with the streak camera used for photon-correlation spectroscopy, as described in section 3.3. Furthermore, the intensity of the excitation laser can be controlled by two neutral density attenuators. The attenuators are positioned such that their density gradients increase in opposite directions in order to minimise beam displacements to a negligible level. In order to control its polarisation, the excitation laser beam passes through a Glan-Taylor prism, a half wave plate as well as a quarter wave plate. The beam is then directed towards the sample at an angle of incidence of roughly 45° from the sample surface and focused onto the sample by a lens with a focal length of 65 mm. The excitation spot on the sample typically has a diameter of 20–30 µm.

The planar microcavity sample is positioned in the He-flow cryostat in the same way as the micropillar sample. The emission from the cavity is collected using a microscope objective. As MOs with long working distances are used, it is possible to perform both non-resonant and quasi-resonant excitation of the sample under an angle of incidence of roughly 45°, as mentioned above. The numerical aperture of the MO defines hence the range of emission-angles that are collected by the MO and which are thus accessible for Fourier-plane imaging.[6] Here, MOs with numerical apertures of 0.26 and 0.42 are used, corresponding to maximal detection angles of ±15° and ±24.8°, respectively. As described in chapter 2.2.1, the angle θ of the emitted light from a Bragg microcavity directly reflects the in-plane wave vector $k_{||}$ of the cavity photons. When the cavity is in the strong coupling regime, this corresponds exactly to the wave vector of the cavity polaritons. Both quantities are related by

$$k_{||} = k \cdot \sin\theta = \frac{E_{\mathrm{ph}}}{\hbar c} \sin\theta \ . \tag{3.3}$$

Furthermore, all photons emitted under the same angle θ meet in the same point of the Fourier plane of the collecting objective. The intensity and energy distribution of the Fourier plane can then be measured using an appropriate lens system and a suitable optical detector. The basic principle of Fourier-plane imaging is illustrated in figure 3-4. In the setup presented in figure 3-3, two lenses with focal lengths of

[5] The pump laser is a Coherent Verdi-V10 which has a maximum output power of 10 W. It pumps a Coherent Mira Optima 900-D, which contains a Ti:sapphire crystal as active medium. In principle, this dual-version of the Mira can be configured to emit pulses with durations in the picosecond or in the femtosecond range.

[6] An alternative way to measure the angular-resolved photoluminescence from microcavities is to utilise goniometer rails [Den06, Stu11].

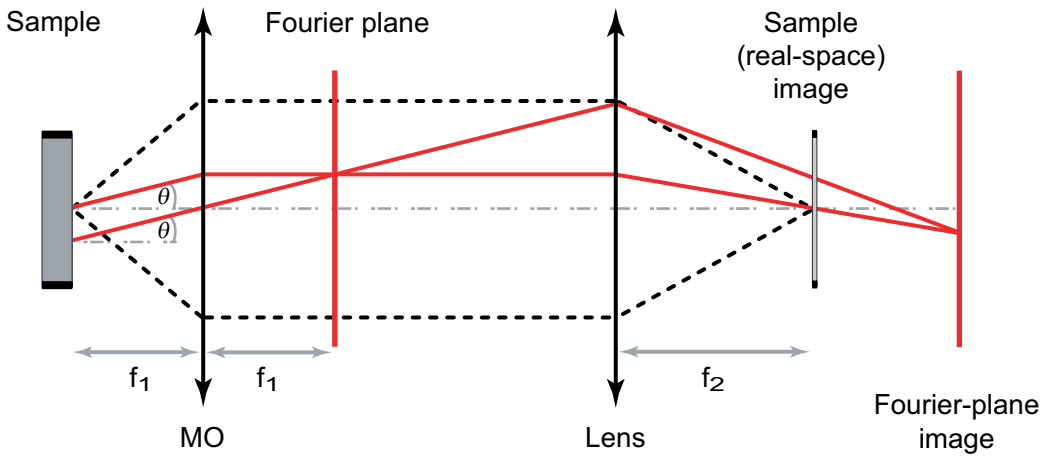

Figure 3-4: Schematic illustration of the Fourier-plane imaging technique. The beam path used for Fourier-plane imaging is indicated by red solid lines: All photons emitted under the same angle meet in the same point in the Fourier plane, which is identical to the back focal plane of the microscope objective (MO). The Fourier plane is subsequently imaged onto a detector, e.g. the entrance slit of a spectrometer. For comparison, the beam path conventionally used for real space imaging of the sample is shown by dashed black lines. Note that, in the actual experiment two lenses are used to image the Fourier plane onto the entrance slit of the monochromator; thereby, the diameter of the beam is adapted to the height of the CCD chip dimensions in order to maximise the angular resolution.

750 mm and 600 mm, respectively, are inserted in the detection beam path to image the Fourier plane onto the entrance slit of the spectrometer.[7] The angular resolution of this method is then given by the chip dimensions and pixel sizes of the CCD camera.[8]

Moreover, a set of polarisation optics positioned in the detection beam path right after the 750 mm lens is used to single out a specific polarisation component of the emission from the microcavity. This set consists of a quarter-wave plate, a half-wave plate and a Glan-Taylor prism.

3.3 Photon Correlation Spectroscopy

When single-photon sources of any kind shall be identified and characterised, the typical procedure is to apply photon correlation spectroscopy techniques [Lou05]. To characterise coherent semiconductor light sources, photon correlation methods have been applied to measure the second-order coherence of their emission: Different types of microcavities have been studied in the regime of weak coupling [Ulr07, Wit11] as

[7] See footnote on page 32 for further information on the spectrometer.

[8] The CCD camera attached to the monochromator has a vertical resolution of 400 pixels. In perfect alignment conditions, this results in minimum bin sizes of $\Delta\theta \approx 0.08^\circ$ per pixel or of $\Delta\theta \approx 0.12^\circ$ per pixel when using the MO with 10x or 50x magnification, respectively.

well as in the regime of strong coupling [Den02, Kas08a, Lov08]. In all these works, second-order correlations were measured using two avalanche photodiodes in HBT configuration. The resulting time resolution of such a HBT setup lies typically above 100 ps.

In order to check, whether the real (i.e. not masked by the finite experimental time resolution) photon correlation function according to equation (2.47) can be measured, the time resolution has to be compared to the coherence time of the light investigated. As described in chapter 2.4, any photon bunching effect occurs only within the coherence time of light. The time resolution of avalanche photodiodes is often sufficient for investigating the light emission by atoms. In semiconductors, spontaneous emission occurs on a sub-nanosecond time scale with coherence times often shorter than the time resolution of a HBT setup. When semiconductor nanostructures are embedded in a microresonator, there may additionally be a strong enhancement of the spontaneous decay rate due to the Purcell effect [Pur46] such that the decay dynamics can no longer be resolved by such a setup due to the short coherence times [Gér98].

In this section an experimental technique is presented that uses a modified streak camera featuring a time resolution of 2 ps and which is thus adequate to characterise the fast emission processes of semiconductor microcavities. This technique has been introduced in references [Wie09] and [Aßm09]. Within the framework of this thesis, this technique was further enhanced to enable faster data acquisition and shorter measurement times. The experimental details are illustrated in subsection 3.3.1, while the procedure of data processing is described in subsection 3.3.2. Finally, typical error sources and corresponding countermeasures are discussed in subsection 3.3.3. This photon correlation spectroscopy technique is applied to investigate a strongly-coupled microcavity-polariton system; the discussion of the results will be presented in chapter 5. A detailed description of this technique has also been published, see item P1 in the publication list (page 123).

3.3.1 Streak camera setup

The optical setup used to perform photon correlation spectroscopy with a streak camera was shown in the previous section in figure 3-3. As mentioned above, a small part of the excitation laser beam is directed onto a fast photodiode. This photodiode generates a trigger signal for the streak camera. Thereby, the streak camera is synchronised with the pulse repetition period of the excitation laser. The emission from the sample, which is collected via a MO, is first directed onto the spectrometer to monitor the spectrum of the cavity emission. Subsequently, a diaphragm is used to exclusively select the emission with zero in-plane wave vector, which corresponds to the emission normal to the sample surface. To further restrict the photon correlation analysis to the emission mode of interest, an interference filter with a narrow bandwidth of approximately 1 nm is utilised.

As in standard streak camera measurements, the signal is then focused onto the entrance slit of the streak device using a lens with a focal length of 50 mm. After pass-

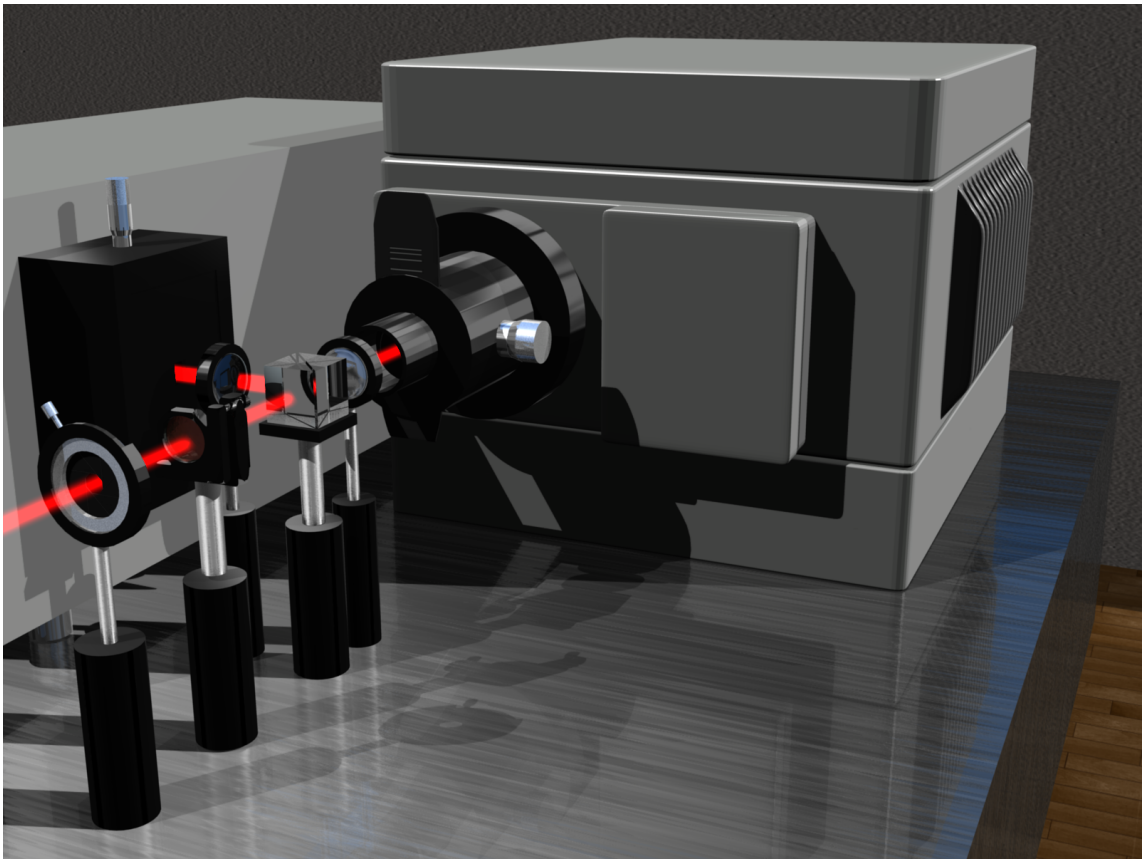

Figure 3-5: Closeup view of the streak camera used for photon-correlation spectroscopy and time-resolved measurements. The streak camera is synchronised with the picosecond-pulsed laser via the fast trigger photodiode shown in figure 3-3. The sample emission, which is preselected in $k_{||}$-space using a diaphragm and in energy using an interference filter, is focused onto the entrance slit of the camera by a 50 mm lens. The functionality of the streak camera is described in detail in the main text.

ing through the entrance slit the light pulse hits onto a photocathode, thereby generating photoelectrons. These electrons, whose number is proportional to the light-pulse intensity, are electrically accelerated towards a micro-channel plate (MCP). On this way, the electrons are also deflected perpendicular to their direction of flight using a pair of sweep electrodes. This vertical sweep unit is synchronised with the excitation laser via the fast photodiode (compare figure 3-3) and provides the time resolution, as photoelectrons traversing the unit at different times are deflected under different angles. When the electrons pass through the MCP stage,[9] they are multiplied and finally hit a phosphor screen. While the vertical position on the screen is then proportional to the arrival time of the individual photons, the horizontal position corresponds to the position of the photon inside the light cone. Furthermore, the intensity of the screen phosphorescence is proportional to the intensity of the incident light. Finally, an image of the phosphor screen is captured by a CCD camera with a resolution of 640 by 480 pixels.

[9] In subsection 3.3.3, the importance of the settings of the MCP gain voltage will be discussed.

In order to perform photon-correlation measurements, single-shot pictures have to be recorded. Unfortunately, acquiring only one single pulse streak per image would result in unreasonably long data acquisition times. For this reason, the streak camera is equipped with a second pair of sweep electrodes, which deflects the accelerated photoelectrons in horizontal direction. Due to this additional deflection of the electrons a set of several dozen consecutive streaks, positioned next to each other in horizontal direction, can be imaged simultaneously. The minimal horizontal deflection speed is determined by the minimal distance required to distinguish individual vertical streaks on the screen. The speed can be set to 300, 600, or 1200 ns per full horizontal screen width (640 pixels). When using the deflection time of 600 ns, 45 consecutive pulses can be recorded per single picture. Example single and integrated images are shown in figure 3-6.

A further customisation of the streak device lies in the choice of the phosphor screen, which is made of P-46 phosphor ($Y_3Al_5O_{12}$:Ce) in the present camera setup. P-46 phosphor features a fast bi-exponential afterglow decay with the slower timescale being in the range of few tens of microseconds. The afterglow decay rates are thus fast enough to allow for high CCD camera frame rates. The drawback of this phosphor is a reduced number of emitted photons per incident electron. This is compensated for by adding a second micro-channel plate to the streak camera. The upper boundary for the overall operation speed of the streak camera is then given by the effective frame rate of the CCD imaging the phosphor screen.

Within the framework of this thesis, the overall operation speed of the correlation spectroscopy technique described above was further improved. In a previous configuration, the frame rate of the CCD camera attached to the streak device was typically set to roughly 70 Hz. The CCD camera was then triggered by the dual-time blanking unit of the streak camera. The feedback signal resetting the blanking unit came from a hardware dongle attached to the computer running the streak-camera control software.[10] In the present settings, the primary trigger signal still stems from the blanking unit. The hardware dongle, however, could be omitted: The CCD camera is configured to provide itself the reset signal to the blanking unit, thereby maximising the operation speed. In this configuration, the maximal frame rate is increased to roughly 140 Hz. To enable this high frame rate the CCD camera has to be run in 2-tap mode, which allows for independent readout of the two half-screens of the CCD chip. Correspondingly, the data acquisition time needed to record a typical set of 100,000 single-shot pictures is reduced from 20–25 minutes to roughly 12 minutes.[11]

[10] Hamamatsu Trigger/Status Adapter C.

[11] CCD cameras with higher frame rates than the one used in the present work are indeed available. Unfortunately, their high speed comes at the cost of significantly reduced quantum efficiency. Therefore, they are not suitable for photon correlation spectroscopy using the streak camera.

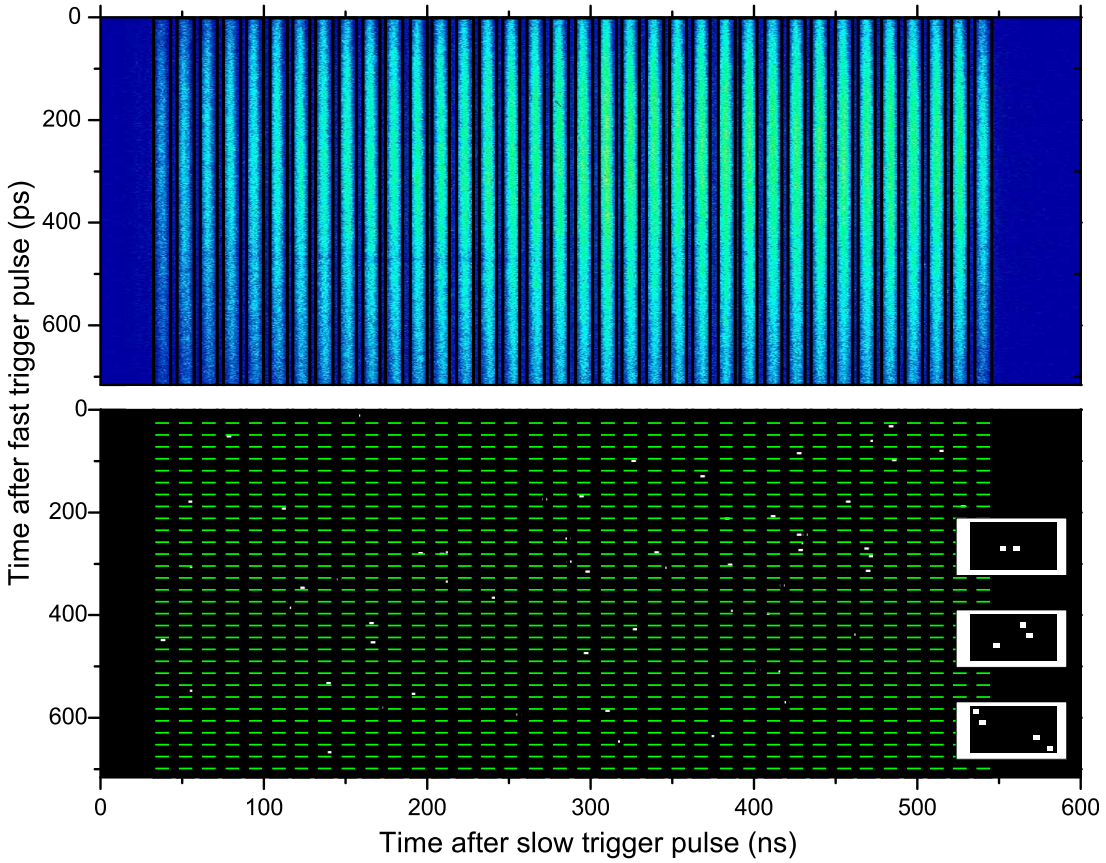

Figure 3-6: Examples of raw integrated (upper panel) and single-shot (lower panel) data acquired in photon-correlation measurements using the streak camera. The upper panel image was obtained after integration over 60,000 single pictures. The vertical black lines in the upper panel denote the borders of the individual streak bins. Photons arriving outside of these borders are not considered for data analysis. The vertical distance between two green lines in the lower panel illustrates the pixel binning within individual streak bins. In this example, the 700 ps of the vertical time axis are divided into 30 time bins. The insets show magnified time bins exemplifying two-, three, and four-photon coincidences.

3.3.2 Photon statistics data processing

Typical examples of integrated and single pictures acquired with the technique described above are shown in the upper and lower panel of figure 3-6, respectively. In the following, a detailed discussion on how to extract the second-order correlation function from the raw data is presented.

To calculate the intensity correlation function, the number of photon pairs detected at times t and $t + \tau$, respectively, has to be determined. This information can be extracted from each single picture as follows. At first all photons in all pictures are sorted to vertical streak bins with a width of one streak. Streak bins are illustrated in the upper panel of figure 3-6 by vertical black lines. Photons that are detected between two streak bins have to be disregarded. Subsequently, the temporal resolution $\Delta\tau$ can be set by pixel binning within each single streak bin. Thus, the streak bins are divided into time bins of a length corresponding to $\Delta\tau$. In the lower

panel of figure 3-6, this time binning is represented by the horizontal green lines.

The binned data set is then analysed with an algorithm that counts all photon pairs inside each single streak of each single picture and sorts them according to the time of detection of the first photon and the time delay τ between the two photons. In the case of equal arrival time, thus $\tau = 0$, this count is multiplied by two. Thereby, it is accounted for the fact that the number of photon pairs counted in a bin containing n photons will be $n(n-1)/2$. As the definition of $g^{(2)}(\tau)$ makes use of the photon number of the mode of interest before and after the detection of a first photon, the number of photon pairs should be $n(n-1)$. Dividing the number of pairs by the number of recorded single pictures already gives the photon pair counting rate for a certain combination of arrival time t and delay τ. Accordingly, the simultaneous detection of four photons, as depicted in the lowest inset of figure 3-6, corresponds to twelve two-photon pairs. The determination of the photon pair number corresponds to calculating the enumerator of equation (2.47),

$$G^{(2)}(t,\tau) = \left\langle \hat{b}^\dagger(t)\ \hat{b}^\dagger(t+\tau)\ \hat{b}(t)\ \hat{b}(t+\tau) \right\rangle \ , \tag{3.4}$$

which represents the second-order correlation function without normalisation. Note that, in equation (3.4), $\langle\cdot\rangle$ denotes the ensemble average, not the average over different times t.

In order to obtain the second-order correlation function in its normalised form, it is required to determine the expectation value of the number of photon pairs detected at the same times t and $t+\tau$ emitted by a light source with identical temporal profile, but which emits photons statistically independent of each other. This corresponds to the product of the mean photon count rates at times t and $t+\tau$. This information can be obtained by integrating all the single pictures as shown in the upper panel of figure 3-6. Here, any effects of correlations are averaged out. The normalised second-order correlation function,

$$g^{(2)}(t,\tau) = \frac{G^{(2)}(t,\tau)}{\left\langle \hat{b}^\dagger(t)\ \hat{b}(t) \right\rangle \left\langle \hat{b}^\dagger(t+\tau)\ \hat{b}(t+\tau) \right\rangle} \ , \tag{3.5}$$

is thus the measured photon-pair count rate at times t and $t+\tau$ as described above divided by the product of the mean photon count rates at the same times.

From $g^{(2)}(t,\tau)$, it is then possible to calculate a time-averaged $g^{(2)}(\tau)$ by dividing the sum of the photon pair detection rates by the sum of the squared mean photon numbers. This averaging over different times t does not significantly change the actual value of $g^{(2)}(\tau)$ for a certain value of τ, as the average is intensity weighted. This is further supported by the results presented in reference [Aßm10], where it has been shown that the actual value of $g^{(2)}(t,\tau=0)$ does not significantly change during the main part of an emission pulse from a microcavity.

3.3.3 Counteracting typical error sources

The photon correlation spectroscopy technique described above has significant advantages compared to common HBT setups, particularly considering the time resolution. Moreover, it avoids typical error sources present in HBT-like configurations, e.g. afterpulsing, crosstalk and misalignment of the two detectors. However, it also introduces new sources of errors. In this subsection, the most prominent error sources in photon correlation spectroscopy using the streak camera technique—namely photon reconstruction and timing jitter—will be discussed.

Photons that are detected by the streak camera will usually not fill a single pixel on the chip of the CCD camera imaging the phosphor screen, but will have a size of several pixels. A built-in algorithm of the streak-camera control software reconstructs the actual position of the photon on the screen by determining the centre of gravity of the intensity of the affected pixels. However, this routine can be fooled by inevitable local inhomogeneities of the phosphor screen. Thereby, it is possible that one photon can be accounted for as two. During the analysis of second-order correlations, this would result in a photon distribution with unreasonably high pair count rates for pixel distances shorter or equal to the typical radius r_{ph} of a single photon on the CCD chip, which then abruptly falls off step-like for distances larger than r_{ph}.

This problem can be solved by introducing artificially dead pixels within a radius of r_{ph} around the centre of gravity of any detected photon. All other photons detected within this area are discarded from further analysis. This way, any erroneous photon counts due to reconstruction problems are eliminated. As a drawback of this approach, a certain number of real photon detections are disregarded, too. These losses have to be accounted for when normalising the second-order correlation function. The dead pixels around each photon correspond to an effective loss in detector size for detecting another photon after the first one went down. As a consequence, the normalisation has to be modified by a factor of wA'/A, with A being the size of a bin on the screen, A' being the reduced size after introducing artificially dead pixels and w being a weighting factor. The weighting factor is necessary, as the mean number of photon counts is generally not distributed equally along the width of a bin. If artificially dead pixels are used in measurements of higher-order correlation functions, it is necessary to consider the decreasing effective detector size inside a time bin accordingly after each photon detection.

The second inherent source of error is timing jitter. Obviously, jitter-induced effects are directly noticeable when time-resolved correlations like $g^{(2)}(t,\tau)$ are investigated [Aßm10]. However, timing jitter has also a significant influence on the measured photon correlations $g^{(2)}(\tau)$ when the studied light source emits pulses of extremely short duration, as will be discussed in the following. To begin with, it should be mentioned that most quantities relevant for calculating second-order correlations are not sensitive to jitter: Even though the peak position of the detected signal and the number of detected photon pairs in a certain time bin will generally vary slightly in each single picture, the pulse shape, the τ-dependence of the photon pair count rate and the sum of all detected photon pairs will not depend on timing jitter.

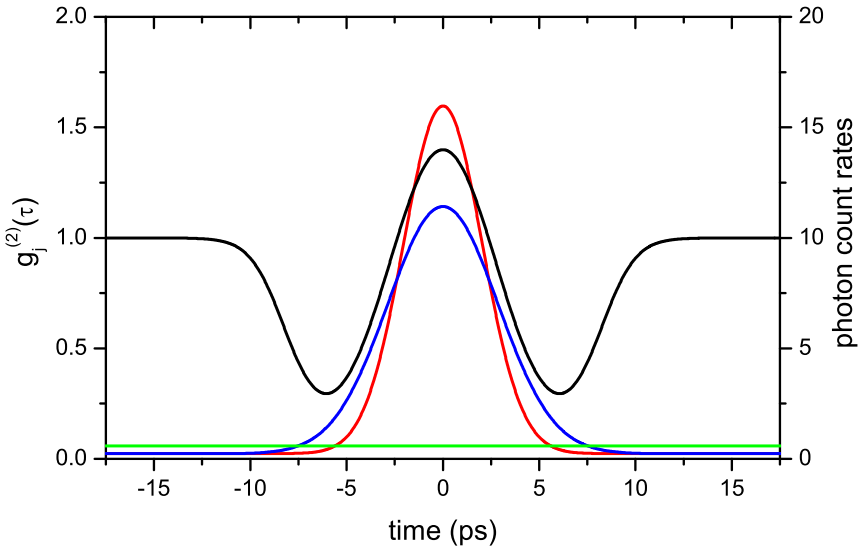

Figure 3-7: Theoretical example for the jitter-affected shape of $g_j^{(2)}(\tau)$ (black curve). The abscissa gives the delay τ for the black curve and the time t for the other curves. Red and blue curves give the photon pair count rates and squared mean photon count rates, respectively. The green curve represents the constant background noise count rate. The resulting $g_j^{(2)}(\tau)$ displays values larger, smaller and equal to unity, depending on which of the count rates gives the dominant contribution at a given τ.

Also, the time-integrated photon pair count rate [$G^{(2)}(\tau)$; compare equation (3.4)] is not affected by jitter. The mean photon count rate used for the normalisation, however, might be broadened due to timing jitter.

The effect of jitter on $g^{(2)}(\tau)$ can be modelled theoretically as follows. As a general example, the signal under investigation is assumed to be characterised by a Gaussian pulse shape $S(t)$ with amplitude of unity and standard deviation W as well as by a Gaussian jitter $J(t)$ with standard deviation J. The resulting mean photon count rate is then given by the convolution of both, given by another Gaussian $S_j(t)$. The latter is characterised by a standard deviation of $W_j = (W^2 + J^2)^{1/2}$. The lowest possible magnitude of the jitter is determined by the temporal response of the photocathode. In principle, it can be increased by instabilities of the trigger signal or the excitation laser used. Additionally, background noise has to be considered via a constant noise count rate r_n. This way, the jitter-affected $g_j^{(2)}(\tau)$ can be written as

$$g_j^{(2)}(\tau) = \frac{\iint \left[S(\tau_2) + r_n\right] \cdot \left[S(\tau + \tau_2) + r_n\right] \cdot J(t - \tau_2)\,\mathrm{d}\tau_2\,\mathrm{d}t}{\int \left[S_j(t) + r_n\right] \cdot \left[S_j(t + \tau) + r_n\right]\,\mathrm{d}t} \,. \tag{3.6}$$

This function is illustrated in figure 3-7. As can be seen, equation (3.6) mainly consists of three components, namely the photon pair count rates, the squared mean photon count rates and background noise. The photon pair distribution is generally narrower than the squared mean photon count rate, which directly results in artificial bunching around zero delay. When these two distribution eventually cross, $g_j^{(2)}(\tau)$ reaches values below unity. For even larger delay τ, the cross-correlation between the original signal and background noise becomes dominant and $g_j^{(2)}(\tau)$ returns to unity.

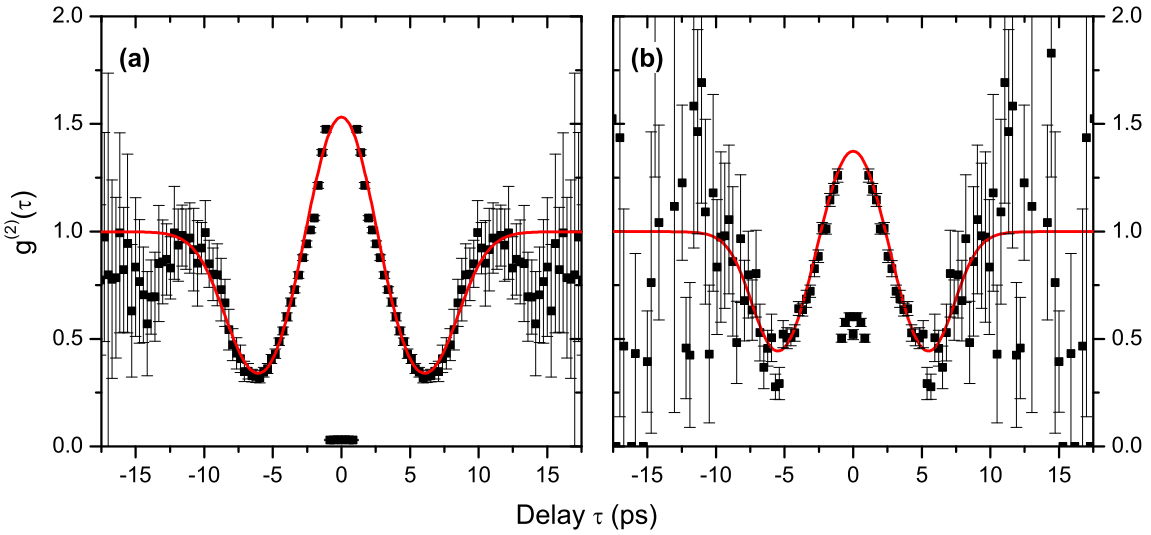

Figure 3-8: Jitter-induced second-order correlation function $g_j^{(2)}(\tau)$ of a pulsed laser for different streak camera settings. The pulsed laser has a FWHM pulse duration of 3.53 ps (corresponding to a standard deviation of 1.5 ps) and a centre wavelength of 768 nm. Experimental data are shown as black squares; the red solid line represents a fit to the data. Data points around $\tau = 0$ display values significantly below the actual correlation values, which is the direct consequence of introducing artificially dead pixels; see main text. These data points were excluded from the fit. Streak camera settings: (a) MCP gain 17, photon counting threshold 100, (b) MCP gain 42, photon counting threshold 170.

A direct way to demonstrate the validity of equation (3.6) is to analyse the second-order correlation function of a well-known laser source such as the picosecond-pulsed laser described in section 3.2. To this end, the mode-locked laser was configured to irradiate pulses with a full width at half maximum (FWHM) temporal duration of 3.53 ps, as evidenced by using a standard autocorrelator. The FWHM of the pulse duration corresponds to a standard deviation of $W = 1.5$ ps. A typical example of experimental results is shown in figure 3-8. In this analysis, the vertical bin size was set to the minimum of one pixel per bin, which equals a bin length of roughly 283 fs. At first sight, a significant reduction of $g_j^{(2)}(\tau)$ around zero delay is apparent. This is a direct consequence of introducing artificially dead pixels. For time delays larger than approximately one picosecond, this effect vanishes.

The red lines in figure 3-8 are fits to the data using equation (3.6). The fit yields the parameters $W = 1.5$ ps, $J = 1.80$ ps, and $r_n = 0.0015$ for the data shown in panel (a), while it results in the parameters $W = 1.42$ ps, $J = 1.38$ ps, and $r_n = 0.0033$ for the data shown in panel (b). The differences in the data and in the fit results demonstrate the importance of correct streak camera settings: When the threshold value of the photon reconstruction algorithm is set too low [as in panel (a)], the photon size on the screen becomes rather large, while the intensity at many of the pixels is not very different from the threshold value. In such a case, it is more difficult to distinguish between subsequent photons, thereby causing a slight underestimation at small delays in the range of $1\,\text{ps} < \tau < 3\,\text{ps}$. It also explains the large jitter value

of $J = 1.80\,\mathrm{ps}$ because the actual position of the centre of gravity of the intensity of two subsequent photons is hard to determine. On the other hand, when the photon counting threshold is set too high, as in panel (b) of figure 3-8, typically the jitter is calculated correctly, but the general uncertainty level increases. This can be seen in panel (b) where the error bars are much larger than in panel (a). In the case of the present streak camera, it was determined that the results are best when the photon counting threshold is set to 110. Under typical operation conditions, the timing jitter is found to be $J \approx 1.3$–1.4. It is thus crucial to choose the threshold value as well as the MCP gain voltage carefully. However, the exact parameter values should vary from one streak camera device to another, depending on the built-in MCP stage, the kind and condition of the phosphorous screens, and the CCD camera.

Generally, the experimentally most relevant quantities are the time-integrated equal-time correlations of second order. Provided that the noise count rate r_n is low, the measured correlation values can be corrected for pulses with Gaussian or similar temporal shape. In second order the real and measured equal-time correlations, $g^{(2)}(0)$ and $g_j^{(2)}(0)$ respectively, are then related as follows:

$$g_j^{(2)}(0) \;=\; g^{(2)}(0) \times \sqrt{1 + \left(\frac{J}{W}\right)^2}\,. \tag{3.7}$$

According to this equation, the deviations become significant when the jitter width J is on the order of 20% of the signal width W or larger. Thus, the timing jitter has to be taken into account when light sources with emission pulse durations below $W = 10\,\mathrm{ps}$ are investigated.

Chapter 4

Lasing Threshold of Quantum-Dot Micropillar Lasers

The lasing threshold is one of the most fundamental parameters of semiconductor lasers, especially with regard to large-scale commercial applications. The efficiency of a laser, and thus the actual threshold carrier density, is affected by different characteristic quantities. In order to achieve stable lasing operation, population inversion[1] has to be established inside the whole active medium. Consequently, the use of nanostructures as active media has become standard in low power laser diodes.

The most prominent outcome of both academic and industrial research aimed at the reduction of the threshold carrier density in semiconductor lasers is the vertical-cavity surface-emitting laser (VCSEL) [Cho97]. A typical VCSEL comprehensively consists of a microcavity made of DBR mirrors, an optical cavity layer with a thickness in the one-wavelength range, and a semiconductor nanostructure embedded as active medium in the cavity layer. While most of the commercially available VCSELs today feature quantum wells as the active medium, lasers using quantum dots (QDs) have attracted much interest in the past decade in academic research [Vah03, Rei10], especially as QD lasers are assumed to operate without requiring a full population inversion [Gie07]. The downside of lasers with small active medium volumes is that the optical gain per round trip is small, too. In order to counter this deficiency, the lifetime of the photons within the cavity has to be increased, which corresponds to maximising the cavity Q-factor. This is usually achieved by using microcavities with a high number of DBR layer pairs.

Of particular interest is the so-called β-factor of the lasing mode which is defined as the spontaneous emission rate into that specific mode divided by the total spontaneous emission into all available modes. The β-factor has a strong influence on the shape of the input-output (i/o) curve of a laser: The step-like nonlinearity in the emitted intensity of the lasing mode, as displayed by conventional lasers with $\beta \ll 1$,

[1] In semiconductor lasers, the lasing condition is defined by the Bernard-Duraffourg criterion which describes it in terms of quasi-Fermi levels of the states (i.e. bands) involved in the actual lasing transition [Ber61].

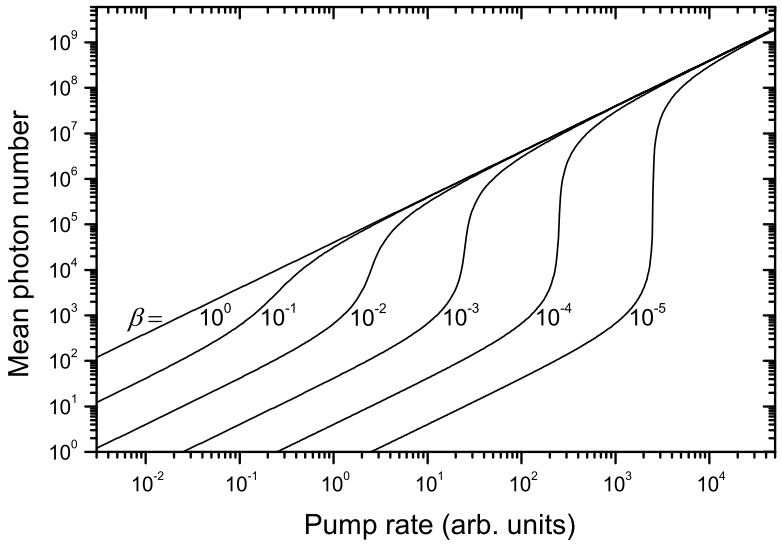

Figure 4-1: Input-output curves for lasers with different β-factors, as calculated using equation (4.1). The particular value of the β-factor is indicated.

becomes much smoother and finally disappears as $\beta \to 1$, thus realising the case of the so-called thresholdless laser [Mar88, Bjö91]. This change in the i/o-curve is shown for different β-values in figure 4-1. While conventional semiconductor-based lasers feature β-values in the range of 10^{-5} [Yam92], in the case of high-Q microcavities operating in the weak-coupling regime the β-factor can be substantially enhanced by taking advantage of the Purcell effect described in chapter 2.3.1. Micropillar cavities using quantum dots as optically active material placed at the central antinode of the electromagnetic field distribution are known to display considerable Purcell enhancement with Purcell factors F_P significantly larger than unity [Gér98, Sol01, Loh06].

Nonetheless, these enhancements of the laser efficiency lead to specific difficulties: the lasing threshold becomes very smooth, thereby complicating a direct identification of the onset of stimulated emission, as is obvious from figure 4-1. To compensate this drawback it has been suggested to use a combination of i/o-curve data, first-order correlations, and second-order correlations in order to characterise the lasing transition of high-Q, high-β microcavity lasers more accurately [Ric94, Wie10].

In this context, it has been shown that both the first- and second-order correlation functions display characteristic features that allow one to investigate the transition from spontaneous to stimulated emission in systems with a low number of emitters [Ulr07, Ate08, Wie09]. Nevertheless, the experimental techniques used so far to record second-order correlations suffer from disadvantages at low excitation powers. Hanbury Brown-and-Twiss setups do not have the appropriate time resolution as correlation effects occur only within the coherence time of the emission [Ate08], which typically is below 100 ps in the regime of spontaneous emission. The streak-camera technique described in chapter 3.3 does feature a time resolution in the picosecond range, but its quantum efficiency for emission wavelengths $\geq$ 900 nm—as typical for GaAs-based QD cavities—is too low to extract sufficient statistics at low signal intensities [Wie09].

The first aim of this chapter is to present and discuss results of comprehensive optical studies on GaAs-based micropillar cavities which include self-assembled QDs as the active medium (see sample description in section 4.1). These QD cavities operate in the weak-coupling regime, i.e. the system can be described by the bare exciton and photon states (compare chapter 2.3.1). A basic characterisation of the sample by means of micro-photoluminescence (micro-PL) measurements is given in section 4.2. In this context, the β-factor of the investigated cavities will be estimated from the measured i/o-curves. In the main part of this chapter, a discussion of the coherence properties of the cavities (section 4.3) is followed by an analysis of the evolution of the fundamental mode polarisation (section 4.4). Here, record values for both the coherence time and the degree of linear polarisation of QD micropillars are reported.

The second aim of this chapter is to provide a completion of a recently presented photon statistics analysis of quantum-dot micropillar lasers. Therefore, a theoretical model relating the first- and second-order correlation functions will be presented in section 4.5. Based on this theoretical model it will be possible to describe second-order correlations over the entire excitation power range from the thermal regime throughout the lasing transition up to the regime of stimulated emission. The chapter is summarised in section 4.6.

4.1 The GaAs-based Micropillar Sample Structure

The pillar microcavities investigated in the present work are mainly based on a planar AlGaAs heterostructure.[2] This planar microcavity structure was grown on a (001) oriented GaAs substrate by molecular beam epitaxy (MBE) [Löf05, Rei06]. A sketch of the layer sequence of the planar structure is shown in figure 4-2. A GaAs one-wavelength cavity layer with a thickness of 262 nm is sandwiched between the upper and lower cavity mirrors. The DBR mirrors are composed of 26-period (top) and 33-period (bottom) AlAs/GaAs stacks, respectively. Each layer pair in the DBR stacks consists of a 74 nm-thick AlAs layer and a 68 nm-thick GaAs $\lambda/4$ layer. With these parameters, the planar microcavity is essentially designed for a cavity resonance wavelength at about 900 nm at cryogenic temperatures.

The GaAs λ-cavity contains a single layer of self-assembled AlGaInAs quantum dots. By positioning the QD layer exactly at the centre of the one-wavelength cavity, thus at the antinode of the intra-cavity electromagnetic field, the light–matter interaction strength, i.e. the Purcell factor F_P, is maximised. The dot surface density of about $6 \cdot 10^9\,\mathrm{cm}^{-2}$ is relatively low compared to previous studies [Gér96, Gér98]; this low density especially favours increased cavity Q-factors as optical losses caused by band-gap absorption are reduced [Löf05].

[2]The pillar microcavity sample used for the studies presented in this chapter has been fabricated in the working group of Prof. Alfred Forchel at the Julius-Maximilians-Universität of Würzburg, Germany. The identifier of the sample is M2754-9-5A.

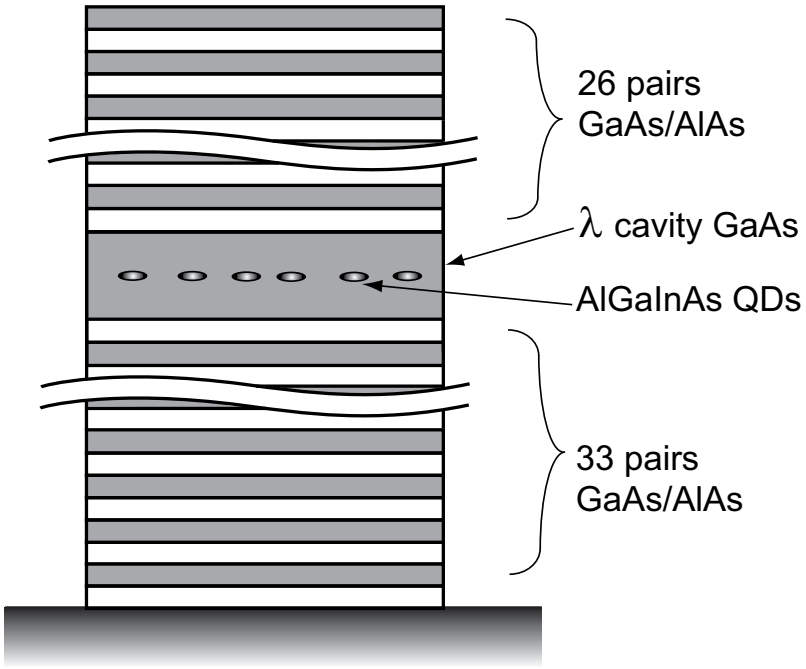

Figure 4-2: Sketch of the layer sequence of the investigated micropillar sample. A λ-cavity containing a single QD layer is sandwiched between the top and bottom DBR structure. For the present work micropillars with different diameters in the range of $d = 2\,\mu\text{m}$ to $d = 8\,\mu\text{m}$ were investigated. Demonstrative scanning electron microscopy images of micropillars similar to the ones investigated in the present work can be found in reference [Rei10].

In order to fabricate micropillars of cylindrical shape, the MBE-grown planar microcavity was further processed using high-resolution electron-beam lithography and plasma-induced reactive ion etching, as described in reference [Löf05]. In the present work, a sample containing micropillars with different diameters in the range of $1\,\mu\text{m}$ to $8\,\mu\text{m}$ is investigated.

All results presented in this chapter were obtained using the experimental setup described in chapter 3.1. The micropillar laser sample was positioned into the He-flow cryostat and glued to the cold finger of the cryostat with thermally conductive silver paint. All measurements were performed at a temperature of roughly 10 K unless indicated otherwise. As described in chapter 3.1, single micropillars could be accessed using a microscope objective mounted to a piezo-driven translation stage. The pillars were excited above the GaAs bandgap and the stop-band of the DBR structure by a continuous-wave diode laser with an emission energy of $\hbar\omega = 1.58\,\text{eV}$ corresponding to a wavelength of roughly 785 nm.

4.2 Characteristic Luminescence

In order to directly measure the PL of the micropillars, one arm of the Michelson interferometer (described in chapter 3.1) was blocked, thereby avoiding unwanted interference effects. Example micro-PL spectra of pillar cavities with different diam-

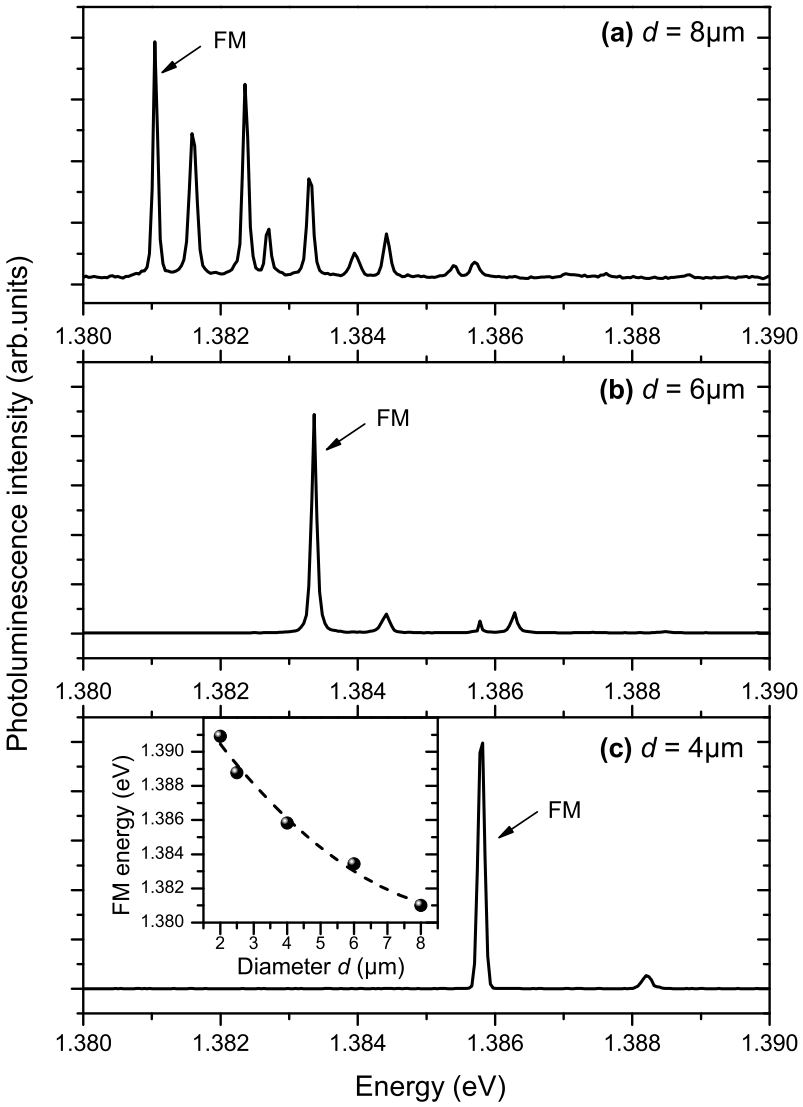

Figure 4-3: Micro-PL spectra measured on different GaAs-based micropillar cavities with diameters of (a) 8 μm, (b) 6 μm, and (c) 4 μm. The excitation power was in the range of roughly 1% of the individual lasing threshold power of each resonator. The FM of each cavity is indicated. Note that the different intensity scales are not comparable; typically the FM intensity of a thinner pillar is weaker. Inset: Circles represent the spectral position of the FM as a function of the micropillar diameter d; the dashed line is a fit using equation (2.20).

eters are shown in figure 4-3. These spectra were measured at excitation powers far below the lasing threshold, which will be discussed below.

As described in chapter 2.2, the structuring of the planar cavity towards a micropillar leads to a three-dimensional optical confinement, thus rising the energy of the fundamental mode (FM) of the cavity. From the experimental data, it becomes obvious that the energy of the FM is shifted from 1.381 eV to nearly 1.386 eV when decreasing the diameter from 8 μm to 4 μm. This shift in energy is summarised in the inset of figure 4-3(c) and is in good agreement with theoretical expectations as

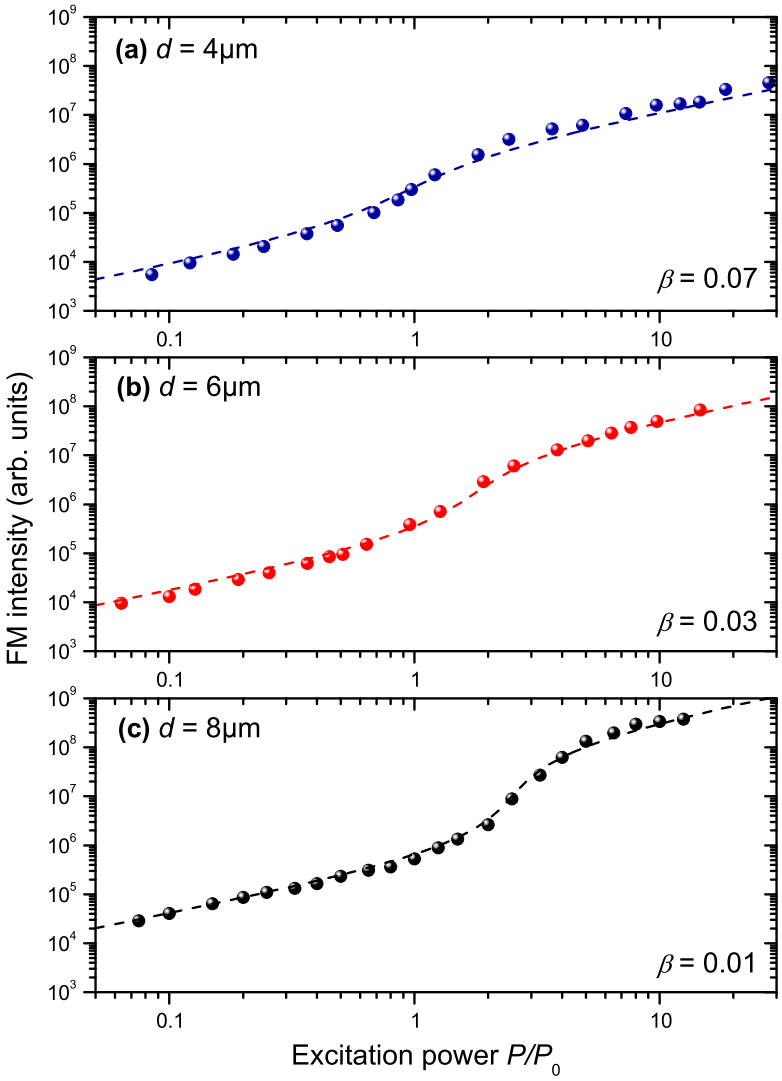

Figure 4-4: Input-output characteristics of the different micropillars. In this plot, only the X-polarised component of the FM is considered as it dominates the emission at high excitation powers. In all cases a smooth transition to lasing operation can be observed. The excitation power is normalised to the onset of the lasing transition region, which is found to be $P_0 = 92\,\mu\text{W}$, $131\,\mu\text{W}$ and $200\,\mu\text{W}$ for the micropillar with diameter $d = 4\,\mu\text{m}$, $6\,\mu\text{m}$ and $8\,\mu\text{m}$, respectively. The dashed lines are theoretical curves calculated using equation (4.1) and varying the values for the β-factor as indicated in the different panels.

shown by the fit using equation (2.20). Except for the micropillar with $d = 4\,\mu\text{m}$ with a spectral linewidth of the FM of $\Delta E = 110\,\mu\text{eV}$, the linewidth of the FM is below the resolution of the experimental setup which is roughly $100\,\mu\text{eV}$. In all cases, this yields promising high cavity Q-factors in the range of 10^4. Note also that the number of visible modes is decreasing when going from larger to smaller diameters, as the free spectral range between different cavity modes increases with stronger transverse optical confinement. Thereby, higher modes may be shifted to higher emission angles or possibly even to energies outside of the DBR stop-band. These results are in good agreement with literature [Gér96, Rei07, Rei10].

Theoretically, the FM should be twofold polarisation degenerate due to the rotational symmetry of the pillar cross-section. Likewise, it is clear that every deviation from perfect rotational symmetry should lift the degeneracy and result in two orthogonal, linearly polarised mode components. These components are generally polarised along one of the main axes of the pillar cross-section, which will be denoted as the X- and the Y-axes, corresponding to polarisation detection angles of $\vartheta = 0^\circ$ and $\vartheta = 90^\circ$, respectively. The splitting in energy between these two FM components depends strongly on the degree of ellipticity of the pillar cross-section [Gay98]. As the observed FM linewidths are resolution-limited, such a splitting cannot be measured with the present experimental setup. Nevertheless, the mode polarised along the X-direction is found to strongly dominate the emission at high excitation powers in all cavities, as will be discussed in more detail in section 4.4.

In order to characterise the transition towards lasing operation, the excitation-power dependence of the X-polarised mode emission was measured. The resulting i/o-curves are shown in figure 4-4 on a double-logarithmic scale. Independent of the diameter, an s-shaped smooth transition from the regime of dominating spontaneous emission to the regime of dominating stimulated emission can be observed, in qualitative agreement with results reported from investigations on similar micropillar structures [Ate08, Rei06]. For better comparison all excitation powers are normalised to the excitation power at the onset of the lasing transition region denoted as P_0. Under identical experimental conditions, the actual value of P_0 is found to decrease for smaller pillar diameters. This is expected for different reasons: First, the number of QDs in which the carrier population has to be inverted should be fewer for smaller pillar cross-sections. Second, as can be seen from figure 4-3, the available mode volume in the cavity, in which the QDs can radiate, is much smaller in thinner pillars.

The i/o-curves shown in figure 4-4 do also allow for an estimate of the β-factor of the lasing mode. In a theoretical model using a two-level system to describe the lasing transition, the relation between the pump rate p and the mean photon number in the lasing mode $\tilde{n}$ is described by [Ric94]

$$\tilde{n} = (2\kappa\beta)^{-1} \cdot \left[-(\kappa - \beta p) + \sqrt{(\kappa - \beta p)^2 + 4\kappa\beta^2 p} \right] \quad . \tag{4.1}$$

Here, κ is a second fit parameter that accounts for the cavity decay rate. It has been pointed out in reference [Gie07] that models using simple two-level systems are not able to incorporate semiconductor specific features such as Pauli blocking, Coulomb interaction and modifications of the source term of spontaneous emission. While these features have a considerable effect on the second-order correlation function—as will be described in more detail in section 4.5—the influence on the i/o-curve seems to be negligible for the case of the cavities discussed here.

As displayed in figure 4-4, equation (4.1) is indeed capable of describing the measured i/o-curve data. The β-factor was varied in order to best fit the s-shaped transition from thermal to coherent emission. This way, the β-values of the investigated microcavities can be estimated to be $\beta = 0.07$ (pillar diameter $d = 4\,\mu\text{m}$), 0.03

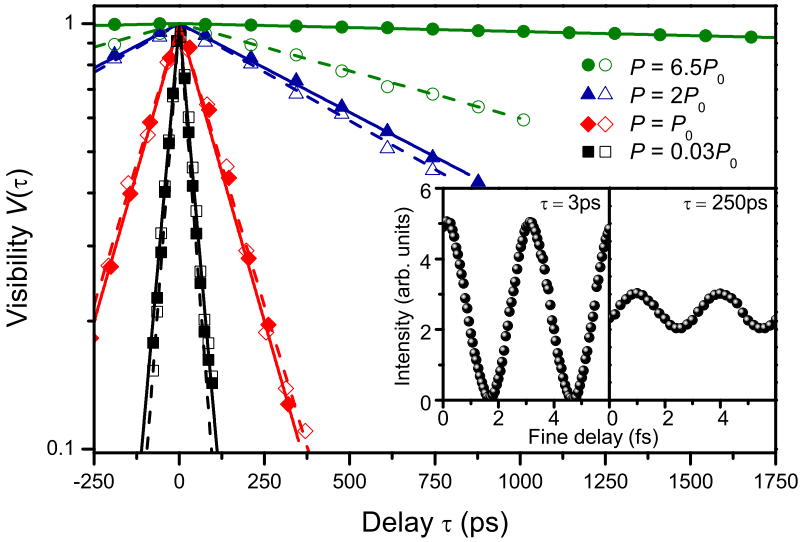

Figure 4-5: Visibility curves of the emission from the two polarisation-split components of the 8 µm-pillar's FM for different excitation powers. Solid (open) symbols represent visibility curves detected in X-direction (Y-direction). The solid (dashed) lines are fits to X-data (Y-data), which are performed using an exponentially decaying function. From these fits the coherence time of radiation can be deduced, as shown in figure 4-6. Inset: Typical high-resolution interference fringes, measured at a delay time τ close to 0 ($V = 0.98$) and at 250 ps ($V = 0.20$) for $P = P_0$ (X-polarisation).

($d = 6\,\mu$m), and 0.01 ($d = 8\,\mu$m), respectively. As expected, this trend is directly reflected in the shape of the kink in the i/o-curve which appears more pronounced for the large-diameter pillar.

4.3 First-Order Coherence

The coherence time of radiation is probably the most important property of a laser. Also, it has been suggested that the evolution of the coherence time can be used as an indicator in order to clearly identify the lasing transition of high-β lasers [Wie10]. To determine the coherence time experimentally, the high-resolution Michelson interferometer presented in chapter 3.1 was utilised. From the recorded interference pattern the the visibility V has to be derived by fitting a sinusoidal function to the fringes, as shown for two different delay times τ in the inset of figure 4-5. As described in equation (3.2), the resulting delay-time dependent visibility $V(\tau)$ is directly proportional to the absolute value of the first-order correlation function $g^{(1)}(\tau)$. Finally, the coherence time can be computed using equation (2.43).

Power dependent visibility measurements with the polarisation detection along one of the main axes were performed. Example visibility curves of the emission from the FM of the 8 µm-pillar are shown in figure 4-5. Solid (open) symbols represent visibility curves detected along the X-axis (Y-axis). The main observation is the fact that the visibility at delay times $\tau \neq 0$ is significantly enhanced for both modes

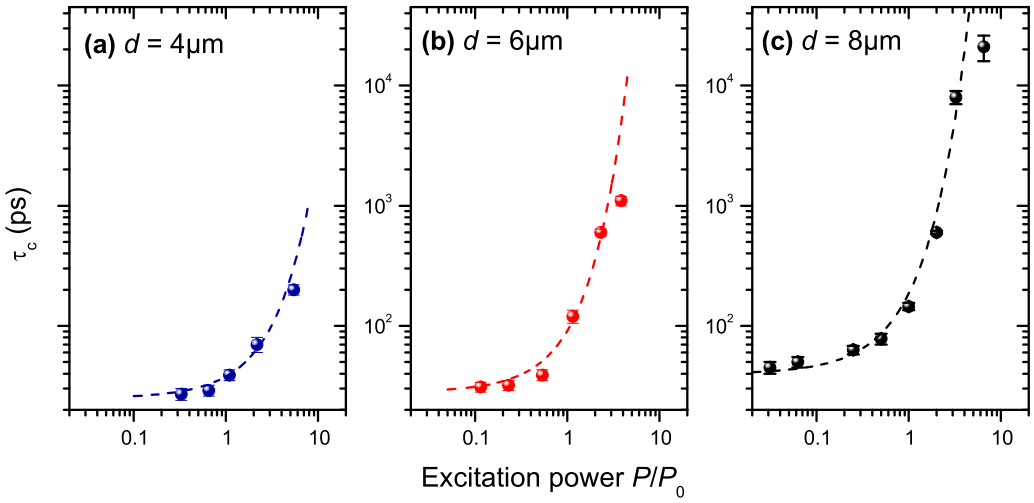

Figure 4-6: Excitation power dependence of the coherence time τ_c of the different micropillars. Only the X-polarised component of the micropillars' FM was evaluated, as in figure 4-4. The excitation power is normalised to the onset of the lasing transition region, as described in figure 4-4. In all cases the evolution of the coherence time can essentially be described by an exponential function. As expected, longer coherence times were observed for micropillars with lower values of the β-factor.

at higher excitation powers, corresponding to longer coherence times at higher excitation powers. Furthermore, the experimental data can be nicely described by an exponential function

$$V(\tau) = \left| g^{(1)}(\tau) \right| = \exp\left(-|\tau|/\tau_c\right) . \tag{4.2}$$

By fitting the data using equation (4.2), one can directly compute the coherence time τ_c. The results of these fits are summarised in figure 4-6 for the case of the FM component polarised along the X-axis. In all cases, the increase of τ_c follows an exponential function. In the case of the 8 µm-pillar, τ_c increases from (45 ± 5) ps up to (21 ± 5) ns when the pump power is increased from $0.03P_0$ to $6.5P_0$. This represents a record value for the coherence of the emission of quantum-dot seeded micropillars. The weaker mode (polarised along Y), however, displays a less substantial increase in τ_c, from (39 ± 5) ps below threshold $(0.03P_0)$ up to (2.0 ± 0.2) ns in the lasing regime $(6.5P_0)$. The discrepancy in τ_c at high excitation powers is indeed expected, as the X-mode also dominates the emission in terms of significantly higher intensity, as will be discussed in section 4.4.

It is also important to note that the actual values of τ_c are strongly influenced by the β-factor. While higher values of the β-factor were determined for thinner micropillar diameters, the coherence time becomes shorter for these. Due to stronger contribution of spontaneous emission into the lasing mode, the effective coherence time of the lasing mode is shorter for high-β lasers. This is in line with other reports and with the mentioned theoretical framework; compare reference [Ate08].

From the measured coherence times, it is also possible to estimate the Q-factors of the FM components. They can be derived from the lowest measured values of

τ_c using the relation $\Delta E = 2\hbar/\tau_c$. This way, the cavity quality factors have been calculated to be $Q_4 \sim 28,000$ ($d = 4\,\mu$m), $Q_6 \sim 33,000$ ($6\,\mu$m), and $Q_8 \sim 47,000$ ($8\,\mu$m).

As an exponential increase of the coherence time around the lasing threshold region was observed in the emission from all micropillars, the experimental determination of $g^{(1)}(\tau)$ was shown to be indicative of the position of the laser threshold. Besides the i/o-curves discussed above, the degree of polarisation and second-order correlations must be considered as well; see the following sections of this chapter.

Finally, it is noted that in recent literature a Gaussian shape of the visibility curve below the laser threshold has been observed [Ate07, Ate08]. In a theoretical framework [Wie10], this has been explained to be due to quantum-mechanical interaction processes which are connected to the degree of population inversion in the quantum-dot ensemble. This behaviour cannot be observed in the emission from the present samples. One reason might be that the cavities investigated in the work by Ates et al. were thinner, with diameters of $4\,\mu$m at maximum. Also, it is possible, though unlikely, that a Gaussian-like visibility curve would have been observed at even lower excitation powers than those presented here. Unfortunately, the true physical origin of such a change in the shape of $g^{(1)}(\tau)$ is not yet fully understood. However, despite the small differences in the shape of the first-order correlation function at low excitation, in general, the results presented here remain in good agreement with theory [Wie10].

4.4 Degree of Linear Polarisation

In micropillars with a perfect circular cross-section the FM is generally twofold degenerate. It has been shown that this degeneracy can lead to unfavourable effects on the laser performance, e.g. polarisation instabilities and mode partition noise in VCSEL devices [Kuk95]. Also, in the field of single-photon sources, where polarisation-encoded quantum cryptography schemes shall be implemented, polarisation control is of major importance. This problem can be circumvented, however, by using micropillars with elliptical cross-section [Mor01, Uni05].

As mentioned above, the emission from the FM of the micropillars investigated in this work has been observed to be polarisation-split into two orthogonal, linearly polarised modes. In the previous sections, the discussion was mainly focused on the FM component polarised in the X-direction, which was found to dominate the lasing emission at high excitation powers. In this section, the evolution of the degree of linear polarisation with excitation power will be analysed in more detail. Here, the discussion will be restricted on the micropillar with $d = 8\,\mu$m.

In panel (a) of figure 4-7, the integrated intensity of the fundamental cavity mode is shown as a function of the polarisation detection angle ϑ. The plot is normalised with respect to the maximum intensity, which is always observed at $\vartheta = 0°$. Generally,

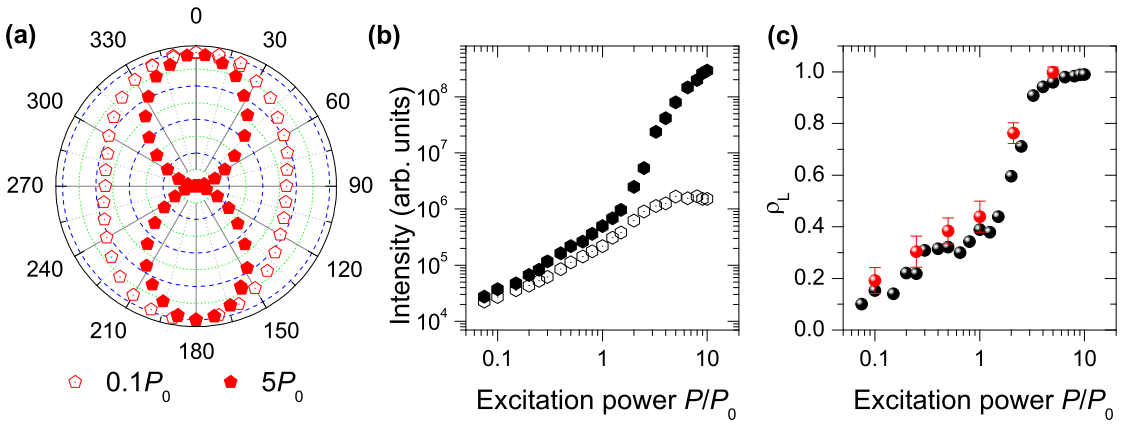

Figure 4-7: (a) Polar plot of the total emission intensity of the FM as a function of the polarisation angle ϑ. Almost full linear polarisation ($\rho_L = 0.99 \pm 0.01$) along $\vartheta = 0^\circ$ is observed at $5P_0$. (b) Input-output characteristics of the X-polarised (filled symbols) and Y-polarised (open symbols) component of the FM. (c) Evolution of the degree of polarisation ρ_L with increasing excitation power. Red symbols are obtained from sinusoidal fits using full polarisation data as shown in (a); black symbols are calculated by relating the emission intensities of the X and Y component shown in (b).

the angle-dependent intensity $I(\vartheta)$ can be described by the relation

$$I(\vartheta) = 0.5 \cdot [1 + \rho_L \cos(2\vartheta)] \ , \tag{4.3}$$

where the degree of linear polarisation ρ_L is characterised by the intensities along the main micropillar axes:

$$\rho_L = \frac{I(0^\circ) - I(90^\circ)}{I(0^\circ) + I(90^\circ)} \ . \tag{4.4}$$

At low excitation powers ($P = 0.1P_0$), the degree of linear polarisation is found to be moderate with $\rho_L = (0.19 \pm 0.05)$. As mentioned above, the X-mode dominates the emission intensity above threshold. This is confirmed in figure 4-7(a), where almost full linear polarisation with $\rho_L = (0.99 \pm 0.01)$ can be observed at $5P_0$.

A second possibility to determine the degree of polarisation is to directly compare i/o-curves measured at polarisation detection angles of $\vartheta = 0^\circ$ and $\vartheta = 90^\circ$. The i/o-curves measured along the X-axis and the Y-axis, are shown in panel (b) of figure 4-7. Note the large differences in intensity in the lasing regime. The degree of polarisation can then be calculated using equation (4.4). In panel (c) of figure 4-7, the resulting values for ρ_L obtained from angle-resolved measurements at fixed excitation power [panel (a)] and from i/o-curves at fixed detection angle are compared. The results seem to be very well reproducible.

In the following, another possibility to determine the degree of linear polarisation will be presented. The advantage of this method is that the evolution of ρ_L and of the coherence times of both FM components can be measured simultaneously. In order to do this, interferometric measurements must be performed. In section 4.3, visibility curves were recorded for the X- and the Y-mode separately, corresponding to polarisation detection angles of $\vartheta = 0^\circ$ and $\vartheta = 90^\circ$, respectively. When the detection

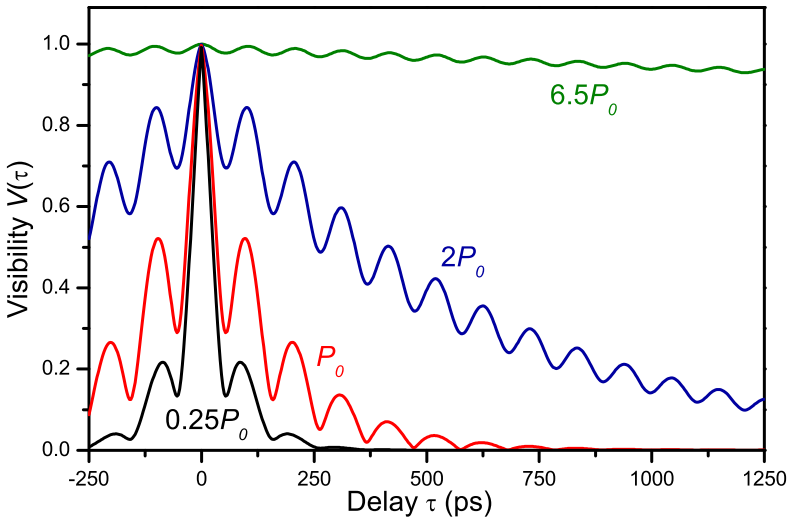

Figure 4-8: Calculated visibility curves for a polarisation detection angle $\vartheta = 45°$, i.e. exactly in between of the micropillar's main axes. The curves were generated using equation (4.5). Parameter values were taken from the results presented in section 4.3 and assuming an energy splitting between the two FM components of 40 µeV.

angle is set to $\vartheta = 45°$, both FM components contribute to the signal, resulting in beats.[3] Assuming a Lorentzian spectral shape for each of the cross-polarised modes, the resulting visibility curve can be described by a combination of two exponentially decaying functions and reads

$$V(\tau) \sim \left[\mathcal{I}_X^2 + \mathcal{I}_Y^2 + 2\,\mathcal{I}_X\,\mathcal{I}_Y \cos(\Delta\omega\tau)\right]^{1/2} \quad . \tag{4.5}$$

Here, $\mathcal{I}_i = \alpha_i I_i \exp\left(-|\tau|/\tau_c^i\right)$ with $i = X, Y$, and I_i and τ_c^i representing the intensity and the coherence time, respectively, of the different FM components. The transmission coefficient of polarisation i through the optical elements (i.e. the beam splitter) is accounted for by α_i.[4]

In order to allow for a better comparison with the results presented in the previous section, equation (4.5) was used to simulate the expected results of visibility curve measurements at a polarisation detection angle of $\vartheta = 45°$. Here, values for the coherence times of the X- and the Y-mode as determined from figure 4-5 as well as values for the relative intensities from figure 4-7(c) were employed. As the linewidth of the FM of the 8 µm-pillar is narrower than the experimental resolution of 100 µeV, for the simulations the energy splitting between X and Y is assumed to be 40 µeV. The simulated curves are shown in figure 4-8. In all cases, clear oscillations can be seen. Also, their amplitude decreases with increasing excitation power, which reflects the increase of the degree of linear polarisation.

Visibility curves experimentally measured at $\vartheta = 45°$ are shown in figure 4-9. As expected, the period of the oscillations does not depend on the pump power.

[3] Such oscillations have been observed in reference [Ate07], but have not been analysed further except for the oscillation period.

[4] The transmission ratios are $\alpha_X^{-1} = 0.51$ and $\alpha_Y^{-1} = 0.43$.

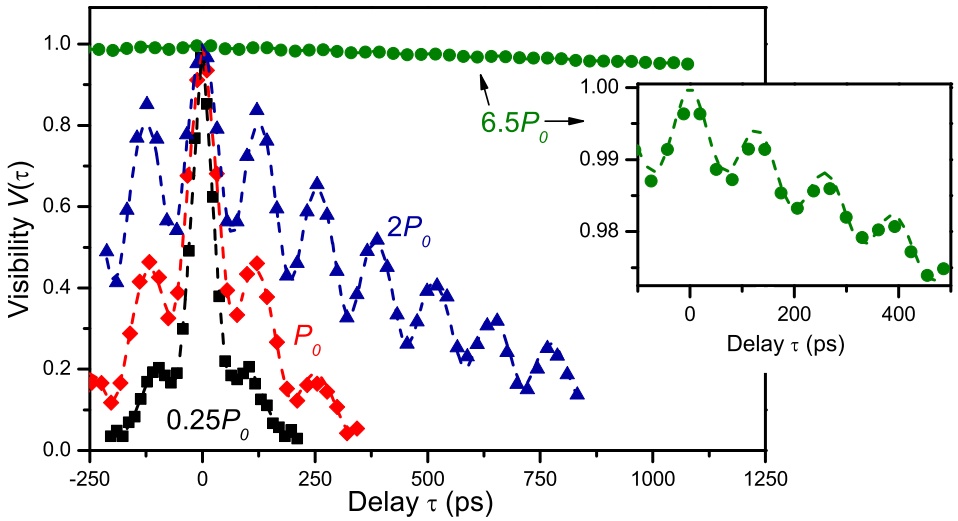

Figure 4-9: First-order correlation function of the 8 µm-pillar's FM, measured at polarisation detection angle $\vartheta = 45^{\circ}$, thus exactly in between of the micropillar's main axes. The inset shows an enlarged visibility curve with remains of oscillatory behaviour at $P = 6.5P_0$. The curves are fits obtained using equation (4.5). The actual results of the fits are presented in figure 4-10.

However, it changes from one micropillar to another. In the case of the 8 µm-pillar an oscillation period of roughly 120 ps is observed. This corresponds to an energy splitting between the two cross-polarised modes of $\hbar\Delta\omega = (35 \pm 3)\,\mu\text{eV}$, which lies in the expected range. The power dependence of the degree of linear polarisation derived from the fits is shown in figure 4-10(a). As expected, at low powers the value of ρ_L is rather small and in agreement with $\rho_L \sim 0.2$ obtained from figure 4-7. The degree of polarisation reaches values in the range $\rho_L \approx 0.2$–0.4. In this regime both modes contribute significantly leading to polarisation beats with large amplitudes, which is undesirable for laser operation. It is only at excitation powers well above the threshold region that the X-polarised mode finally dominates the emission which results in polarisation stable operation with $\rho_L = 0.995 \pm 0.005$, in line with the data presented in figure 4-7. However, oscillations can still be observed in the regime of stimulated emission above threshold, as can be seen from the inset of figure 4-9.

A similar behaviour is found in the evolution of the coherence times, as shown in figure 4-10(b). Below the threshold, the coherence times of both modes are comparable. This also means that their corresponding Q-factors are close to each other: here, using again the lowest measured coherence times, i.e. $\tau_{c,X} = (48 \pm 6)\,\text{ps}$ and $\tau_{c,Y} = (42 \pm 6)\,\text{ps}$, the Q-factors are found to be $Q_X \sim 50,000$ and $Q_Y \sim 44,000$, respectively. These quite similar Q-factors are indicative of the small ellipticity of the pillars [Dar06]. Furthermore, while $\tau_{c,X}$ and $\tau_{c,Y}$ both increase significantly in the lasing transition region, $\tau_{c,X}$ increases much more strongly at $P > P_0$ and reaches a value of $(20 \pm 4)\,\text{ns}$ at an excitation power of $6.5P_0$. Differences in the actual values of the coherence times with respect to those derived in the previous section are attributed to the increased level of uncertainty in the fitting procedure in the oscillating case due to the large number of parameters.

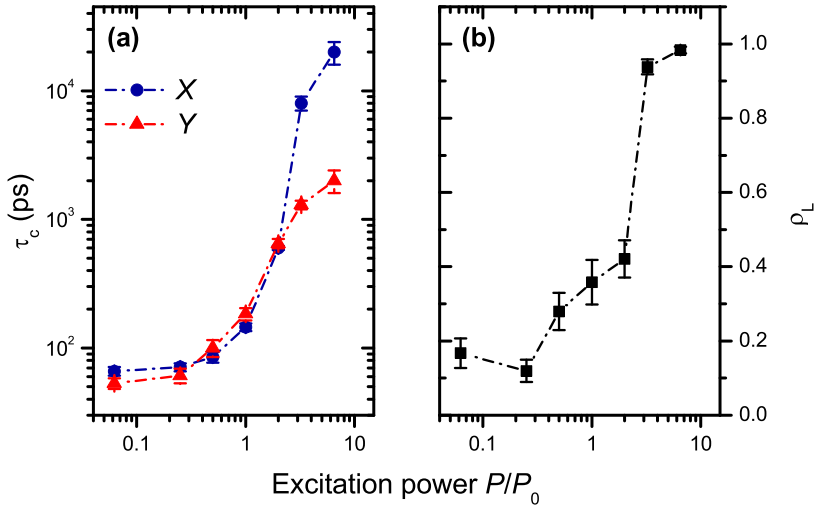

Figure 4-10: (a) Excitation power dependence of the coherence time τ_c of the different components of the 8 µm-pillar's FM. (b) Degree of linear polarisation ρ_L of the emission from the FM. Data in both panels were obtained from fits to the results shown in figure 4-9. Compare also with figures 4-6 and 4-7.

The above described observation can be explained by a residual, comparatively small degree of ellipticity of the micropillar cross-section. However, in order to ensure that the direction of polarisation is not imprinted by the excitation laser, the direction of polarisation of the linearly polarised excitation laser was rotated. Thereby, the direction of polarisation of the micropillar emission was found to be independent of the polarisation of the pump. Consequently, the characteristic direction of polarisation is indeed an intrinsic feature of the given micropillar.

The domination of a specific linearly polarised microcavity mode might also be due to tuning of certain exciton transitions out of or into resonance with the X-mode at high excitation powers. As the exact position of the exciton transition is very sensitive to changes of the lattice temperature, temperature-dependent first-order correlation measurements on an auxiliary micropillar with $d = 8\,\mu\text{m}$ were performed. As shown in figure 4-11, an increase of the sample temperature up to 77 K does not significantly affect the coherence and polarisation properties. Here, P_0 denotes the threshold at 10 K. The higher lattice temperature leads only to an increase of the actual laser threshold value. This can be seen from lower visibility values at $2P_0$ and 77 K as compared to 10 K and is related to stronger contributions of non-radiative recombination processes. A further important finding lies in the actual coherence time of the X-mode above threshold at 77 K. It is found to be (18 ± 5) ns and therefore only marginally lower than at 10 K. These results also underline the suitability of GaAs-based QD micropillars for laser applications at elevated temperatures [Böc08, Rei08].

To summarise this section, a detailed analysis of the FM polarisation was performed. The evolution of the degree of linear polarisation with the excitation power was determined in three different ways, showing concordant results. First-order correlation measurements at detection angle $\vartheta = 45^\circ$ were introduced, exhibiting characteristic oscillatory behaviour. This method allows for a direct measurement of the

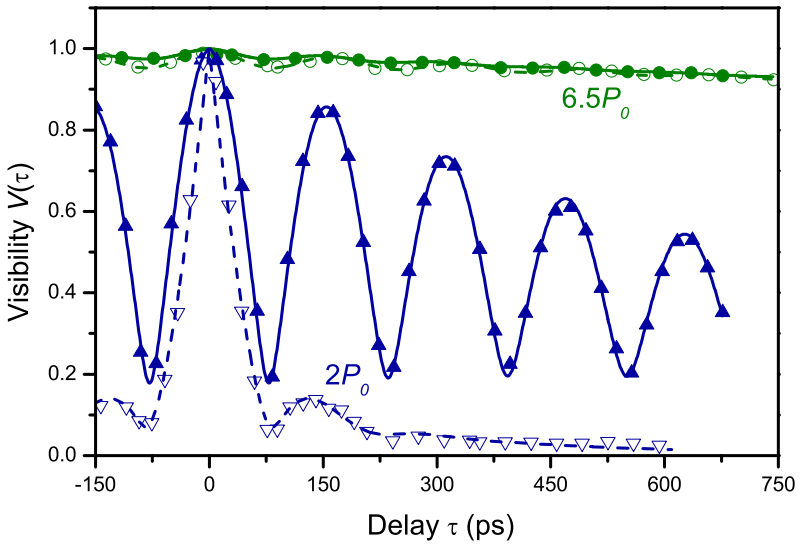

Figure 4-11: First-order correlation function ($\vartheta = 45°$) of the FM of a different micropillar with $d = 8\,\mu\text{m}$ at excitation powers of $2P_0$ (blue triangles) and $6.5P_0$ (green circles). Solid (open) symbols represent data taken at 10 K (77 K). For this microcavity the lasing transition region started at $P_0 = 240\,\mu\text{W}$ (10 K) and at $P_0 = 290\,\mu\text{W}$ (77 K), respectively.

coherence times, the relative intensities as well as the energy splitting of the two FM components. The presented results can be explained with the existence of an initial inequality in the mode strengths related to an elliptical pillar cross-section, which manifests itself by slightly linearly polarised emission at low excitation powers. Although the intensities, the coherence times, and the Q-factors are found to be comparable in the low excitation power regime, the X-mode finally prevails above the lasing threshold. Considering the polarisation and coherence properties derived above, one may define a threshold for this QD laser as the point where the single mode starts to dominate, namely $6.5P_0$, which is situated at the higher plateau of the s-shaped i/o-curve.

4.5 Interdependence of Correlations of First and Second Order

As mentioned above, additionally to i/o-curves, first-order correlations and the degree of linear polarisation, it is necessary to evaluate the photon statistics of the emission from a high-β laser in order to best characterise the lasing threshold. Using the streak-camera technique presented in chapter 3.3, the second-order correlations of the FM of the 8 µm-pillar have been investigated previously [Wie09]. However, statistically relevant measurements were only possible in the excitation power range at and above the lasing threshold. The main cause for the lack of reliable data in the thermal emission regime was the low quantum efficiency of the S-20 photocathode inside the streak device in the spectral region around 900 nm. In this section, a method to overcome this deficiency is introduced and applied.

In order to overcome the mentioned limitation and to fully characterise the lasing transition, a theoretical model is developed that relates first- and second-order correlations. This way, it is demonstrated that experimental results from $g^{(1)}(\tau)$ measurements, i.e. the coherence time of radiation, can be used to extend the accessible excitation power range for equal-delay time photon statistics into the thermal regime below threshold.

First, a macroscopic radiating system in the regime of spontaneous emission is considered. The interdependence of first- and second-order correlations is then given by the Siegert relation:

$$g^{(2)}(\tau) = 1 + \left| g^{(1)}(\tau) \right|^2 \ . \tag{4.6}$$

This relation assumes that the different emitters contributing to the total radiation act independently, so that no coherence can build up and lasing with $g^{(2)}(0) = 1$ cannot occur. As described in chapter 2.4, photon bunching occurs only within the coherence time of the emission. This can be seen when combining equations (4.2) and (4.6) and, in particular, results in $g^{(2)}(0) = 2$ since $g^{(1)}(0) \equiv 1$. Furthermore, quantum light emission with $g^{(2)}(\tau) < 1$ cannot occur in this case. This is indeed plausible as a large number of emitters is involved.

Consequently, whenever second-order correlation values below 1 are measured, only a very limited number of emitters can be contributing to the light generation. The observation of photon anti-bunching generally occurs when single-photon sources are investigated [Lou05]. However, a significant drop of second-order correlations below unity has also been observed in the photon statistics of the high-Q micropillar discussed in this chapter, as demonstrated in reference [Wie09]. This suggests that a low number of QDs contributing to the emission of the X-component of the cavity's FM.

Such a reduced number of active emitters, say N, can be taken into account in the second-order correlation function by adapting a model first developed in the field of quantum optics with atoms [Car78]. For this purpose, the total electric field $E_N(t)$ has to be described as the superposition of the electric field $E_i(t)$ irradiated by each single emitter i:

$$E_N(t) = \sum_{i=1}^{N} E_i(t) \ . \tag{4.7}$$

Assuming the N emitters to be effectively equal and presupposing the absence of background noise, the overall second-order correlations of N emitters can be expressed as [Car78]

$$G_N^{(2)}(\tau) = N G_A^{(2)}(\tau) + N(N-1) \cdot \left[I_A^2 + \left| G_A^{(1)}(\tau) \right|^2 \right] \ , \tag{4.8}$$

where, $I_A = \langle E_i^- E_i^+ \rangle$ is the intensity of the radiation from a single emitter, and $G_A^{(1)}(\tau)$ and $G_A^{(2)}(\tau)$ are the corresponding first- and second-order correlation functions, respectively. In order to obtain the normalised correlation function $g_N^{(2)}(\tau)$, equation (4.8) has to be divided by $|G^{(1)}(0)|^2 = (NI)^2$. It is then readily shown that the normalised second-order correlation function of a N-emitter system can be

written as:[5]

$$g_N^{(2)}(\tau) = \frac{g_A^{(2)}(\tau)}{N} + \left(1 - \frac{1}{N}\right)\left[1 + \left|g^{(1)}(\tau)\right|^2\right] \ . \tag{4.9}$$

Here, $g_A^{(2)}(\tau) = 1 - \exp(-|\tau|/t_\mathrm{d})$ is the intensity autocorrelation function of the electric field emitted by a single QD, which exhibits the well known anti-bunching behaviour. It is assumed here that the system can exhibit perfect anti-bunching. In general, this behaviour may be deteriorated by a stray light background, e.g. as shown in reference [Mic00]. The parameter t_d is the characteristic time describing the relaxation back to non-quantum light emission for later τ. For very weak excitation of the QD, t_d is just given by the spontaneous emission decay time τ_sp. This also includes resonator-induced effects such as Purcell enhancement. Higher pump rates generally also lead to faster decay and shorter t_d times, which then has to be written as $t_\mathrm{d}^{-1}(P) = 1/\tau_\mathrm{sp} + W(P) + W_\mathrm{cav}(P)$. Here, $W(P)$ accounts for faster re-excitation of the QD, whereas $W_\mathrm{cav}(P)$ includes emission events that are due to stimulation by intra-cavity photons.

Besides the anti-bunching term just discussed, the right hand side of equation (4.9) contains also a bunching term similar to the one in the Siegert relation, which may, however, also be smaller than 1, depending on the actual value of N. Both terms are weighted by coefficients determined by the number of emitters: For $N = 1$, only $g_A^{(2)}(\tau)$ adds to the overall correlations, while bunching disappears. For increasing N, the anti-bunching term decreases continuously, while the second term simultaneously gains in importance. In the limit of an infinite number of emitters, the Siegert relation is recovered.

To describe the variation of $g_N^{(2)}(\tau)$ with excitation power, and incorporate the threshold to stimulated emission and the lasing regime, further modifications are necessary. In this regime, $g_N^{(2)}(\tau)$ has to drop to unity for a large number of emitters. Therefore, the contribution of the bunching component in equation (4.6), $|g^{(1)}(\tau)|^2$, has to be reduced continuously for increasing excitation power and increasing cavity photon number. This can be achieved by introducing a phenomenological, excitation-power dependent factor $\chi_1(P)$:

$$g_N^{(2)}(\tau) = 1 + \chi_1(P)\left|g^{(1)}(\tau)\right|^2 \ . \tag{4.10}$$

Clearly, χ_1 must take the value 1 in the spontaneous emission regime, while it has to be zero for pure lasing. The drop from 1 to 0 has to occur within the laser threshold range. Generally, χ_1 can be expected to depend not only on the pump rate of photons into the resonator, but also on the photon loss rate, i.e. on the Q-factor of the cavity.

When going to a finite emitter number, this scaling factor has to be maintained. Additionally, the anti-bunching behaviour needs to be softened at and above the lasing threshold. This can be obtained by introducing another scaling factor $\chi_2(P)$ within the first term of equation (4.9), which is then rewritten as:

$$g_N^{(2)}(\tau) = \frac{1}{N}\left[1 - \chi_2 \exp\left(-\frac{|\tau|}{t_\mathrm{d}}\right)\right] + \left(1 - \frac{1}{N}\right)\left[1 + \chi_1\left|g^{(1)}(\tau)\right|^2\right] \ . \tag{4.11}$$

[5] See appendix A for details of the derivation of equation (4.9).

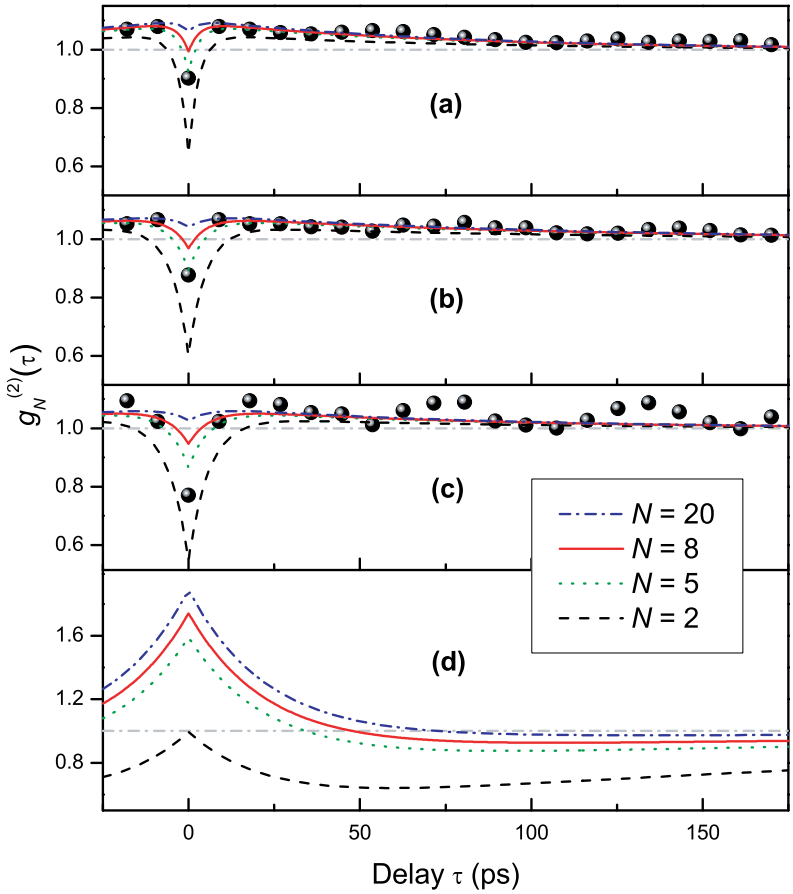

Figure 4-12: Second-order intensity correlation function of the 8 µm pillar's FM at excitation powers of (a) $4P_0$, (b) $2P_0$, (c) P_0 and (d) $0.03P_0$. The figure shows both experimental results from streak camera measurements (black spheres), as well as simulations using equation (4.11) taking into account the coherence times derived from $g^{(1)}(\tau)$ measurements shown in figure 4-5. At very low excitation powers [panel (d)] no measurements could be achieved due to limited sensitivity of the streak device. Here, the expected parameters $\chi_1 = \chi_2 = 1$ as well as $t_\mathrm{d} = 250\,\mathrm{ps}$ were used for the calculations; see main text.

Here, χ_2 has to depend on the photon generation and loss rate. In the regime of spontaneous emission with a negligible photon number in the resonator χ_2 should approach unity. With increasing excitation power the average number of intra-cavity photons increases, which reduces possible anti-bunching effects, as two photons may then be emitted at the same time. For very high photon densities χ_2 therefore has to drop to zero. In reference [Wie09] it has been shown that for the resonator under investigation quantum light emission can occur in the threshold region and above, so that even at those excitation powers anti-bunching is important, while the bunching effects are already minimised.

It should be noted that equation (4.11) is, in general, valid for cw experiments. However, if the discussion is restricted to delay times τ much smaller than the pulse repetition period, it should also hold for pulsed excitation experiments. As has been shown in reference [Aßm10] for a similar QD-micropillar system, the degree of second-order coherence is relatively constant throughout the dominant part of an emission

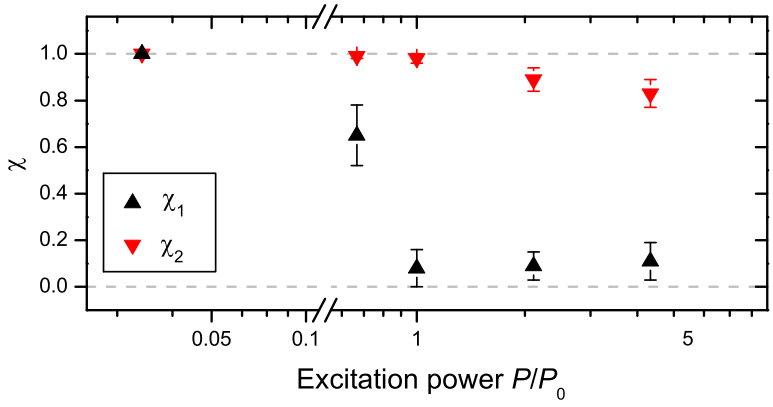

Figure 4-13: Excitation power dependence of the cavity feedback factors χ_1 and χ_2, respectively. The values for $\chi_{1,2}$ were obtained from the fits using equation (4.11).

pulse. Accordingly, as $g_N^{(2)}(\tau)$ is an intensity-weighted average over all times t within a pulse, deviations at the beginning and at the end of a pulse should be of no major consequence. Furthermore, considering the cw excitation scheme in the $g^{(1)}(\tau)$ experiments, one has to account for the photon lifetime which decreases from $\sim$250 ps at P_0 to $\sim$150 ps at $4P_0$ and thereby limits the effective coherence time of the QD-cavity system.[6]

Hence, following equation (4.11) it is possible to compare the measured $g^{(1)}(\tau)$ data, i.e. the coherence time τ_c, with results obtained from direct photon statistics measurements. Experimentally determined $g_N^{(2)}(\tau)$ curves are shown in figure 4-12, panels (a)-(c). To realise the calculations discussed above, fixed values for the number of QDs N were chosen. Subsequently, the curves were fitted to the experimental data by variation of the parameters χ_1, χ_2, and t_d.

As illustrated in figure 4-12, the simulated curves show a reasonable agreement with the experimental data. The different parameters were determined with a rather good accuracy, as revealed in figure 4-13 which shows the evolution of χ_1 and χ_2 with excitation power. The reason for the preciseness of the parameters is that they represent different characteristics of the $g_N^{(2)}(\tau)$ curves. First, χ_1 accounts mainly for the bunching behaviour which occurs at early delay times τ. Here, the other parameters are only of minor importance. The simulations reveal χ_1 to decrease from $\chi_1 \approx 1$ in the thermal regime down to roughly 0.1 in the lasing transition region at and above P_0. Second, χ_2 describes solely the magnitude of the anti-bunching term in equation (4.11) and is found to decrease from unity below threshold to a value of $\chi_2 \approx 0.83$ at $4P_0$. This moderate decrease comes from the fact that anti-bunching is also observed in the lasing regime. Finally, t_d exclusively characterises the relaxation from quantum to non-quantum light. In the threshold region, t_d is found to be $t_d \approx 6$ ps at P_0 and $t_d \approx 3$ ps at $4P_0$. A central result of the fitting procedure is that the data is best fit by the model when a number of emitters in the range of $5 \leq N \leq 8$ is assumed, which is in excellent agreement with the values assumed in the theoretical modelling framework applied in reference [Wie09]. Although this

[6] With the photon lifetime τ_0, the effective coherence time of the system is $\tau_{c,\mathrm{eff}}^{-1} = (2\tau_0)^{-1} + \tau_c^{-1}$.

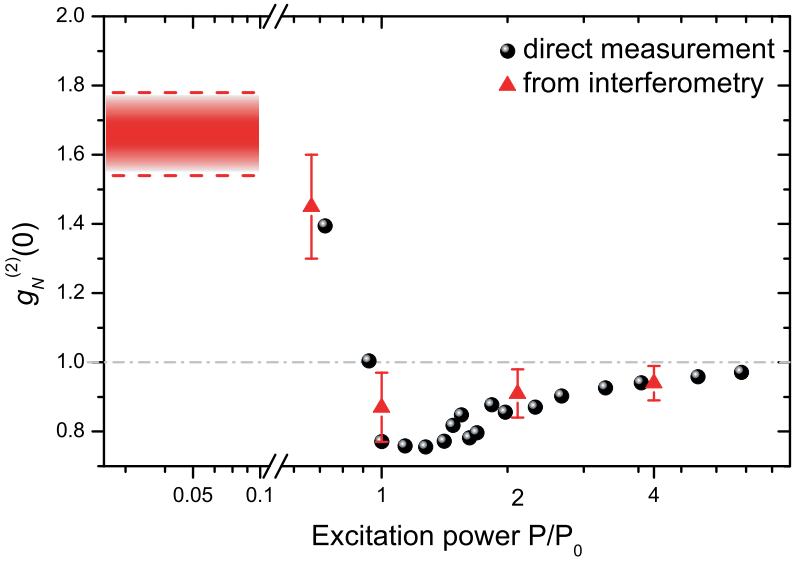

Figure 4-14: Excitation power dependence of the equal-time second-order correlation function $g^{(2)}(0)$. Data obtained with the streak camera are shown as spheres; data obtained from the fits shown in figure 4-12 are represented by triangles. In the thermal regime ($P < 0.1P_0$), a value range of $g^{(2)}(0) = 1.66 \pm 0.12$ is determined; see main text.

means that only 2–3% of the estimated total number of QDs in the active layer are contributing to the lasing operation, these results highlight the fact that the high-Q micropillar under investigation is indeed a few-emitter cavity system as manifested in the anti-bunching signal.

Furthermore, as shown in figure 4-12(d), it is possible to simulate second-order correlation values at low excitation powers (here $0.03P_0$) when reliable $g^{(2)}(\tau)$ measurements are made difficult by the limited sensitivity of the streak camera in the near-infrared spectral range. In this case, the QD laser is operated far below its threshold, and thus spontaneous emission events are predominant. Therefore, the scaling parameters were set to the expected values $\chi_1(P \ll P_0) = \chi_2(P \ll P_0) = 1$. Also, a value of $t_\mathrm{d} = 250\,\mathrm{ps}$ was used [San02], corresponding to a Purcell factor of about 2, which is in agreement with auxiliary time-resolved photoluminescence data. It is interesting to note that in the case of a two-emitter system, quantum light statistics are observed at finite delay times while $g_N^{(2)}(\tau)$ equals unity for zero delay time. For larger values of N, a bunching peak around $\tau = 0$ is accompanied by a decrease of $g_N^{(2)}(\tau)$ slightly below unity at larger delay times. However, it can be seen that in the case of $N = 20$ the results are already converging to the classical value, namely a notable bunching peak within the coherence time and uncorrelated photons at large delay times.

Considering the calculation results for $5 \leq N \leq 8$, the model can also be used to derive values for the equal-time correlation $g^{(2)}(0)$ as depicted in figure 4-14. The comparison of direct and indirect $g_N^{(2)}(\tau)$ measurements reveals a good agreement for excitation powers $P \geq 0.7P_0$. Furthermore, it is possible to provide a reasonable estimate for the state of the QD laser far below the threshold, which differs signifi-

cantly from the case of a macroscopic thermal emitter: in the regime of spontaneous emission (say $P < 0.1P_0$), the equal-time correlations amount to a value of only $g^{(2)}(0) = 1.66 \pm 0.12$. This clear deviation from the classical result is indeed expected for a system with a low number of emitters [Wie09].

While the results achieved with the presented model can describe the experimental data measured with the streak camera up to certain level, the model has clear limitations. Especially when compared to the theoretical framework modelling quantum-dot-based microcavity lasers introduced in reference [Gie07] and further developed in references [Aßm10, Ate08, Ulr07], several phenomena cannot explicitly be accounted for. This includes semiconductor-specific effects like the modified source term of spontaneous emission, Pauli-blocking, the absence of complete carrier inversion as well as many-body Coulomb effects. Another important point which is not included in the presented model are the oscillations observed in $g_N^{(2)}(\tau)$ (see figure 4-12). According to the mentioned microscopic theoretical framework, these oscillations can be traced back to the dynamical coupling between photons and carriers. In general terms of laser physics, these oscillations can be compared to relaxation oscillations as well as to Rabi oscillations. For the purpose of completeness, it should also be mentioned that the introduced model does not account for any cavity feeding effects by QDs that are not (quasi-)resonant with the cavity FM [Lau10, Win09]. It is however reasonable to neglect these at this stage, especially in the case of phonon-assisted feeding which occurs on a much slower time scale as compared to the present experimental configuration [Hoh09].

Nevertheless, despite these shortcomings, the results obtained with the presented model do agree quite well on a qualitative level with the above mentioned microscopic theory. Much larger deviations from the theoretical work by Gies et al. are assumed to occur when cavities with even larger β-factors in the range of $\beta \geq 0.1$ are investigated. It should also be stressed that the presented model is intended as a readily accessible tool to describe the coherence properties of a QD laser on a basic level allowing for easy comparison with experimental data—as an alternative to complex theoretical modelling requiring extensive numerical calculations.

4.6 Conclusions

To summarise this chapter, the lasing thresholds of QD micropillar lasers exhibiting both high Q-factors and β-factors were investigated. As expected, the lasing transition of the fundamental cavity mode was difficult to identify solely from the i/o-curve data. Consequently, the first-order correlations as well as the degree of linear polarisation were evaluated with different experimental methods. The lasing threshold was found to be accompanied by a strong nonlinear increase in the coherence time τ_c. Record values for the coherence times of more than 20 ns were determined. Simultaneously, the degree of linear polarisation ρ_L increased significantly. However, stable linear polarisation with $\rho_\mathrm{L} > 0.99$ was not reached until higher excitation were applied, i.e. $P = 6.5P_0$. Finally, a theoretical model was introduced that allows to

describe the coherence of the radiation from micropillar lasers in terms of both first- and second-order correlations.

Parts of the work presented in this chapter were published in *J. Opt. Soc. Am. B* **28**, 1404-1408 (2011); see item P3 in the publication list (page 123).

Chapter 5

Thresholds of a Polariton Laser

Quantum theory predicts that exciton-polaritons in a microcavity should behave as bosonic particles in the low-density limit. Because of this, they are expected to undergo Bose-Einstein condensation (BEC) under specific conditions. As it has been pointed out by Imamoğlu et al. [Ima96], the realisation of a macroscopic, coherent polariton BEC should lead to coherent, laser-like emission without the need of electronic population inversion.[1] This type of coherent emission of radiation is generally called polariton lasing. While a proof-of-principle experiment on polariton condensation in a GaAs-based microcavity has been presented in reference [Wer09], the aim of the current chapter is to show that polariton lasing can be distinguished from photon lasing by the observation of a two-threshold behaviour in the emission from a GaAs-based microcavity.

This chapter is organised as follows. First, in section 5.1, the fundamental physics of a BEC of microcavity exciton-polaritons are discussed. Second, the design of the investigated microcavity sample and its basic characteristics are described in section 5.2. Results of the experimental studies are presented in the subsequent parts: The two-threshold behaviour of a pulsed polariton laser at low temperatures ($T = 10\,\mathrm{K}$) is demonstrated in section 5.3. Furthermore, its temperature-dependent behaviour is analysed in section 5.4. Finally, a summary is given in section 5.5.

5.1 Microcavity-Polariton Lasers

Bosonic particles have the property to condense in unlimited numbers in their ground state. The basic physics of this so-called Bose-Einstein condensation are described in this section, following references [Den10, Kav07].

Consider a system of size r_{BE} and dimensionality d which consists of N non-

[1] As mentioned in chapter 4, the lasing condition in semiconductor lasers is defined by the Bernard-Duraffourg criterion which describes it in terms of quasi-Fermi levels of the states (i.e. bands) involved in the actual lasing transition [Ber61]. However, note that it is generally accepted to use the term *population inversion* as a synonym for the Bernard-Duraffourg criterion.

interacting bosonic particles with an energy dispersion $E(\vec{k})$. In such a system, the energy distribution of the particles is highly dependent on the temperature T and follows the Bose-Einstein distribution function:

$$f_{\mathrm{BE}}(\vec{k},T,\mu) = \left(\exp\left\{\frac{E(\vec{k})-\mu}{k_{\mathrm{B}}T}\right\}-1\right)^{-1} . \tag{5.1}$$

Here, μ gives the chemical potential, which is negative if the ground state is $E(0)=0$. Consequently, $-\mu$ is the energy needed to add another bosonic particle to the system. Its value is determined by the following normalisation condition:

$$N(T,\mu) = \left(\exp\left\{-\frac{\mu}{k_{\mathrm{B}}T}\right\}-1\right)^{-1} + \sum_{\vec{k},\vec{k}\neq 0} f_{\mathrm{BE}}(\vec{k},T,\mu) . \tag{5.2}$$

In this equation, as it is the state of interest, the ground state with $k=0$ has been separated from other states.

The particle density $n(T,\mu)$ can be determined in the thermodynamic limit, by transforming the sum into an integral. The total boson density then reads

$$n(T,\mu) = \lim_{r_{\mathrm{BE}}\to\infty}\frac{N(T,\mu)}{(r_{\mathrm{BE}})^d} = n_0(T,\mu) + \frac{1}{(2\pi)^d}\int_0^\infty f_{\mathrm{BE}}(\vec{k},T,\mu)\ \mathrm{d}\vec{k} , \tag{5.3}$$

where

$$n_0(T,\mu) = \lim_{r_{\mathrm{BE}}\to\infty}\frac{1}{(r_{\mathrm{BE}})^d}\cdot\left(\exp\left\{-\frac{\mu}{k_{\mathrm{B}}T}\right\}-1\right)^{-1} \tag{5.4}$$

represents the particle density of the ground state. While $n_0(T,\mu)$ vanishes if $\mu\neq 0$, the integral in equation (5.3) increases with μ. As a result, there exists a maximum particle density n_c that can be reached following the Bose-Einstein distribution function; it is determined by:

$$n_c(T) = \lim_{\mu\to 0}\frac{1}{(2\pi)^d}\int_0^\infty f_{\mathrm{BE}}(\vec{k},T)\ \mathrm{d}\vec{k} . \tag{5.5}$$

Assuming a parabolic dispersion and a dimensionality $d>2$, n_c is a critical density above which all additionally added particles collapse into the ground state, as proposed by Einstein [Ein24]. The ground-state particle density then reads:

$$n_0(T) = n(T) - n_c(T) . \tag{5.6}$$

This represents a phase transition characterised by a massive accumulation of bosonic particles in the ground state. Here, the chemical potential is the order parameter; it vanishes at the phase transition.

In more modern theories, condensation has been described for interacting bosons. This led to the definition that BEC is associated with the occurrence of a macroscopic wave function $\psi(\vec{r})$ with an average value of

$$\langle\psi(\vec{r})\rangle = \sqrt{n_{\mathrm{cond}}(\vec{r})}\cdot\exp\{i\phi(\vec{r})\} , \tag{5.7}$$

which simultaneously represents the order parameter of the phase transition. Above the condensation threshold, the phase is constant across the whole condensate, i.e. the condensate is completely phase-coherent. The actual value of the phase, however, is randomly chosen at the transition to BEC.

If the bosonic system is two-dimensional, such as it is the case for microcavity polaritons, equation (5.5) diverges. Strictly speaking, BEC at finite temperatures is not possible in a uniform $d = 2$ system [Hoh67, Mer66]. If, however, the particles are confined by a spatially varying potential, a BEC-like phase transition at finite temperatures becomes allowed.[2] For a two-dimensional box system of size r_{BE}, the critical particle density at a specific temperature T_c reads

$$n_c(T_c) = \frac{2}{\lambda_{\mathrm{dB}}^2} \ln\left\{ \frac{r_{\mathrm{BE}}}{\lambda_{\mathrm{dB}}} \right\} \ , \tag{5.8}$$

where λ_{dB} represents the thermal de Broglie wavelength.

Despite the reduced dimensionality, there are two main reasons why microcavity polaritons are very promising for BEC experiments. First, as discussed in chapter 2.3.2, one of the most prominent characteristics of microcavity polaritons is their light effective mass which is a direct consequence of their photonic content. This allows in principle to observe polariton condensation at significantly higher temperatures as compared, for example, with condensation of atoms [And95, Dav95]. Second, a major advantage of microcavity systems lies in the experimental accessibility, as the photons emitted from the cavity are part of the polaritonic wave function and, thus, give direct insight into several properties of the system.

In recent years, there have been several demonstrations of typical signatures of BEC in microcavities, such as macroscopic occupation of the ground state [Kas06, Wer09], spatial condensation [Bal07], strong increase of first-order spatial coherence [Den07, Ric05], quantised and half-quantised vortices [Lag08, Lag09], superfluidity [Amo09a, Amo09b], as well as the build-up of spontaneous polarisation [Bau08].

However, there is still a hot debate on how the coherent emission of a polariton condensate ("polariton lasing") can be distinguished from coherent emission of a conventional photon laser. In an early work [Den03], two different kind of thresholds have been observed on different positions of the same sample and, thus, at different cavity-exciton detuning. Later, it has been argued about the similarities of photon lasing and a polariton condensate [Baj07]. In the same publication, it has been suggested that "the observation of a second threshold at higher excitation density corresponding to photon lasing" would be "an unambiguous proof for polariton condensation or polariton lasing". Such a two-threshold behaviour has been observed by the same authors in micropillars [Baj08] as well as by another group who applied mechanical stress to a planar GaAs-based microcavity [Bal09].

In the current chapter, it will be shown that it is possible to observe two distinct thresholds in the emission of a GaAs-based microcavity while increasing the carrier

[2] In the two-dimensional case, another phase transition might occur, the so-called Berezinskii-Kosterlitz-Thouless (BKT) transition [Ber71, Kos73].

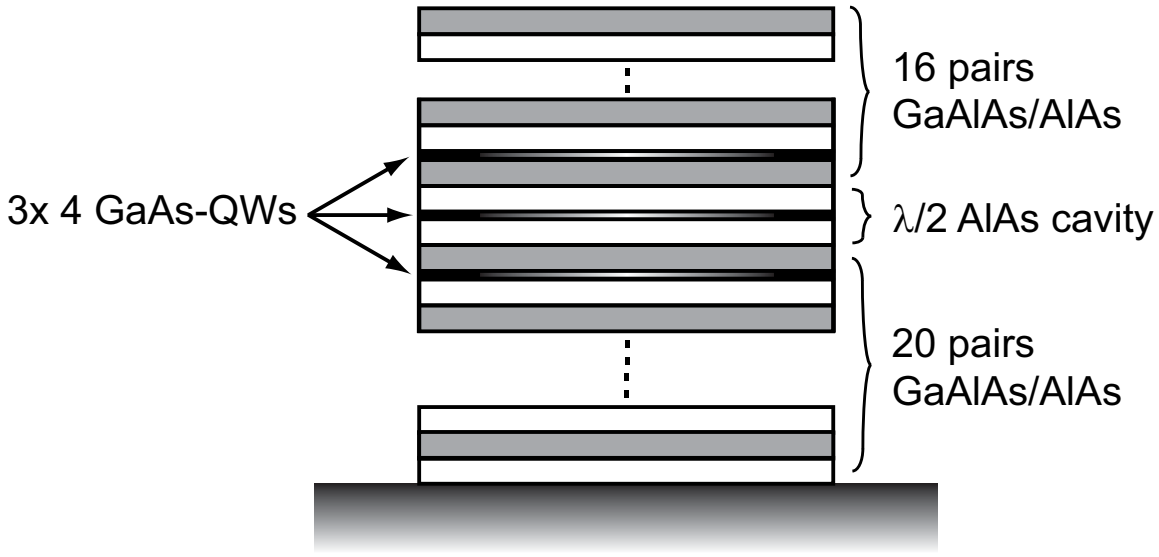

Figure 5-1: Sketch of the layer sequence of the investigated quantum-well microcavity sample. The resonator consists of a half-wavelength AlAs cavity layer sandwiched between two DBR mirrors. The DBR stacks are made of consecutive $\lambda/4$ layer pairs of $Ga_{0.8}Al_{0.2}As$ (56 nm) and AlAs (65 nm). Three stacks of four GaAs quantum wells are embedded in the microcavity.

density. Therefore, different characteristic quantities will be analysed in the spectral as well as in the time domain.

5.2 The GaAs-based Quantum-Well Microcavity Sample

The microcavity sample used for the studies presented in this chapter is based on a planar AlGaAs heterostructure.[3] It consists of a $\lambda/2$ AlAs cavity sandwiched between two distributed Bragg reflector (DBR) mirrors. The DBR stacks are composed of 16 alternating $Ga_{0.8}Al_{0.2}As$/AlAs layers on top and 20 alternating layers at the bottom of the central cavity layer. This planar microcavity structure was grown on a (001) oriented GaAs substrate by molecular beam epitaxy.

Three sets of four GaAs/AlAs quantum wells are embedded at the cavity centre as well as in the first DBR layers on either side of the cavity layer. Compared to resonators with a lower number of QWs, the use of twelve wells allows to decrease the exciton density per well for a specific polariton density. Correspondingly, the polariton density at which exciton-exciton interactions become relevant, is much higher. Simultaneously, as the Rabi splitting Ω_R scales with the square root of the QW number, the light-matter coupling is increased [Hou94b]. A sketch of the layer sequence

[3]The microcavity sample used for the studies presented in this chapter has been grown in the research group of Prof. Alfred Forchel at the Julius-Maximilians-Universität of Würzburg, Germany. The identifier of the sample is C1059.

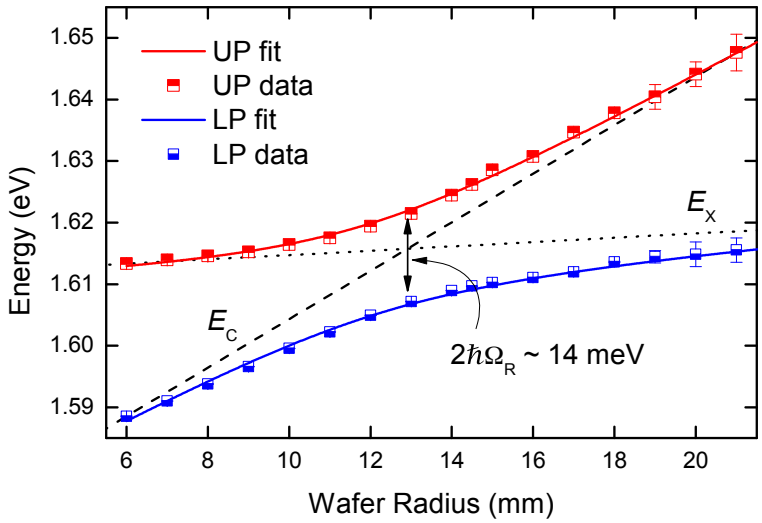

Figure 5-2: Energy of the lower (blue colour) and upper (red colour) polariton in dependence of the radial position on the sample wafer. Experimental data are obtained from reflectivity measurements. The lines represent fits to the data using equation (5.9) and assuming both the cavity mode (dashed line) and exciton resonance (dotted line) energy to change linearly with the radial position on the wafer. Compare also figure 2-6.

is shown in figure 5-1.

The cavity layer is wedge shaped, i.e. the cavity-photon energy varies across the sample. This allows for changing the cavity-exciton detuning in a certain range. However, for most experiments discussed in this chapter, the cavity-photon and exciton mode were chosen to be in resonance.

The eigenmodes of the system can be deduced from reflectivity measurements. Therefore, the reflectivity spectrum has been measured in dependence of the radial position r_{wf} on the sample wafer.[4] The experimental data are shown in figure 5-2. In order to fit the data, equation (2.29) is evaluated for zero in-plane wave vector, which results in

$$E_{\mathrm{UP,LP}}(r_{\mathrm{wf}}) = \frac{1}{2}\left[E_{\mathrm{X}}(r_{\mathrm{wf}}) + E_{\mathrm{C}}(r_{\mathrm{wf}})\right] \pm \frac{1}{2}\sqrt{\left[E_{\mathrm{X}}(r_{\mathrm{wf}}) - E_{\mathrm{C}}(r_{\mathrm{wf}})\right]^2 + 4\left[\hbar\Omega_{\mathrm{R}}\right]^2}\,, \quad (5.9)$$

where $E_{\mathrm{X}}(r_{\mathrm{wf}}) \equiv \alpha_{\mathrm{X}} \cdot r_{\mathrm{wf}} + \beta_{\mathrm{X}}$ and $E_{\mathrm{C}}(r_{\mathrm{wf}}) \equiv \alpha_{\mathrm{C}} \cdot r_{\mathrm{wf}} + \beta_{\mathrm{C}}$. Thus, the energies of the exciton resonance and the cavity mode are assumed to vary linearly with the radial position r_{wf}. From the fitting procedure, the vacuum Rabi splitting[5] is calculated to be $2\hbar\Omega_{\mathrm{R}} \sim 14\,\mathrm{meV}$. The quality factor of the microcavity is assumed to be about $1,800$.

For the measurements discussed in this chapter, the experimental techniques presented in chapters 3.2 and 3.3 were used. During all measurements the sample was

[4] Experimental data shown in figure 5-2 were obtained from reflectivity measurements which have been performed by the research group of Prof. Alfred Forchel at the Julius-Maximilians-Universität of Würzburg, Germany.

[5] Note that, in general, the determined value of the Rabi splitting depends on the applied experimental method [Sav95].

kept in a helium-flow cryostat. Optical excitation was provided by a picosecond-pulsed Ti-Sapphire laser. The pump laser was focused to a Gaussian spot approximately 30 μm in diameter on the sample at an angle of 45° from normal incidence. The emission of the sample was collected from the central area of the excitation spot using a microscope objective. To investigate the far-field emission of the sample, the Fourier plane was imaged onto the entrance slit of a monochromator and detected with a nitrogen-cooled CCD camera (see chapter 3.2). In order to perform time-resolved measurements, the emission from the sample was directed to a streak camera with a time-resolution of 2 ps (see chapter 3.3).

5.3 Two-Threshold Behaviour of a Pulsed Polariton Laser

In this section, experimental results obtained at zero cavity-exciton detuning and a sample temperature of $T = 10\,\mathrm{K}$ are presented. In order to identify the position corresponding to zero cavity-exciton detuning, the PL of the coupled system was measured in dependence of the position on the sample (not shown). From a fit of the upper and lower polariton energies using equation (5.9), the position with $\Delta_0 = 0$ was determined. In subsection 5.3.1, results obtained from Fourier-plane imaging are discussed. Subsequently, in subsection 5.3.2, results of streak-camera measurements are demonstrated. Finally, the observed characteristics of the different states of the microcavity are summarised in subsection 5.3.3.

5.3.1 Two thresholds in the spectral domain ($T = 10\,\mathrm{K}$)

The energy dispersion relation is supposed to change when microcavity polaritons condense and a polariton laser is formed. Furthermore, when the microcavity system transits into photon-lasing operation at high carrier densities, the polariton states should disappear. In order to investigate this behaviour, excitation-power dependent dispersion measurement were performed.

Figure 5-3 shows in-plane energy dispersions at different excitation powers P. At low pump powers (here 0.4 mW) only the LP branch is observed, as it is exclusively populated at low temperatures [figure 5-3(a)]. The LP branch is well fitted using equation (2.29). Upon increasing excitation power, there is evidence for a transition from the quadratic LP branch at low excitation power towards a blueshifted state. This first threshold in the microcavity emission occurs at an excitation power of $P_{\mathrm{th1}} \approx 15\,\mathrm{mW}$, as can be seen from figures 5-3(b) and 5-3(c). It is identified as the threshold to polariton lasing, as will be discussed in detail below.

Above the threshold to polariton condensation, a blueshift of the LPs at $k_{||} = 0$ as well as a change of the excitation spectrum is expected [Den10]. In the case of resonant excitation of lower polaritons with large $k_{||}$ values, the energy dispersion should

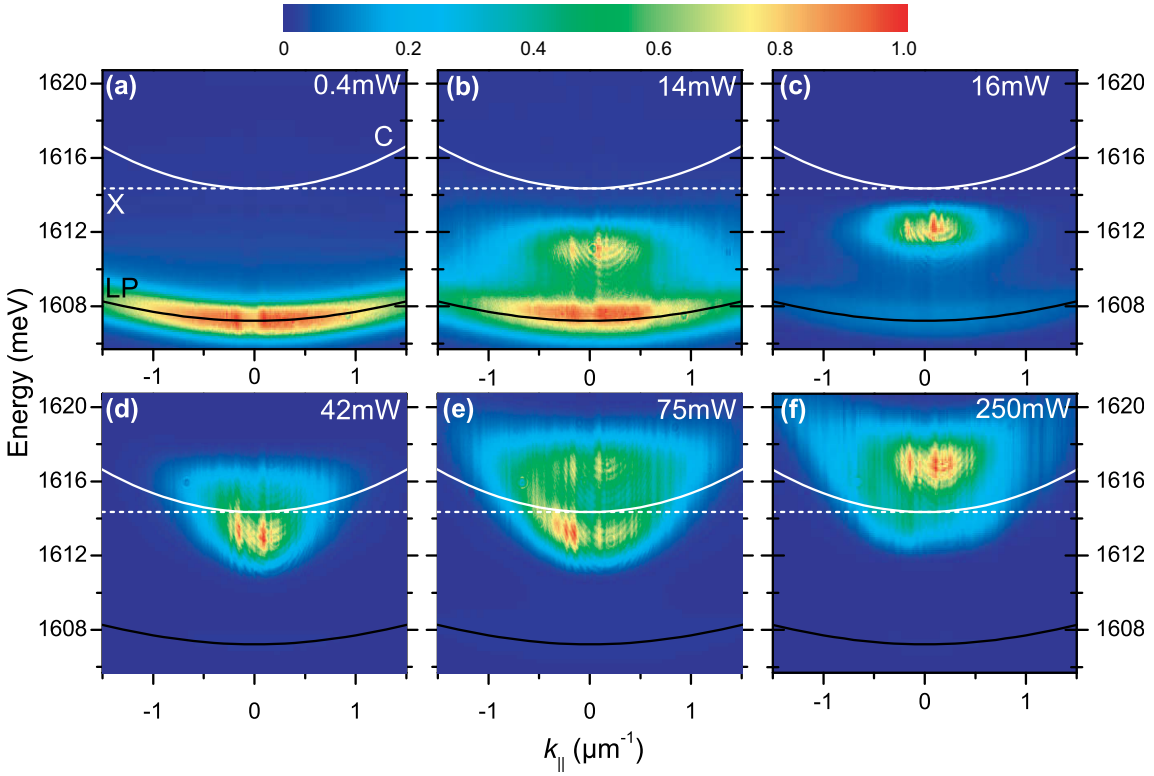

Figure 5-3: Energy-dispersion relations at different excitation powers. The black solid line gives the LP and was calculated with equation (2.29). Parameters have been chosen to fit the experimental LP data. The cavity photon dispersion (C; solid white) is obtained from equation (2.19) using the same parameters. The exciton energy (X; dotted white) is assumed to be constant in the observed $k_{||}$-range. The linear false colour scale goes from royal blue (low intensity) to red (high intensity), as indicated at the top.

exhibit a phonon-like linear behaviour for $|k_{||}\xi| < 1$ with $\xi = \hbar/(2m^*_{\mathrm{LP}} g_c n_c)^{-1/2}$. Here,[6] g_c is a coupling constant reflecting the interaction of two condensate particles and n_c is the condensate particle density. In standard equilibrium Bogoliubov theory the occurring energy dispersion above threshold is given by [Oze05]

$$\omega_{\mathrm{Bog}}(k_{||}) = \omega_{\mathrm{LP}}(k_{||}) + g_c n_c + g_c n_c \sqrt{(k_{||}\xi)^2[(k_{||}\xi)^2 + 2]} \; . \tag{5.10}$$

Here, contributions by reservoir excitons are neglected, as polaritons are injected resonantly. Dispersion curves with such a shape have first been observed on a nominally identical microcavity sample [Uts08]. Using resonant excitation, the sample described in section 5.2 was also shown to display Bogoliubov excitation spectra; see item P2 in the publication list (page 123).

However, when non-resonant excitation is applied, the contributions from the exciton reservoir cannot be neglected any more. A reasonable method to describe the dynamics of a polariton-condensate wave function $\psi_c(\vec{r})$ is to use a generalised

[6] The quantity ξ is the so-called healing length and describes "the minimal distance over which the condensate wave function can vary significantly" [Oze05].

Gross-Pitaevskii equation (GPE),[7]

$$i\hbar\frac{\partial\psi_c(\vec{r})}{\partial t} = \Big\{E_{\mathrm{LP}} - \frac{\hbar^2}{2m^*_{\mathrm{LP}}}\nabla^2_{\vec{r}} + \frac{i\hbar}{2}\big(R[n_R(\vec{r})] - \gamma_c\big) + V_{\mathrm{ext}}(\vec{r}) + \hbar g_c|\psi_c(\vec{r})|^2 + V_R(\vec{r})\Big\}\psi_c(\vec{r}) \ , \tag{5.11}$$

where $E_{\mathrm{LP}} = \hbar\omega_{\mathrm{LP}}$ is the LP energy at $k_{||} = 0$; exciton and cavity disorder are included in $V_{\mathrm{ext}}(\vec{r})$. The condensate decay and gain rate are given by γ_c and $R[n_R(\vec{r})]$, respectively, and the latter depends on the local density of reservoir polaritons n_R. This reservoir effectively generates a mean-field repulsive potential $V_R(\vec{r}) \approx \hbar g_R n_R(\vec{r}) + \hbar g_P P(\vec{r})$, which depends on the interaction strength of reservoir polaritons g_R and the pump rate $P(\vec{r})$. Furthermore, the GPE (5.11) is coupled to a rate equation for the reservoir density:

$$\dot{n}_R(\vec{r}) = P(\vec{r}) - \gamma_R n_R(\vec{r}) - R[n_R(\vec{r})]\cdot|\psi_c(\vec{r})|^2 \ . \tag{5.12}$$

In this equation, γ_R gives the decay rate of reservoir polaritons; the last term of the right side accounts for transitions of reservoir polaritons into the condensate.

The stationary solutions for the coupled equations (5.11) and (5.12) depend on both the size and the spatial shape of the excitation spot $P(\vec{r})$ [Wou08]. Assuming a spatially homogeneous excitation spot, it has been found that the reservoir density is clamped above threshold ($n_R = n_{R,\mathrm{th1}}$), while the condensate density grows as $|\psi_0|^2 = (P - P_{\mathrm{th1}})/\gamma_c$. Furthermore, in this case the condensate wave function can be described by

$$\psi_c(\vec{r}) = \psi_0 \cdot \exp\Big\{i(\vec{k}_c\vec{r} - \omega_c t)\Big\} \ . \tag{5.13}$$

In general, there exist several allowed stable solutions, as the value of the condensate wave vector $\vec{k}_c$ remains undetermined. Nevertheless, for a given $\vec{k}_c$, the eigenfrequency ω_c of the condensate is given by:

$$\omega_c - \omega_{\mathrm{LP}} = \frac{\hbar^2 k_c^2}{2m} + g_c\,|\psi_0|^2 + g_R n_R + g_P P \ . \tag{5.14}$$

However, in the case of an inhomogeneous excitation-spot profile the situation is slightly different: The stationary solutions will be of the form

$$\psi_c(\vec{r},t) \ = \ \psi_0(\vec{r})\cdot\exp\{-i\omega_c t\} \ = \ \sqrt{\rho_c(\vec{r})}\cdot\exp\{i[\phi_c(\vec{r}) - \omega_c t]\} \ , \tag{5.15}$$

$$n_R(\vec{r},t) \ = \ n_R(\vec{r}) \ , \tag{5.16}$$

where $\rho_c(\vec{r})$ and $\phi_c(\vec{r})$ denote the condensate's local density and phase, respectively. Using the equations (5.11) and (5.12) and the Ansatz given by equations (5.15) and (5.16), a solution for the condensate eigenfrequency and wave vector can be obtained by local density approximation [Wou08]. Using this approach, one has to account for the fact that the condensate eigenfrequency is constant in space. Consequently,

[7] Equations (5.11) to (5.17) are discussed in more detail in the publications by Wouters et al. [Wou07, Wou08].

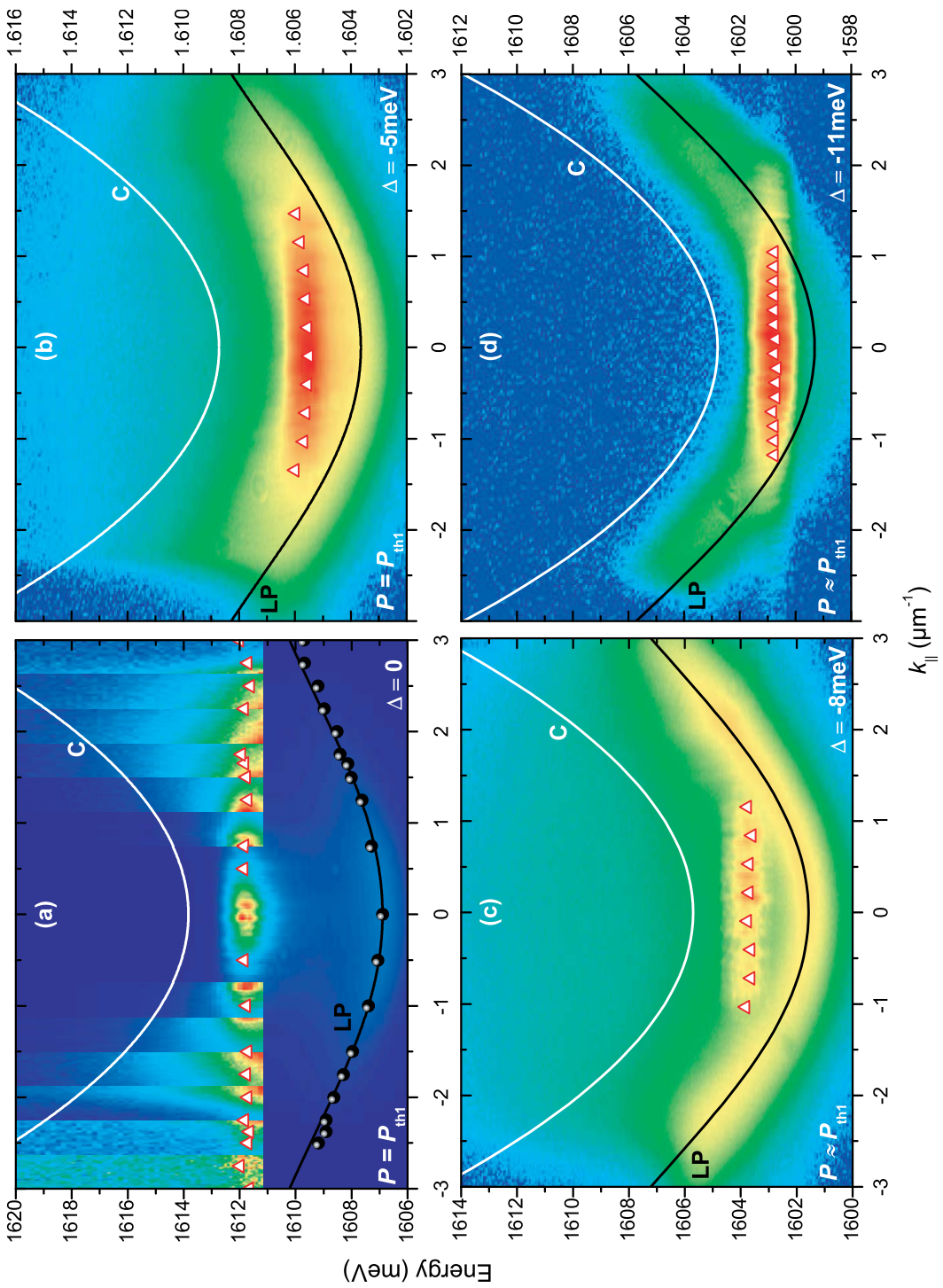

Figure 5-4: Dispersion curves at the first threshold (P_{th1}) observed at the indicated detunings Δ_0. Data measured with MO2 (NA = 0.42). The dispersion relation of the condensate is essentially flat at all detunings. At negative cavity-exciton detuning, the dispersion follows the LP dispersion at large in-plane momenta. The false colour scale is linear in panel (a) and logarithmic in panels (b) to (d). The lines give calculated LP (black) and cavity-photon (C; white) mode dispersions. Black circles (red triangles) follow the energy at the intensity maxima corresponding to the lower polariton (condensed polariton) mode. Signal at large $k_{||}$ values is magnified [panel (a)], for better visibility.

the wave vector $\vec{k}_c(\vec{r})$ has to compensate for the variation of $P(\vec{r})$, and thus varies in space across the condensate. When a circularly symmetric Gaussian laser spot is applied, as in the present experiment, the solutions of the equations discussed above should display rotational symmetry as well. Neglecting disorder induced effects, the condensate eigenfrequency has been calculated to

$$\omega_c - \omega_{\mathrm{LP}} = g_c\rho_c(r=0) + g_R n_R(r=0) + g_P P(r=0)\ . \tag{5.17}$$

The circular symmetry further implies that the local wave vector at the centre of the excitation spot equals zero, $\vec{k}_c(r=0)=0$. As the excitation-spot profile decreases in radial direction, $\vec{k}_c(\vec{r})$ is always pointed outwards and increases with $\vec{r}$.

Numerical simulations for the case of a Gaussian excitation spot with diameter of about 20 µm have shown that the dispersion of the condensate is essentially flat for small $k_{||}$-values.[8] Using the MO with larger numerical aperture, a deeper understanding of the examined microcavity state at the first threshold is obtained. As can be seen from figure 5-4(a), the shape of the condensate dispersion is flat in the observed $k_{||}$-range. The flat nature of the dispersion becomes more clear at negative detunings, as demonstrated exemplarily in figures 5-4(b) to 5-4(d) for detunings of $\Delta_0 = E_{\mathrm{C}} - E_{\mathrm{X}} = -5\,\mathrm{meV}$, $-8\,\mathrm{meV}$ and $-11\,\mathrm{meV}$, respectively. Here, it is seen that the dispersion is flat until it reaches the LP branches at high $k_{||}$-values. Accordingly, the observed shape of the dispersion agrees with the discussed theory. Moreover, the results are in line with reports from other groups, see for example reference [Mar10].

At higher excitation powers, the main emission mode occurs at further blueshifted energies. As depicted in figure 5-3(d), the emission at $P \approx 3P_{\mathrm{th1}}$ originates from an energy about 1–2 meV below the calculated cavity-photon mode. At $P = 5P_{\mathrm{th1}}$, two-mode emission is observed: While the larger part of the emission still comes from below the cavity mode, a second mode appears at roughly 3 meV above the cavity-photon mode [figure 5-3(e)]. At excitation powers well above this first threshold, the emission comes predominantly from the blueshifted cavity-photon mode [figure 5-3(f), $P = 250\,\mathrm{mW}$]. In this case, the dispersion of the emission displays a parabolic shape. Here, the SC is most probably bleached and the system remains weakly coupled. The cavity thus operates as a standard photon laser. The blueshift with respect to the calculated bare cavity mode may be attributed to changes in the material refractive indices with increasing carrier density [Moh94]; this is, however, not fully understood. Recently, another working group has discovered a similar behaviour [Chr12].

In order to analyse the dispersion curve changes in more detail, the evolution of different characteristic parameters with increasing excitation power was examined. Here, only the emission around zero in-plane momentum ($|k_{||}| \leq 0.13\,\mu\mathrm{m}^{-1}$) was taken into account.

Figure 5-5(a) shows the cavity-emission spectrum around zero in-plane momentum as a function of the excitation power. Here, the evolution of the main emission

[8] Different results are expected for smaller excitation spot sizes [Wou08]: The condensate is expected to emerge at a finite $k_{||}$-value, forming a ring-shaped object. This has been observed experimentally in a CdTe-based cavity [Ric05] as well as in a GaAs-based resonator [Chr12].

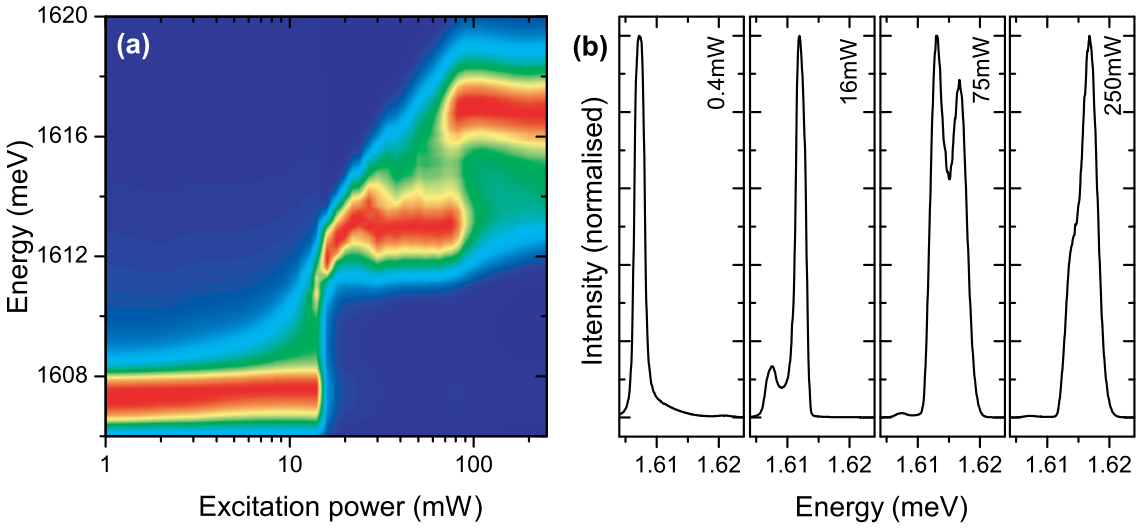

Figure 5-5: (a) Excitation-power dependence of the cavity emission spectrum in a linear colour scale going from dark blue (low intensity) to red (high intensity). (b) Emission spectrum at selected excitation powers: $P \ll P_{\mathrm{th1}}$, $P = P_{\mathrm{th1}}$, $P \approx P_{\mathrm{th2}}$ and $P \gg P_{\mathrm{th2}}$ (from left to right). In both panels, only the emission corresponding to in-plane momenta $|k_{||}| \leq 0.13\,\mu\mathrm{m}^{-1}$ was taken into account.

energy can be traced: Being rather constant in the thermal regime below P_{th1}, a clear jump of the emission energy of roughly 4 meV is found at the condensation threshold. This shows that the scheme of excitation is a relevant parameter, as the blueshift is usually smooth when cw excitation is applied. The discontinuous behaviour at the first threshold can be explained considering the combination of pulsed excitation and time-integrated dispersion imaging: The blueshift of LPs evolves with time throughout an emission pulse. Although a notable part of the emission originates from blueshifted polaritons (as evidenced by dispersion images with logarithmic colour scale; not shown), the thermal LP branch still dominates the emission for $P < 15\,\mathrm{mW}$. At P_{th1}, the emission from condensed polaritons finally prevails. As the total number of particles in the condensed state is already relatively high at this stage, a jump in energy is observed. Both, the observed discontinuous behaviour and the large blueshift are in good agreement with other results obtained for pulsed excitation (see, e.g., reference [Mar10]), whereas different results have been reported from continuous-wave experiments [Baj08, Wer09].

Above P_{th1} the emission energy first exhibits a further smooth blueshift, as expected for an interacting condensate with increasing particle density. It then stays at an almost constant value, which implies that also the average particle density in the condensed mode remains almost constant. Simultaneously, a second mode at higher energy appears and reaches comparable intensity directly below the second threshold, as shown in figure 5-5(b). Starting from $P_{\mathrm{th2}} = 80\,\mathrm{mW}$, this mode dominates the emission. Correspondingly, another jump is observed in the emission energy, before it remains fixed for higher powers. The total blueshift as compared to the low density LP energy is then roughly 10 meV, the SC is thus definitely broken. It is assumed that the cavity mainly operates as a standard photon laser above the sec-

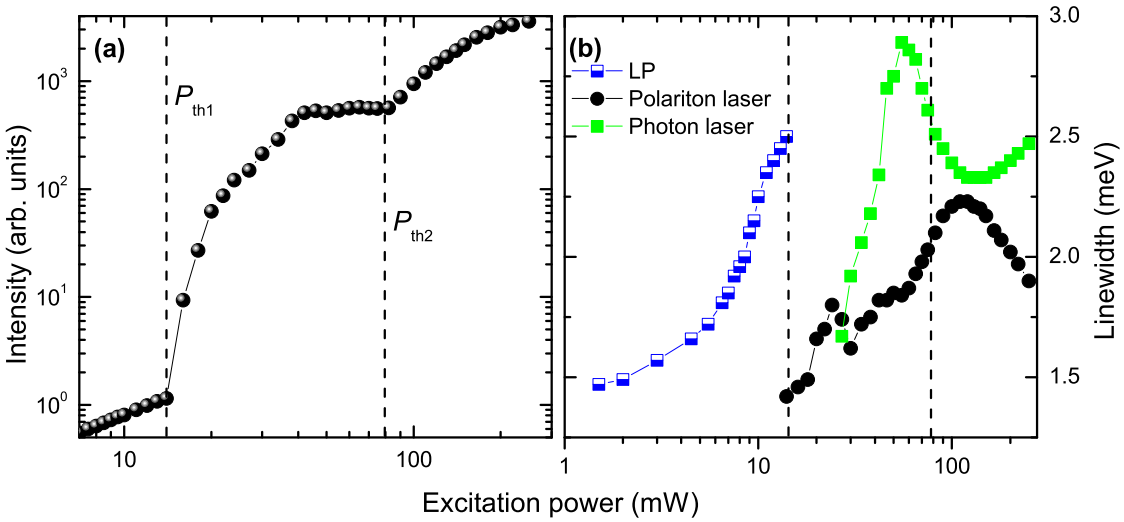

Figure 5-6: Evaluation of the cavity emission with in-plane momenta $|k_{||}| \leq 0.13\,\mu\mathrm{m}^{-1}$. Panel (a) shows the excitation-power dependence of the integrated intensity. Panel (b) displays the spectral linewidth (FWHM) of different emission modes: the LP, the polariton laser, as well as the photon laser mode. Linewidths are obtained by fitting a single- or double-peak Gaussian function to the spectra shown in figure 5-5. The vertical dashed lines indicate the two thresholds, as observed from the dispersion maps. The lines are a guide to the eye.

ond threshold. Furthermore, the transition to photon lasing is assumed to coincide with the so-called Mott density. Above the Mott density, the carriers are no longer bound to excitons, but form an electron-hole plasma. Nevertheless, due to the pulsed excitation scheme, remains of polariton lasing are still observed at high powers, as depicted in figure 5-5(b) for $P = 250\,\mathrm{mW}$. This result is in agreement with recent reports on time-resolved measurements, where the temporal transition from photon lasing to polariton lasing has been investigated [Kam12]: While photon lasing was observed at early times, emission from the polariton condensate was seen at later times in the pulsed emission. Thus, the system relaxes back to the strong coupling regime, as soon as the exciton density falls below the Mott density. For the present cavity this was also observed; see item P6 in the publication list (page 123).

A similar two-threshold behaviour is found in the development of the integrated emission intensity with excitation power, see figure 5-6(a). In the thermal regime the intensity increases linearly with pump power. With further increasing excitation power a strongly non-linear behaviour is observed, until a first saturation level is reached. At even higher pump powers a second non-linear behaviour is found. Both nonlinearities occur at the power levels where the changes in the dispersion curves as well as in the evolution of the emission energy were seen. As mentioned above, these two nonlinearities can be ascribed to the build-up of a polariton condensate at P_{th1} and the onset of standard photon lasing at P_{th2}, respectively.

While two distinct thresholds are observed in the cavity-emission energy and intensity, the situation is more difficult in the case of the spectral linewidth, as shown

in figure 5-6(b). The full width at half maximum (FWHM) was determined by fitting single- or double-peak Gaussian functions to the emission spectra.[9] The linewidth increases gradually in the thermal regime. A clear narrowing is observed at the transition to the condensate; here the linewidth is $\sim 1.4\,\mathrm{meV}$. Above P_{th1}, the linewidth further increases. In the excitation power range between the two thresholds, the appearing second mode displays a larger width than the polariton laser and further increases up to a maximum width of about 3 meV. Around the second threshold described above, the linewidth of the polariton laser strongly increases while the width of the photon laser strongly decreases. The opposite tendency is observed at very high carrier densities.

In the excitation power range between the thresholds, the monotonous increase of the polariton-laser linewidth can be explained by density fluctuations and polariton-polariton interactions [Por03], as will be discussed in more detail in section 5.3.2. The decrease of the cavity-photon linewidth around P_{th2} is a typical sign for the onset of standard lasing. Finally, the observed ongoing increase above P_{th2} may be explained by fluctuations of the refractive index throughout an emission pulse [Wan05]. In the high density regime of photon lasing, heating of the electronic system may also play a role. Nevertheless, the emission above the second threshold is identified as photon lasing by analysing the other spectral and temporal quantities.

5.3.2 Two thresholds in the time domain ($T = 10\,\mathrm{K}$)

The spectroscopic results presented in the previous subsection are clear indicators of the system changing its state at the observed thresholds. However, a detailed characterisation of the emission requires also studies of its coherence properties as well as its behaviour in the time domain. In order to assure comparability of time-resolved and spectroscopic data, the investigations in the temporal domain were restricted to the emission around $k_{||} = 0$. Furthermore, the 1 nm-wide bandpass filter[10] followed the strongest emission mode according to figure 5-5(a).

The coherence properties are determined in terms of the second-order correlation function. To this end, the streak-camera technique introduced in chapter 3.3 was applied. As the photons emitted from the cavity are part of the polaritonic wave function, the photon statistics of the emitted light is supposed to reflect the quantum statistical behaviour of the microcavity-polariton system. In particular, the second-order correlation function for equal-time events,

$$g^{(2)}(\tau = 0) = \frac{\left\langle : \hat{n}^2 : \right\rangle}{\left\langle \hat{n} \right\rangle^2} \ , \tag{5.18}$$

was measured. For a single-threshold microcavity, in which the SC is bleached before reaching the critical LP density needed for polariton condensation, a standard

[9] Note that the true linewidth is blurred due to temporal variations of the total carrier density subsequent to an excitation pulse.

[10] See chapter 3.3.1 for details.

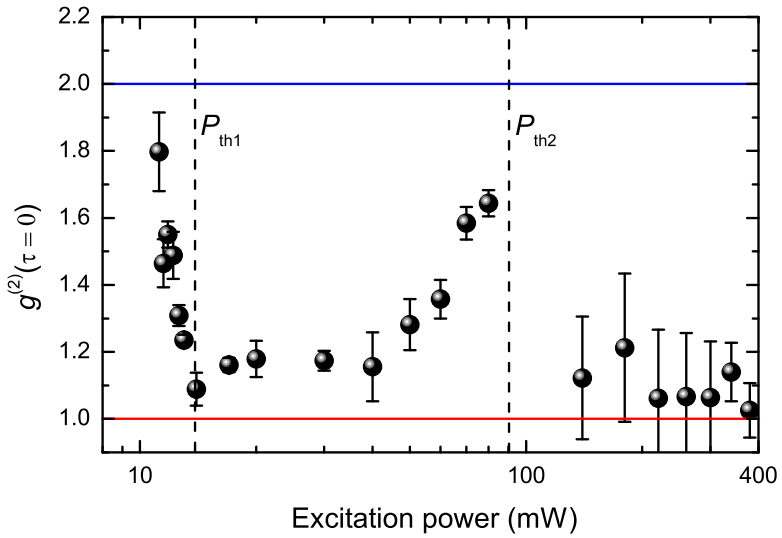

Figure 5-7: Excitation-power dependence of the equal-time correlation function $g^{(2)}(\tau = 0)$. The vertical dashed lines represent the thresholds. The blue and the red line indicate the thermal and the coherent state, respectively. Note that, for all time-resolved measurements, a 1 nm-wide bandpass filter was used to single out the main emission mode. Only the emission with zero in-plane wave vector is considered here.

laser behaviour has been observed in reference [Aßm09]: a smooth transition from $g^{(2)}(0) = 2$ to $g^{(2)}(0) = 1$. This corresponds to the transition from thermal emission below threshold to the coherent emission of a photon laser above the lasing threshold. However, the second-order correlations of a microcavity-polariton system that exhibits a two-threshold behaviour, as shown in the previous subsection, are supposed to exhibit a more sophisticated power dependence.

Investigations of the photon statistics presented up to now have been performed using HBT setups with time resolutions of many tens to a few hundred picoseconds [Den02, Kas08a, Lov08]: In an early work [Den02], strong photon bunching at the condensation threshold followed by continuously decreasing $g^{(2)}(0)$-values with increasing pumping power has been observed, but no coherent state. On the other hand, a more recent report demonstrated increasing photon fluctuations above the condensation threshold [Kas08a]. In all cases, only a single threshold has been discussed. In this section, the evolution of second-order correlations from the thermal regime to the photon-lasing regime at high excitation powers will be analysed.

Figure 5-7 shows the results of our photon-correlation measurements as a function of excitation power. At low powers the correlation function tends to a value of approximately 2. Hence, the emission has thermal light characteristics. With increasing excitation power $g^{(2)}(0)$ decreases towards unity; almost full second-order coherence is reached at $P = P_{\mathrm{th1}}$. This drop in $g^{(2)}(0)$ coincides with both the build-up of the condensate (figure 5-4) and the first non-linear increase of the integrated intensity [figure 5-6(a)]. For a rather small range of excitation powers the system stays in a regime in which the emitted light exhibits a high degree of second-order coherence, in other words $g^{(2)}(0)$ values close to unity, before photon fluctuations increase again

until $g^{(2)}(0)$ reaches a value of about 1.65.

This increase has been predicted by theorists [Sar08, Sch08]. It can be explained in terms of condensate-particle fluctuations: Based on a model consisting of a polariton reservoir in the so-called bottleneck region[11] of the LP branch and radiatively active modes around $k_{||} = 0$, the dynamics of the mode with $k_{||} = 0$ has been determined [Sch08]. A central result is that scattering processes of polaritons in the active region, i.e. between polaritons with $k_{||} = 0$ and a pair of polaritons with opposite momenta $(k_{||}, -k_{||})$, strongly increase above the condensation threshold.[12] These scattering processes result in increasing fluctuations of the condensate particle number and manifest in an unchanged average density of the condensate ground state despite of the increasing pumping. This finding is consistent with the saturation behaviour seen in the previous section in both the i/o-curve and the main emission energy: the effective condensate population remains constant in this density range.

At very high excitation powers, starting from P_{th2}, the second-order correlation function approaches $g^{(2)}(0) = 1$ again, reflecting the breakdown of SC and the transition to conventional photon lasing. It should be emphasised that the thresholds observed in figure 5-7 are in excellent agreement with the position of the thresholds observed in spectroscopic measurements in the previous section.

From the same data set used to quantify photon correlations, the temporal evolution of the cavity emission can be deduced by integrating over all recorded pulses and images (see figure 3-6). Consequently, the time-resolution stays the same (2 ps). Example temporal traces of the cavity emission are shown in panels (a) to (c) of figure 5-8. From these, the pulse duration is determined. As the temporal shape of the cavity emission can be strongly asymmetric at certain excitation powers, the pulse duration-at-half-maximum was determined in a first step. This quantity was then multiplied by $(1/2) \cdot [\ln(4)]^{-1/2}$, in order to enable direct comparison with the standard deviation of a Gaussian jitter as discussed in chapter 3.3.

Following this procedure, the results shown in figure 5-8(d) are obtained. Obviously, the two-threshold behaviour seen in the spectrally resolved data and in the second-order correlations is confirmed by the evolution of the cavity's emission-pulse duration with increasing excitation power. At low pump powers the pulses are comparatively long (25 ps and more) as the LP branch gets slowly populated through spontaneous scattering processes. The tendency shows that far longer pulse durations are expected at very low carrier densities, as is known from literature [Bil09, Den02, Den03]. With increasing power the pulses are getting shorter because of parametric scattering into the ground state, as expected for a condensed polariton state. The range where the pulse duration is as short as 5 ps is relatively small. At

[11] The bottleneck region of the LP branch is the region where the dispersion changes from exciton-like to more photon-like. As the dispersion becomes much steeper for smaller $k_{||}$-values, the density of available polariton states strongly decreases. As a result, polaritons accumulate in the region around $k_{||} \approx 10\,\mu\mathrm{m}^{-1}$. The polariton bottleneck is known to be suppressed at higher excitation densities [Sko02, Tar00]. Note that the reservoir model remains valid in that case, as the particle density at large $k_{||}$-values is implicitly accounted for; see equation (5.11).

[12] Similar theoretical results are obtained using a mean-field model [Sar08].

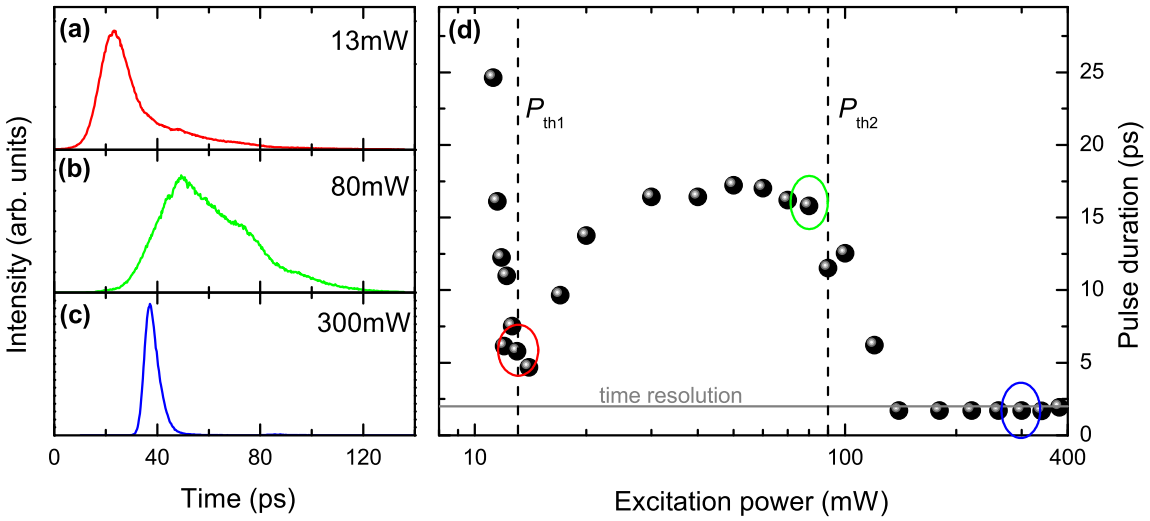

Figure 5-8: Time-resolved spectroscopy: Panels (a) to (c) show the temporal pulse profile measured at the first, at the second, and above the second threshold, respectively. Panel (d) shows the excitation-power dependence of the emission-pulse duration (Gaussian standard deviation). The data point marked by circles correspond to the pulse profiles shown in panels (a)−(c). Note that, for all time-resolved measurements, a 1 nm-wide bandpass filter has been used to single out the main emission mode. Only the emission with zero in-plane wave vector is considered here.

those excitation powers the emitted light shows almost full coherence. Starting from 20 mW polariton-polariton scattering processes set in and cause a depletion as well as subsequent repopulation of the $k_{||} = 0$ state. This results in an increasing pulse duration, which reaches a saturation level at about 17 ps. While stimulated scattering down to the condensate ground state remains active for a longer time window, the pulse duration of 17 ps is supposed to be limited by the time after which all free carriers have relaxed down to the LP branch. In this regime above the first threshold, the occupation of the ground state is supposed to stay above unity but does not increase further, considering that photon correlations concurrently increase. Furthermore, simultaneously with the second threshold in the integrated intensity and the decrease of second-order correlation to unity, the pulses are shortening again. The shortest pulse duration of 2 ps is given by the bare cavity lifetime. Thus, both thresholds are accompanied by distinct changes in the temporal pulse duration.

5.3.3 The two-threshold criterion

To summarise this section, the two-threshold behaviour in the emission of a planar GaAs-based microcavity under non-resonant pulsed excitation was demonstrated and analysed in detail. The comparison of five different quantities revealed a good overall accordance. Consequently, a comprehensive characterisation of the three different states of the cavity can be given:

(1) At low excitation powers the microcavity polariton system is in a thermal

regime of polariton photoluminescence. Here, the emission intensity from the LP increases linearly with excitation power. Also, the thermal state is underlined by strong photon fluctuations [$g^{(2)}(0) \to 2$] and long emission pulses.

(2) The first threshold at P_{th1} is identified as polariton condensation, despite of the large blueshift of the emission. Simultaneously with the first nonlinearity in the input-output curve, the build-up of the condensate in momentum space is observed. Its dispersion is essentially flat over the whole mapped $k_{||}$-range. The emission from the condensed state is further characterised by spectral linewidth narrowing, almost full second-order coherence [$g^{(2)}(0) \sim 1.1$], and short emission-pulse durations of roughly 5 ps. Moreover, it should be stressed that the condensation threshold differs significantly from a standard lasing threshold when increasing P across the threshold: First, the energy shifts continuously into the blue for $P_{\mathrm{th1}} < P < 24\,\mathrm{mW}$, as the number of particles in the condensed state is increasing. Second, polariton-polariton scattering processes cause particle fluctuations which lead to an increase of second-order correlations up to values of $g^{(2)}(0) \sim 1.6$. Third, the emission-pulse duration increases again to significantly higher values ($\sim 15\,\mathrm{ps}$) than at P_{th1}. Finally, a saturation in the emission intensity is observed, which is consistent with a constant emission energy for $P > 24\,\mathrm{mW}$.

(3) The second threshold at high excitation power (P_{th2}) goes along with the breakdown of SC and the onset of conventional photon lasing. This is reflected in a second nonlinearity in the integrated intensity as well as by another significant change in the emission energy. At this point the dispersion curve displays a parabolic shape, characteristic for cavity-mode emission. The regime of photon lasing is also accompanied by well-known characteristics in the time domain, such as a high degree of second-order coherence as well as extremely short pulse durations, reflecting the cavity-photon lifetime and the cavity Q-factor.

Thus, it was shown that the combination of well-resolved photon statistics with an in-depth spectral and temporal analysis does give an in-depth characterisation of the quantum state of a microcavity exciton-polariton system. Using the above listed characteristics, a distinction between the states of polariton lasing and photon lasing is achieved.

The presented two-threshold behaviour is reproducible in the cavity-exciton detuning range of roughly $-3\,\mathrm{meV} < \Delta_0 < +3\,\mathrm{meV}$. For more negative detunings, the energy as well as the dispersion relation of the condensed mode can still be distinguished from the cavity-photon mode, as evidenced in figure 5-4. However, the transition from polariton lasing at medium carrier densities to photon lasing at high excitation powers is much smoother in that case as well as in the case of positive cavity-exciton detunings of $\Delta_0 > 3\,\mathrm{meV}$.

5.4 Temperature Dependence of a Pulsed Polariton Laser

In the last section, a two-threshold behaviour in the emission from a GaAs-based microcavity was demonstrated. With respect to potential applications, it is particularly necessary to determine the temperature range in which a polariton laser can operate. The light mass of the lower polariton allows in principle for condensation and accordingly inversionless lasing operation at room temperature. However, it has already been shown that material parameters place an upper limit on the possible range of temperatures over which gain in terms of bosonic final state stimulation can be achieved [Sab01]. First of all, the regime of SC has to be preserved at high carrier densities, where the exciton oscillator strength may bleach [Hou95]. In this regard, the probably most important parameter is the quantum-well exciton binding energy $E_{\mathrm{b},1s}^{\mathrm{QW}}$.[13] Once the thermal energy $k_{\mathrm{B}}T$ becomes comparable to $E_{\mathrm{b},1s}^{\mathrm{QW}}$, the dissociation of excitons into free carriers is expected to set in. However, the linear optical response of the dissociated system is not significantly altered in this regime: The SC in GaAs-based microcavity systems persists even at thermal energies far beyond $E_{\mathrm{b},1s}^{\mathrm{QW}}$ and even up to room temperature, as Tsintzos et al. evidenced by electroluminescence measurements [Tsi08, Tsi09]. At those high temperatures, SC has been maintained as the Rabi splitting was still larger than the difference of the particular linewidths of the exciton and the cavity mode.

In such GaAs-based systems typical values of the exciton binding energy are on the order of $E_{\mathrm{b},1s}^{\mathrm{QW}} \sim 10\,\mathrm{meV}$, which correspond to an exciton dissociation temperature of roughly 100 K. However, exciton dissociation also means that the predominant carrier species turns from composite bosons to fermions. Accordingly, degenerate population of the ground state and bosonic final-state stimulation are suppressed, condensation becomes difficult to achieve and the emission of a macroscopic number of coherent photons is only possible by driving the system into the weak coupling regime and inverting it, thus turning it into a vertical-cavity surface-emitting lasers (VCSEL).

In the current section, the transition from SC to weak coupling and the mechanisms suppressing polariton lasing at elevated temperatures are investigated. Therefore, a temperature dependent study of the emission from the microcavity introduced in section 5.2 is presented. The experimental conditions were essentially the same as in the previous section, except for the excitation spot size which was reduced to 25 µm to allow for higher carrier densities. As in the previous section, a discussion of results from Fourier-plane spectroscopy (subsection 5.4.1) is followed by an analysis of streak-camera measurements (subsection 5.4.2). A possible explanation of the factors suppressing polariton lasing at higher temperatures is given in subsection 5.4.3.

As both the cavity-photon and the exciton energies vary with temperature, the position on the wedge-shaped sample yielding zero detuning is determined experimentally for each temperature. To this end, the position of the UP and LP energies

[13] See equation (2.8).

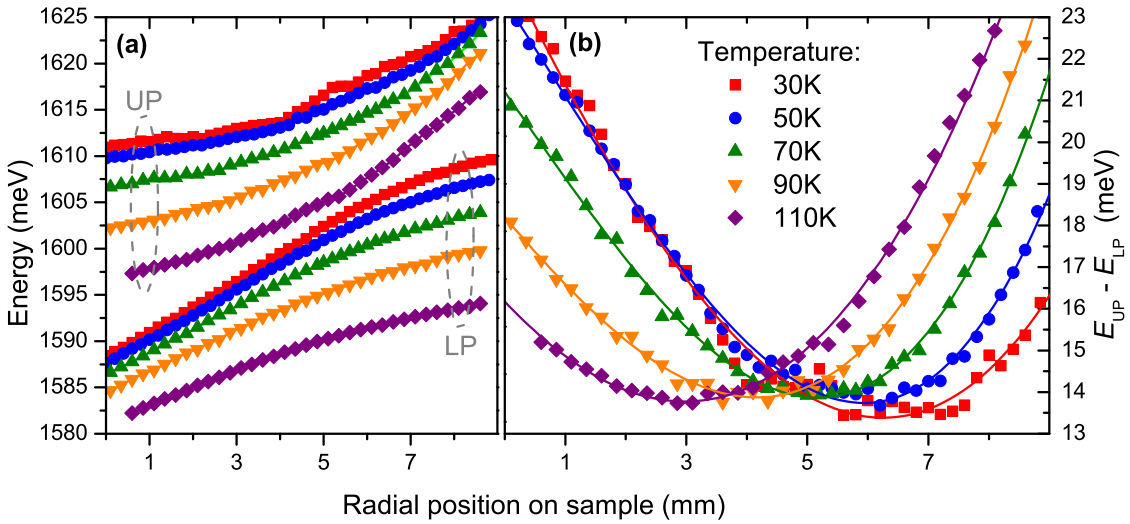

Figure 5-9: (a) Energy of the upper and lower polariton ($k_{||} = 0$) versus the position on the sample, plotted for different temperatures. (b) Energy difference between UP and LP. The data have been fitted with a parabolic function, revealing the approximate sample position with zero cavity-exciton detuning. Apparently, the Rabi splitting is not significantly altered at higher temperatures. Data are extracted from energy dispersion measurements. The indicated temperature legend accounts for both panels. Note that the scale of the abscissae is not identical to figure 5-2.

at $k_{||} = 0$ were scanned across the sample. By fitting a parabolic function to the energy difference $E_{\mathrm{UP}} - E_{\mathrm{LP}}$, the point of minimum splitting was identified. This is illustrated in figure 5-9. Strong coupling is observed up to 110 K in the used sample. Also, the Rabi splitting deduced from PL measurements does not change significantly in the examined temperature range.

5.4.1 Two thresholds in the spectral domain ($T \geq 10$ K)

Example energy-dispersion curves at various temperatures are shown in figure 5-10. The curves were measured at excitation powers slightly above the first nonlinearity observed at the indicated temperatures, as will be further discussed below. This way, the persistence of SC at lower carrier densities as well as the shape of the dispersion at the first threshold can be monitored simultaneously. As can be seen from figure 5-10(f), the LP branch can be observed at temperatures up to $T = 110$ K. Thus, the regime of SC persists over the whole temperature range in which zero detuning can be achieved on the investigated sample. This behaviour is in accordance with other reports [Hou94a, Tsi08, Tsi09]. In order to identify the polariton and photon lasing thresholds at the different temperatures, the two-threshold criterion introduced in the previous section is applied.

The Fourier-plane images shown in figure 5-10 reveal that the energy-dispersion relation observed at the first threshold is significantly different from the cavity-photon dispersion for temperatures up to 50 K. On the other hand, the emission at the first

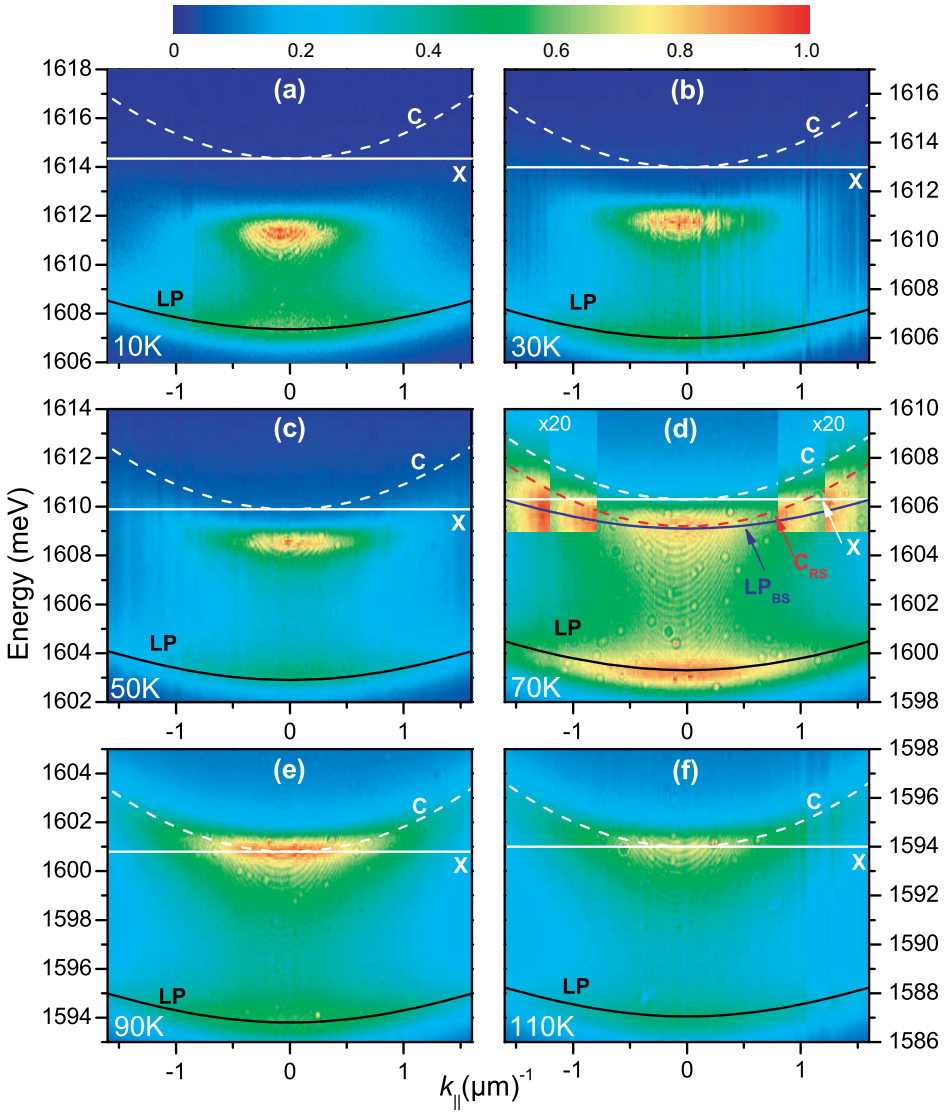

Figure 5-10: Dispersion curves at the first threshold observed at the indicated temperatures. The excitation powers were P_{th1} = (a) 3.7, (b) 5.1, (c) 8.9, (d) 17, (e) 37, and (f) 63 mW. The lines indicate the dispersion of the LP (black), bare exciton X (solid white), and bare cavity-photon mode C (dashed white). In panel (d) further curves are introduced: The solid blue line (LP_{BS}) is a blueshifted LP, while the dashed red line (C_{RS}) is obtained by shifting C into the red. All dispersion maps are normalised, as shown by the linear colour scale. In panel (d) the measured signal at large $k_{||}$ values is magnified, as indicated.

threshold measured at 90 K and 110 K seems to originate from the cavity-photon mode. The situation at 70 K is less clear. In order to obtain a deeper understanding of the data, the integrated intensity as well as the spectrum of the emission with zero in-plane momentum ($|k_{||}| \leq 0.16\,\mu m^{-1}$) were extracted from the dispersion curves. The evolution of both quantities in relation to the excitation power is shown in figures 5-11 and 5-12 for different temperatures.

In the temperature range up to $T = 50$ K, mainly three different regimes can be identified. First, starting at low excitation powers, the emission intensity increases linearly. At these polariton densities, only the thermally populated LP branch is seen, the emission energy remains almost constant. Furthermore, when increasing

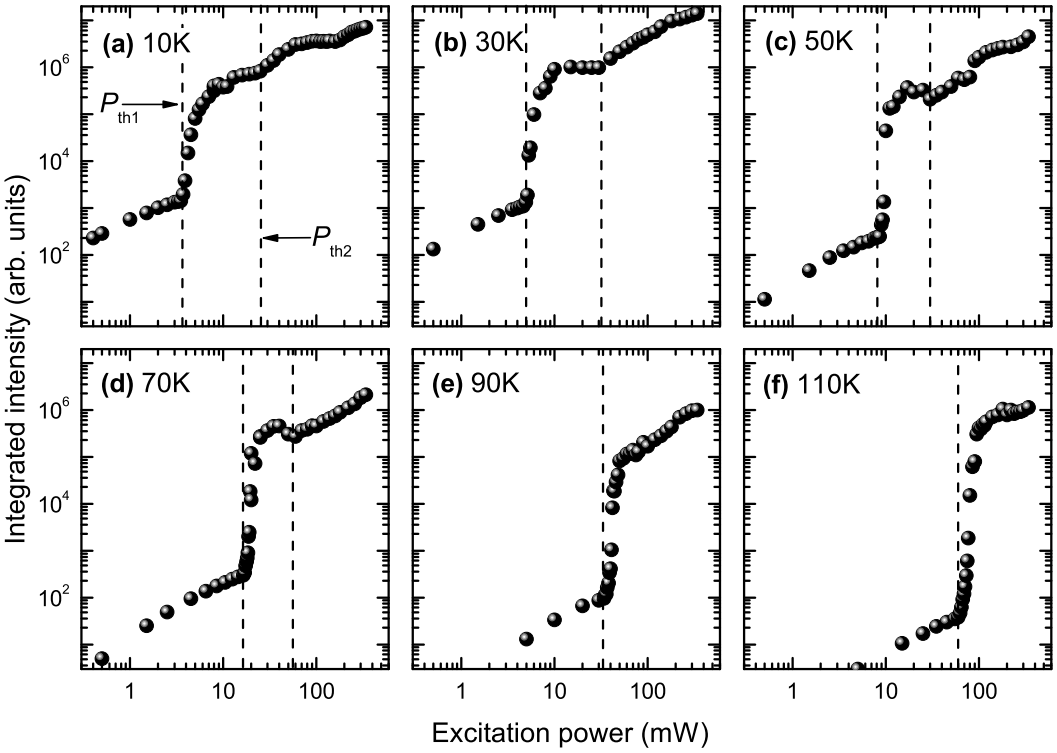

Figure 5-11: Excitation-power dependence of the emitted intensity from the strongest emission mode around zero in-plane wave vector ($|k_{||}| \leq 0.16\,\mu\mathrm{m}^{-1}$). The corresponding temperatures are indicated. The intensities are normalised by accounting for the integration time used to measure the dispersion curve at the lowest excitation power ($P = 500\,\mu\mathrm{W}$). The vertical dashed lines mark the two thresholds, P_{th1} and P_{th2}, as indicated in panel (a). At temperatures of 90 K and 110 K, only a single threshold is visible.

the power, a strongly non-linear behaviour is observed in the integrated intensity, followed by a regime of sub-linear increase. As can be seen from figure 5-12, the emission energy of the strongest mode exhibits a distinct blueshift at this first threshold P_{th1}, which is a typical signature of the spontaneous formation of a condensate of interacting particles. This is followed by a further continuous blueshift and a regime of almost constant spectral position. Note that this intermediate continuous blueshift is not that pronounced at 50 K. Furthermore, the shape of the dispersion is observed to change at this excitation power P_{th1}: The dispersion curve is mainly flat in this regime [Wou08], as discussed in the previous section. Consequently, this first non-linear change in intensity, energy and dispersion shape can be attributed to the onset of pulsed polariton lasing.

At a higher density, denoted P_{th2} in figure 5-11(a), the intensity starts to increase again at least linearly, while the energy undergoes another considerable blueshift. The emission then comes predominantly from a slightly blueshifted cavity-photon mode. At this stage, the system has changed to the weak-coupling regime and cavity-photon lasing occurs. Moreover, for larger $k_{||}$ values, the dispersion can be described by a cavity mode, blueshifted due to an altered effective index of refraction of the cavity. As mentioned above, this change in the refractive index might be caused by the high

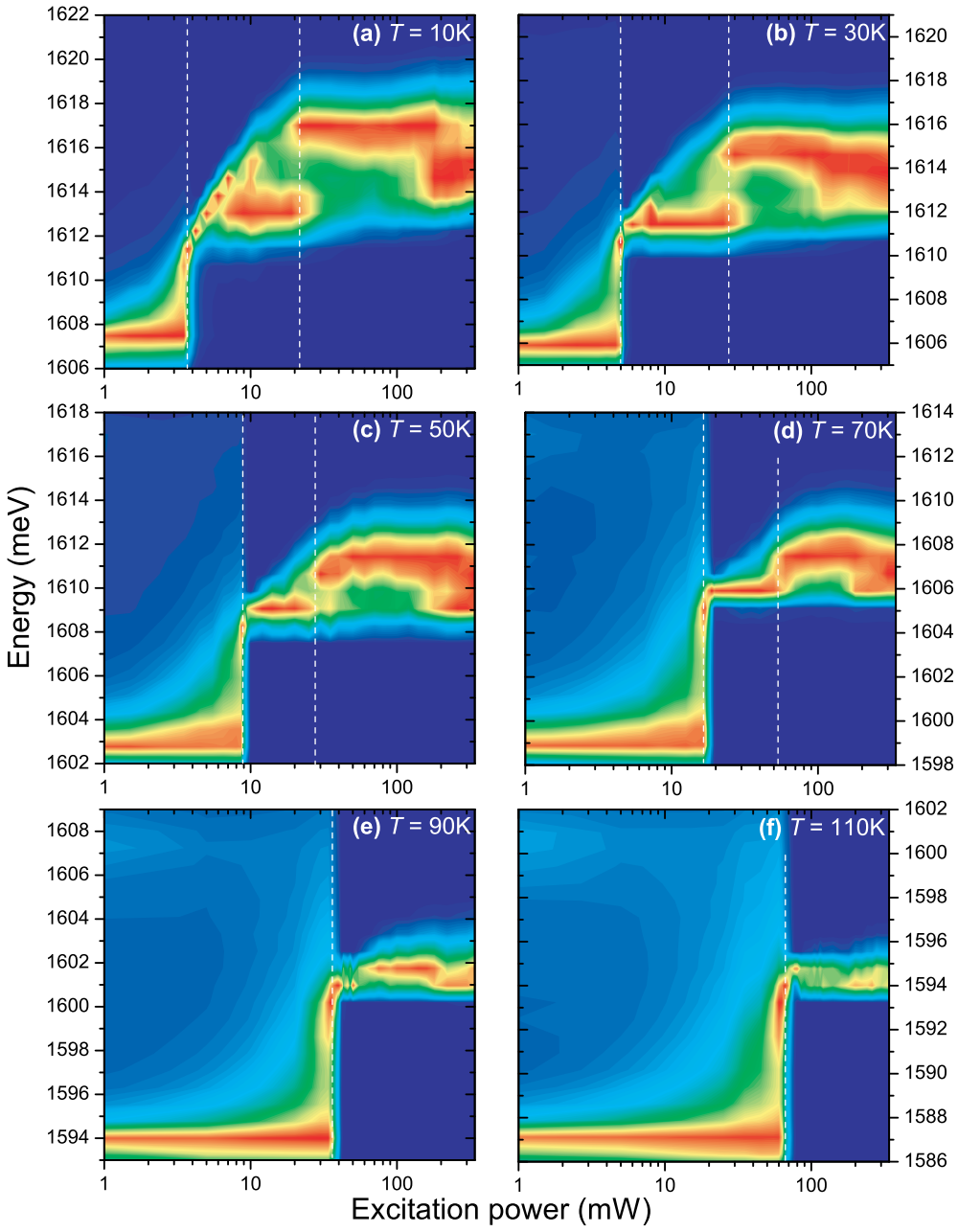

Figure 5-12: Excitation-power dependence of the emission spectrum around zero in-plane wave vector ($|k_{||}| \leq 0.16\,\mu\mathrm{m}^{-1}$). The linear colour scale goes from dark blue (low intensity) to red (high intensity). The corresponding temperatures are indicated. The vertical dashed lines mark the two thresholds P_{th1} and P_{th2}, which occur at the same excitation power as in figure 5-11. At temperatures of 90 K and 110 K, only a single threshold is visible.

charge-carrier densities [Moh94].

Interestingly, another emission mode emerges at the highest excitation powers that could be achieved. As can be seen from figure 5-12, this mode emits at an energy between the condensate mode observed at P_{th1} and the photon-laser mode seen at P_{th2}. In this high-density regime, the emission linewidth is significantly broadened and amounts to roughly 2.5 meV.[14]

While two distinct thresholds were identified at temperatures up to 50 K, the situation at an increased temperature of 70 K is less clear. The blueshift of roughly 5.5 meV that occurs at the first threshold is comparable to half the Rabi splitting, which would suggest the system having changed to the weak coupling regime. This can be seen from the dispersion curves [figure 5-10(d)]: The emission mode is rather close to the bare cavity mode. Also, the shape of the dispersion at larger $k_{||}$-values is ambiguous: It lies between a blueshifted LP mode (labelled $\mathrm{LP_{BS}}$) and a redshifted cavity-photon mode (labelled $\mathrm{C_{RS}}$). While a blueshifted LP would be a hint for the persistence of SC, a redshifted cavity mode would point to photon lasing [Baj07]. This would, however, be inconsistent with the blueshift of the cavity-photon mode that is observed at excitation powers above the second threshold for $T \leq 50\,\mathrm{K}$. Moreover, at higher excitation powers a second jump in the emission energy of $\geq 1\,\mathrm{meV}$ is apparent at $T = 70\,\mathrm{K}$. It is only at this stage that the system is definitely in the weak-coupling regime, and the emission then agrees perfectly with the cavity-photon dispersion. This interpretation is underlined by the position of the emission energies at the two thresholds as well as the corresponding blueshifts.

When going to even higher temperatures of 90 and 110 K, only a single threshold can be identified in the accessible excitation-power range. It is accompanied by a non-linear increase in the intensity as well as by a large blueshift of roughly 7 meV, which is half the Rabi splitting of the examined sample. As depicted in figures 5-10(e) and 5-10(f), the emission comes from the bare cavity photon mode. Contrary to the behaviour at lower temperatures, the emission energy seems to remain constant at very high emission powers at these high temperatures; the parabolic dispersion is unchanged at high excitation powers. Furthermore, the jump in intensity at the photon-lasing threshold is more prominent than the jumps at both thresholds for $T \leq 70\,\mathrm{K}$. This is expected and can be explained as follows. As shown in figure 5-11, the intensity of the LP below threshold decreases with temperature as non-radiative recombination processes become more relevant. However, in the regime of photon lasing, we assume that non-radiative recombination becomes negligible as radiative recombination dynamics should become faster, which results in the more pronounced jump. Note also that the reduction in photon-lasing threshold excitation power at 90K compared to the value at 70K is in good qualitative agreement with reference [Tso12].

Accordingly, two thresholds at excitation powers P_{th1} and P_{th2} were observed from angular-resolved measurements at temperatures up to 70 K. They are manifested in

[14] As mentioned in the previous section, it should be noted that the true linewidth of the microcavity emission is only accessible in low-noise continuous-wave measurements.

clear changes in the energy dispersion relation, in the integrated intensity as well as in the main emission energy.

5.4.2 Two thresholds in the time domain ($T \geq 10\,\mathrm{K}$)

In the same way as in section 5.3, the spectroscopic data discussed so far are now compared with results obtained from time-resolved measurements. Accordingly, the equal-time second-order correlation function as well as the emission-pulse duration are analysed in relation to the excitation density.

Emission-pulse durations and photon correlations at various temperatures are shown in figures 5-13 and 5-14, respectively. At temperatures up to 70 K two thresholds corresponding to the onset of polariton and photon lasing can be identified. When approaching the first threshold, the pulse duration shortens to roughly 5 ps. Subsequently, it increases again to values of approximately 17 ps (for $T = 10\,\mathrm{K}$), 15 ps (30 K), 10 ps (50 K), and 8 ps (70 K) in the polariton-lasing regime. Beyond the second threshold the emission-pulse duration reduces to the bare cavity lifetime of approximately 2 ps at all temperatures. However, in the polariton-lasing regime the increase in the pulse durations tends to become smaller with increasing temperature. This

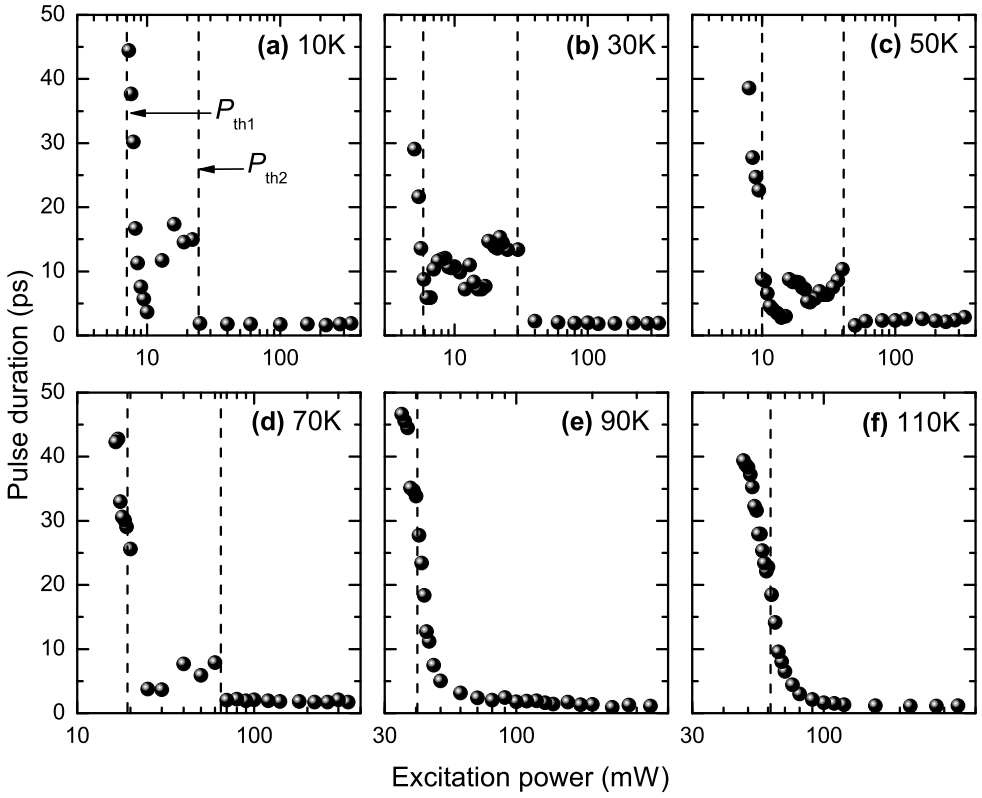

Figure 5-13: Excitation-power dependencies of the emission-pulse duration, measured at different temperatures. The vertical dashed lines represent the thresholds as in figures 5-11 and 5-12. Note that the streak-camera measurements performed in the context of this thesis are restricted to the cavity emission with zero in-plane wave vector ($|k_{||}| \leq 0.16\,\mu\mathrm{m}^{-1}$).

behaviour can be understood in terms of an acceleration of the relaxation dynamics of the non-resonantly excited carriers towards the polariton dispersion [Kas08b, Wer09]: The relaxation kinetics becomes more efficient with increasing temperature, due to the increased rate of phonon scattering.

The corresponding $g^{(2)}(0)$ shows a decrease from the thermal-regime value of two towards a value close to unity at the first threshold, reflecting thus a high degree of second-order coherence. This is followed by an increase towards values around 1.3 ($T = 10\,\mathrm{K}$), 1.65 (30 K), 1.4 (50 K), and 1.25 (70 K). This increase in $g^{(2)}(0)$ can be explained considering scattering processes between polaritons with wave vector $k_{||} = 0$ and polaritons with $k_{||} \neq 0$ [Sch08, Sch10]. These processes increase above the threshold to polariton lasing, acting thereby as a noise source for the mode around $k_{||} = 0$, as discussed in section 5.3.2. Consequently, this results in a loss of second-order coherence and thus in increasing $g^{(2)}(0)$ values at excitation powers between the two thresholds. Above the second threshold, $g^{(2)}(0)$ decreases to unity at all temperatures, indicating the Mott transition and the onset of standard cavity-photon lasing.

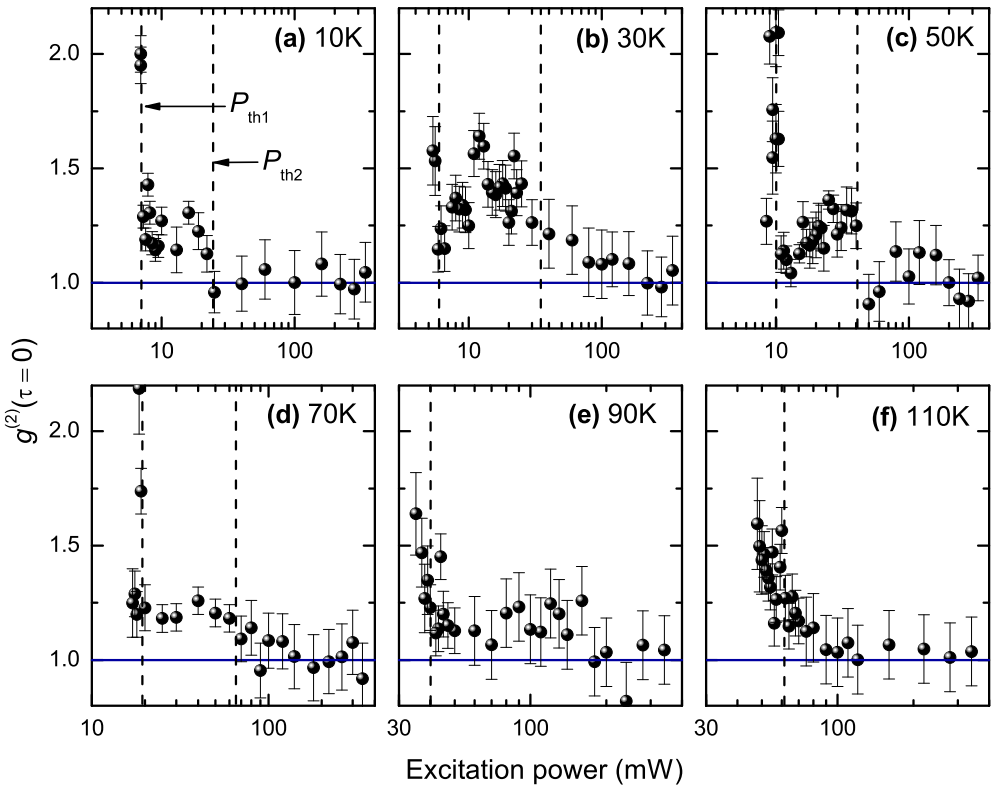

Figure 5-14: Excitation-power dependencies of the equal-time correlation function $g^{(2)}(0)$, measured at different temperatures. The horizontal line indicates the coherent state which is characterised by $g^{(2)}(0) \equiv 1$; the vertical dashed lines represent the thresholds as in figures 5-11 and 5-12. Note that the streak-camera measurements performed in the context of this thesis are restricted to the cavity emission with zero in-plane wave vector ($|k_{||}| \leq 0.16\,\mu\mathrm{m}^{-1}$).

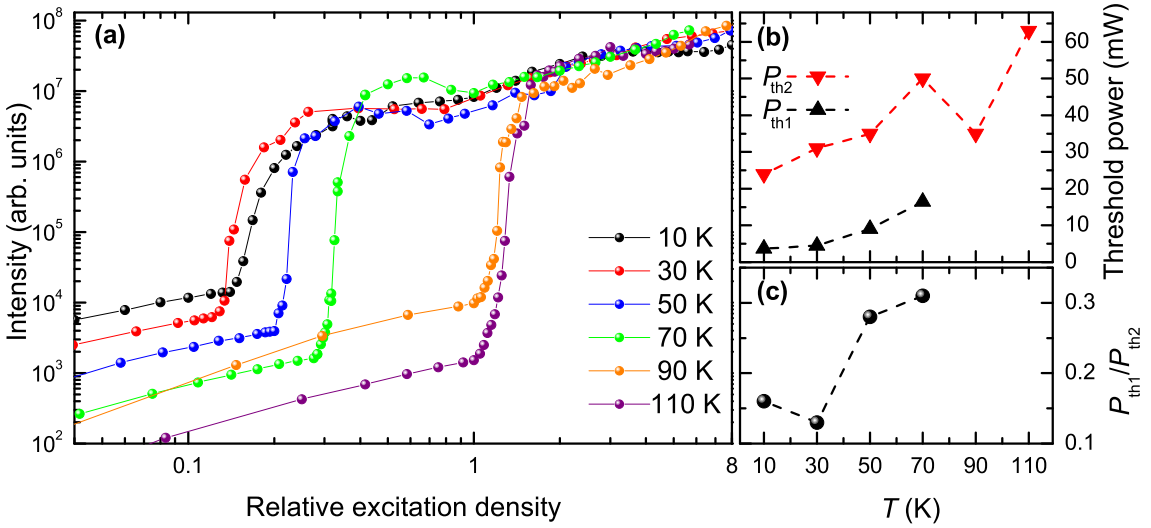

Figure 5-15: (a) Integrated intensity from the strongest emission mode versus the relative excitation density plotted for various temperatures. Relative excitation densities are given in fractions of the photon-lasing threshold P_{th2}. (b) Ratio of the threshold densities, $P_{\mathrm{th1}}/P_{\mathrm{th2}}$. The lines are guide to the eye.

Furthermore, the positions of the two thresholds are in good accordance with the positions of the nonlinearities in the i/o-curve shown in figure 5-11. Again, the results obtained at 70 K do not allow for a clear distinction between two thresholds: While the pulse duration exhibits a small increase at intermediate powers, $g^{(2)}(0)$ essentially decreases monotonically from a thermal to a coherent value.

The situation changes significantly for temperatures above 70 K, in agreement with the observations in the spectral domain. At 90 K and 110 K only a single threshold is visible in both photon correlations and the pulse duration. It occurs at a three to ten times higher threshold excitation density than the first threshold evidenced at lower temperatures, and roughly coincides with the excitation densities at the second threshold seen there. Therefore, it is a reasonable assumption to link this single threshold to the onset of standard cavity-photon lasing.

5.4.3 Processes suppressing polariton lasing at $T > 70$ K

As demonstrated in sections 5.4.1 and 5.4.2, polariton lasing is observed at temperatures up to 70 K in the examined microcavity sample. The underlying effects that are responsible for the suppression of polariton lasing at higher temperatures are discussed in this part.

At first glance, one possible reason for the non-appearance of polariton lasing at temperatures above 70 K might be an increase of the exciton linewidth with increased temperature. This change in the exciton linewidth would directly affect the Rabi splitting. However, this can be disproved by dispersion measurements at very low excitation power, from which a Rabi splitting of roughly 13.5 meV at 110 K is deduced. This is in agreement with reference [Gam95], which states that the linewidth of

quantum-well excitons does not increase significantly for temperatures below 100 K.

In the following, the relative positions of the two thresholds, $\rho_P = P_{\mathrm{th1}}/P_{\mathrm{th2}}$, are analysed. Therefore, all i/o-curves are plotted on a comparable scale in figure 5-15(a). In order to realise comparability, the excitation densities are expressed in fractions of the photon-lasing threshold P_{th2}. To this end, it is assumed that in the photon-lasing regime the dynamics become so fast that non-radiative recombination becomes negligible, as mentioned above, and the emitted intensity therefore becomes directly proportional to the inserted carrier density independent of temperature. While at 10 K the relative excitation density ratio of the first to the second threshold takes on a value of 0.16, it slightly decreases to 0.13 at 30 K [figure 5-15, panels (b) and (c)]. At even higher temperatures ρ_P increases up to a value of 0.31 at 70 K. To some degree this increase for $T > 30\,\mathrm{K}$ is expected and can be explained as follows: On one hand, the Mott transition essentially occurs either due to wave function overlap of the inserted carriers or due to an ionization catastrophe causing screening and thus further ionization when a certain number of carriers is inserted into the system [Ric78]. In both cases the transition carrier density—which is assumed to coincide with P_{th2}—is not expected to show a considerable temperature dependence[15] for the exciton binding energy of $E_{\mathrm{b},1s}^{\mathrm{QW}} \sim 10\,\mathrm{meV}$ considered here [Sno08]. Furthermore, it is known that the scattering rate from the exciton reservoir towards the bottom of the LP branch is inversely proportional to the exciton temperature, thus increasing also the excitation power necessary for polariton condensation [Por02]. Both effects may lead to an increase of ρ_P.

On the other hand, the total carrier density at the first threshold will depend strongly on the fraction of the total carriers which form exciton-polaritons and on the characteristic timescale of their relaxation to the lower-polariton ground state compared to the typical timescale of non-radiative relaxation processes which both depend on temperature. At elevated temperatures the bottleneck in polariton relaxation is expected to become suppressed due to increased polariton-polariton scattering [Tar00]. Also longitudinal optical phonon scattering is assumed to become effective at above 60 K in GaAs and is known to improve the polariton relaxation rate towards the ground state drastically [Mar10, Tas97]. As a rough qualitative estimate of the relative importance of those effects, the relative exciton fraction can be approximated using the Saha equation, which takes the following form for a non-degenerate two-dimensional system in thermal equilibrium [Phi96]:

$$\frac{N_{\mathrm{e}} N_{\mathrm{h}}}{N_{\mathrm{X}}} = K = \frac{\mu_{\mathrm{X}} k_{\mathrm{B}} T}{\pi \hbar^2} \exp\left\{-\frac{E_{\mathrm{b},1s}^{\mathrm{QW}}}{k_{\mathrm{B}} T}\right\} . \tag{5.19}$$

Here, N_{e} (N_{h}) is the electron (hole) density, and N_{X} and μ_{X} represent the exciton density and reduced mass, respectively. Obviously, this is a rough simplification as the non-degeneracy condition is fulfilled only below threshold and thermal equilibrium is not necessarily established. Nevertheless, it is sufficient to estimate the relative

[15] Significant changes of the Mott density are expected when very low temperatures way below 10 K are investigated [Sno08].

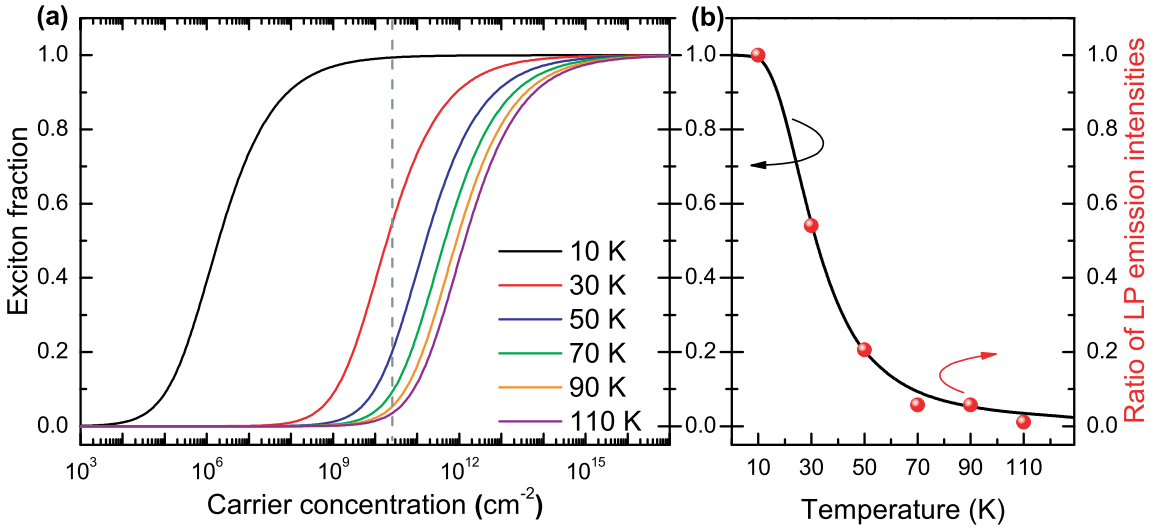

Figure 5-16: (a) Fraction of the carriers present that form excitons according to the Saha equation (5.19) versus the total carrier density in the system plotted for temperatures of $T = 10,\ 30,\ \cdots,\ 110\,\mathrm{K}$. The vertical dashed line indicates the carrier density used in panel (b). (b) Exciton fraction according to the Saha equation for a carrier density of $2.5 \times 10^{10}\,\mathrm{cm}^{-2}$, corresponding roughly to 5% of the Mott density. Red dots give the intensity ratio of the emission from the LP ground state at a given temperature T to the emission from the LP ground state at $T = 10\,\mathrm{K}$. For the intensity ratio values experimental data gathered at an excitation power of roughly 5% of P_{th2} were analysed. Note that, strictly speaking, the Saha equation is only valid below the Mott density.

importance of exciton ionization and modifications of the relaxation rate. The calculated relative exciton fractions compared to the total carrier densities at various temperatures are shown in figure 5-16(a). In the present considerations, the main interest lies on the low excitation densities way below the degeneracy threshold where the Saha equation still is a good approximation. It is assumed that the Mott threshold density per quantum well is on the order of $5 \times 10^{11}\,\mathrm{cm}^{-2}$, which is a typical value for the kind of sample considered here. Using this parameter, the exciton fractions far below threshold predicted by the Saha equation can be compared to the relative emitted LP intensities. The comparison is shown in figure 5-16(b). The ratios of the emitted intensities follow the predicted exciton fractions quite well, indicating that the exciton formation rate is the dominating effect determining the LP emission at low excitation densities. At high temperatures beyond 70 K equation (5.19) tends to slightly overestimate the ratio of the emitted intensities. This behaviour is attributed to additional small effects of temperature-dependent non-radiative recombination.

However, it is obvious that the relative position of the first threshold is not completely determined by the exciton fraction and the corresponding exciton density present in the system. The small but distinct reduction of the threshold carrier density that occurs when going from 10 K to 30 K despite the strongly reduced exciton fraction in the system indicates that relaxation towards the LP ground state becomes much more efficient at slightly increased lattice temperatures. This finding agrees with previous studies showing that a slightly increased lattice temperature

tends to lower the polariton-lasing threshold for not too positive detunings. However, the exact range of detunings where this decrease of the threshold occurs was shown to vary from sample to sample and probably also depends on the excitation conditions [Kas08b, Wer09]. Generally, previous studies have shown the polariton bottleneck to become more efficiently suppressed at around 30 K due to beneficial phonon scattering [Tar00].

5.5 Conclusions

In this chapter, the emission from a microcavity-polariton system was investigated. A prominent two-threshold behaviour was observed at $T = 10\,\mathrm{K}$ in different experimentally accessible quantities in the spectral as well as in the time domain: Two distinct transitions were identified in the energy-dispersion, the main emission energy and intensity as well as in the photon correlations and in the emission-pulse duration. Using these results, a list of criteria to distinguish three regimes of thermal emission, polariton lasing, and photon lasing was given.

In a temperature-dependent study, it was demonstrated that the two-threshold behaviour is observed at temperatures up to 70 K. At elevated temperatures of 90 K and 110 K, only a single threshold is observed, which is attributed to the transition to photon lasing.

Following the analysis of the relative position of the observed two thresholds, the suppression of polariton lasing at higher temperatures can be explained by thermal ionization of excitons which effectively reduces the available number of polaritons. However, it should be noted that the results presented in section 5.4.3 do not exclude the possibility that the breakdown of strong coupling might be explained in terms of Coulomb-correlated electron-hole plasma systems [Kir97, Szc04]. Therefore, further theoretical calculations are necessary to clarify the nature of this transition.

Parts of the results presented in this chapter were (or will be) published in items P2 and P4-P6 in the publication list (page 123).

Chapter 6

Summary and Outlook

In this thesis, the nonlinearities occurring in the emission of two different kinds of microcavity lasers, respectively working in the regimes of weak and strong coupling, were studied. The lasing thresholds were identified by means of different experimental methods.

First, the lasing thresholds of quantum-dot micropillars with different diameters were examined. In each case, the fundamental cavity mode was found to be split into two orthogonally polarised modes of comparable intensity in the thermal regime. This was attributed to a residual ellipticity in the cross-section of the pillars. From input-output curves, β-factors in the range of 0.01 to 0.07 were determined. Accordingly, the threshold-carrier density was difficult to identify solely from the i/o-curves. The emission from a micropillar with a diameter of 8 µm was analysed in more detail. Polarisation-sensitive measurements revealed that one of the fundamental mode components was dominating the emission above threshold, resulting in a high degree of linear polarisation of $\rho_L = 0.99$. Furthermore, the first-order correlation function was measured using a high-resolution Michelson interferometer. Record coherence times of roughly 20 ns for the stronger mode were derived. A simple theoretical model connecting first-order and second-order correlations was introduced. The presented model allowed for an estimate of the effective number of QDs contributing to the system's radiation. Based on a result of approximately five to eight contributing quantum dots, a value range for second-order equal-time correlations in the thermal regime was evaluated. In this way, the experimentally accessible excitation-power range for photon-correlation measurements using a streak camera was extended into the thermal emission regime.

These results allow for a comprehensive characterisation of the lasing threshold of quantum-dot micropillars. However, there are still a number of open questions. For example, it is still unclear whether the number of quantum dots contributing to the cavity emission is the sole reason for the observed non-classical light emission around the threshold region. Further studies could examine cross-correlations between different micropillar modes, e.g. between the two fundamental mode components: a laser device emitting simultaneously two or more uncorrelated modes could be beneficial

with regard to enhanced optical data transmission rates using multiplexing methods.

Second, the two-threshold behaviour of a GaAs-based quantum-well microcavity operating in the regime of strong coupling was demonstrated. Experimental results obtained from Fourier-plane spectroscopy and time-resolved measurements were combined: two distinct nonlinearities were observed in the energy-dispersion relation, the emitted intensity and energy, as well as in the emission-pulse duration. It was shown that polariton lasing and conventional photon lasing can clearly be distinguished. Additionally, the second-order correlation function was measured by means of the recently introduced streak-camera technique, which was improved in the framework of this thesis. Following this approach, the polariton laser was evidenced to feature a high degree of second-order coherence of $g^{(2)}(0) = 1.1$ just above the transition to polariton condensation. The evolution of $g^{(2)}(0)$ with excitation power also revealed a prominent two-threshold behaviour. Furthermore, in a temperature-dependent study of polariton lasing, the two thresholds mentioned above could be observed at temperatures up to 70 K. The suppression of polariton lasing at higher temperatures could be explained by thermal ionization of excitons, which effectively reduces the available number of polaritons. However, it should be noted that the presented results do not exclude the possibility that the breakdown of strong coupling might be explained in terms of Coulomb-correlated electron-hole plasma systems. Therefore, further theoretical calculations are necessary to fully clarify the nature of this transition.

In this second part, a set of criteria was presented which allows one to distinguish polariton lasing from conventional photon lasing. Unfortunately, the suitability of GaAs-based polariton lasers for potential applications is hard to estimate, as polariton lasing is suppressed for temperatures above 70 K. However, GaAs-based microcavities remain an excellent example system allowing for the exploration of the properties of polariton condensates in general. It is very likely that results obtained from GaAs-based resonators may be transferred to other material systems, such as GaN or ZnO. Those semiconductors appear to be more promising for room temperature applications due to their larger exciton binding energy.

Further scientific research on polariton condensates should investigate their phase-coherence as well as their superfluid nature. Using the available Michelson interferometer in a slightly changed configuration, the first-order spatial correlation function of polaritonic systems could be evaluated under different experimental conditions. Also, by shaping the polariton landscape using different excitation-spot geometries, the direction of flow of polaritons could be controlled. Finally, a very promising idea is to realise all-optical switches and gates with the help of imprinted potentials.

Appendix A

Second-Order Correlations of an N-Emitter System

The second-order correlation function of an ensemble of N (identical) emitters was first explicitly derived in the context of resonance fluorescence from atomic beams with atomic number fluctuations [Car78]. The total radiation from such a system can be described by a superposition of the electric fields eradiated by each single emitter:

$$E_{N(t)}(t) = \sum_{i=1}^{N(t)} E_i(t) + \epsilon \ , \tag{A.1}$$

where ϵ is a time-independent term describing any scattered light from the background, i.e. noise. The second-order correlation function of the total field can then be calculated as follows:

$$G^{(2)}_{N(t)}(\tau) = \left\langle E^-(t)E^-(t+\tau)E^+(t+\tau)E^+(t)\right\rangle \tag{A.2}$$

$$= \left\langle \sum_{i=1}^{N(t)} \sum_{j=1}^{N(t+\tau)} \sum_{m=1}^{N(t+\tau)} \sum_{n=1}^{N(t)} \left(E_i^-(t) + \epsilon^-\right)\left(E_j^-(t+\tau) + \epsilon^-\right) \right.$$

$$\left. \times \left(E_m^+(t+\tau) + \epsilon^+\right)\left(E_n^+(t) + \epsilon^+\right) \right\rangle . \tag{A.3}$$

In order to facilitate the computation of $G^{(2)}_{N(t)}(\tau)$, a few reasonable assumption can be made. It is presumed that the number of active emitters, i.e. the number of QDs resonant with the cavity FM, is time-independent, thus $N(t) = N(t+\tau) = N$. It is also assumed that fields from different emitters are not correlated in the first instance. Possible correlations due to cavity induced effects in the micropillar are introduced in section 4.5 using the phenomenological factors χ_1 and χ_2. With the two aforementioned assumptions, equation (A.3) can be rewritten as

$$G^{(2)}_N(\tau) = NG^{(2)}_A(\tau) + N(N-1)\cdot\left[I_A^2 + \left|G^{(1)}_A(\tau)\right|^2\right]$$

$$+ |\epsilon|^4 + 2I_A N|\epsilon|^2 + 2\mathrm{Re}\left(G^{(1)}_A\right)N|\epsilon|^2 \ , \tag{A.4}$$

where the intensity of the emission from a single emitter is $I_A = \langle E_i^- E_i^+ \rangle$. The first- and the second-order correlation functions of the emission from each single emitter included in equation (A.4) are defined as usual:

$$G_A^{(1)}(\tau) = \left\langle E_i^-(\tau) E_i^+(0) \right\rangle \ , \tag{A.5}$$

$$G_A^{(2)}(\tau) = \left\langle E_i^-(0) E_i^-(\tau) E_i^+(\tau) E_i^+(0) \right\rangle \ . \tag{A.6}$$

A full analytical description of both $G_A^{(1)}(\tau)$ and $G_A^{(2)}(\tau)$ can be found in reference [Car76]. As any effect induced by the cavity surrounding the QD layer is accounted for by $\chi_{1,2}$ (see section 4.5), the additional terms including noise related phenomena can be omitted, i.e. we can set $\epsilon \equiv 0$. Thus $G_N^{(2)}(\tau)$ can be rewritten as

$$G_N^{(2)}(\tau) = N G_A^{(2)}(\tau) + N(N-1) \cdot \left[I_A^2 + \left| G_A^{(1)}(\tau) \right|^2 \right] \ . \tag{A.7}$$

This equation mainly consists of three parts: the first part is proportional to $G_A^{(2)}(\tau)$ and, as each emitter contributes equally, also proportional to N. This part reflects the anti-bunching behaviour of single emitters and is thus dominant for low values of N. The second and third parts have their origins in the product of correlations from different atoms. Their contribution increases for larger ensembles of emitters. The coefficient of the second and third part results from the number of possible emitter pairs, which is $N(N-1)$.[1]

In order to obtain the normalised second-order correlation function $g_N^{(2)}(\tau)$, equation (A.7) must be divided by $|G^{(1)}(0)|^2 = (NI)^2$. Equation (4.9) is then readily obtained.

[1] A detailed discussion of the different parts in equation (A.7) can be found in reference [Hen03].

Bibliography

[Abr72] M. Abramowitz and I. A. Stegun, *Handbook of Mathematical Functions with Formulas, Graphs, and Mathematical Tables. National Bureau of Standards Applied Mathematics Series 55. Tenth Printing.*, Dover Publications, Mineola / NY (1972). 15

[Ada85] S. Adachi, GaAs, AlAs, and $Al_xGa_{1-x}As$: Material parameters for use in research and device applications, J. Appl. Phys. **58**, R1 (1985), doi:10.1063/1.336070. 5

[Amo09a] A. Amo, J. Lefrère, S. Pigeon, C. Adrados, C. Ciuti, I. Carusotto, R. Houdre, E. Giacobino, and A. Bramati, Superfluidity of Polaritons in Semiconductor Microcavities, Nat. Phys. **5**, 805 (2009), doi:10.1038/nphys1364. 71

[Amo09b] A. Amo, D. Sanvitto, F. P. Laussy, D. Ballarini, E. D. Valle, M. D. Martin, A. Lemaitre, J. Bloch, D. N. Krizhanovskii, M. S. Skolnick, C. Tejedor, and L. V. na, Collective Fluid Dynamics of a Polariton Condensate in a Semiconductor Microcavity, Nature **457**, 291 (2009), doi:10.1038/nature07640. 71

[And95] M. H. Anderson, J. R. Ensher, M. R. Matthews, C. E. Wieman, and E. A. Cornell, Observation of Bose-Einstein Condensation in a Dilute Atomic Vapor, Science **269**, 198 (1995), doi:10.1126/science.269.5221.198. 71

[Ash76] N. W. Ashcroft and N. D. Mermin, *Solid State Physics*, Thomson Learning, U.S. (1976). 6

[Aßm09] M. Aßmann, F. Veit, M. Bayer, M. van der Poel, and J. M. Hvam, Higher-Order Photon Bunching in a Semiconductor Microcavity, Science **325**, 297 (2009), doi:10.1126/science.1174488. 37, 82

[Aßm10] M. Aßmann, F. Veit, M. Bayer, C. Gies, F. Jahnke, S. Reitzenstein, S. Höfling, L. Worschech, and A. Forchel, Ultrafast tracking of second-order photon correlations in the emission of quantum-dot microresonator lasers, Phys. Rev. B **81**, 165314 (2010), doi:10.1103/PhysRevB.81.165314. 41, 42, 64, 67

[Ate07] S. Ates, S. M. Ulrich, P. Michler, S. Reitzenstein, A. Löffler, and A. Forchel, Coherence properties of high-β elliptical semiconductor micropillar lasers, Appl. Phys. Lett. **90**, 161111 (2007), doi:10.1063/1.2724908. 56, 58

[Ate08] S. Ates, C. Gies, S. M. Ulrich, J. Wiersig, S. Reitzenstein, A. Löffler, A. Forchel, F. Jahnke, and P. Michler, Influence of the spontaneous optical emission factor β on the first-order coherence of a semiconductor microcavity laser, Phys. Rev. B **78**, 155319 (2008), doi:10.1103/PhysRevB.78.155319. 48, 53, 55, 56, 67

[Baj07] D. Bajoni, P. Senellart, A. Lemaître, and J. Bloch, Photon lasing in GaAs microcavity: Similarities with a polariton condensate, Phys. Rev. B **76**, 201305 (2007), doi:10.1103/PhysRevB.76.201305. 71, 91

[Baj08] D. Bajoni, P. Senellart, E. Wertz, I. Sagnes, A. Miard, A. Lemaître, and J. Bloch, Polariton Laser Using Single Micropillar GaAs-GaAlAs Semiconductor Cavities, Phys. Rev. Lett. **100**, 047401 (2008), doi:10.1103/PhysRevLett.100.047401. 71, 79

[Bal07] R. Balili, V. Hartwell, D. Snoke, L. Pfeiffer, and K. West, Bose-Einstein Condensation of Microcavity Polaritons in a Trap, Science **316**, 1007 (2007), doi:10.1126/science.1140990. 71

[Bal09] R. Balili, B. Nelsen, D. W. Snoke, L. Pfeiffer, and K. West, Role of the stress trap in the polariton quasiequilibrium condensation in GaAs microcavities, Phys. Rev. B **79**, 075319 (2009), doi:10.1103/PhysRevB.79.075319. 71

[Bau08] J. J. Baumberg, A. V. Kavokin, S. Christopoulos, A. J. D. Grundy, R. Butté, G. Christmann, D. D. Solnyshkov, G. Malpuech, G. Baldassarri Höger von Högersthal, E. Feltin, J.-F. Carlin, and N. Grandjean, Spontaneous Polarization Buildup in a Room-Temperature Polariton Laser, Phys. Rev. Lett. **101**, 136409 (2008), doi:10.1103/PhysRevLett.101.136409. 71

[Bay99] M. Bayer, A. Kuther, A. Forchel, A. Gorbunov, V. B. Timofeev, F. Schäfer, J. P. Reithmaier, T. L. Reinecke, and S. N. Walck, Electron and Hole g Factors and Exchange Interaction from Studies of the Exciton Fine Structure in $In_{0.60}Ga_{0.40}As$ Quantum Dots, Phys. Rev. Lett. **82**, 1748 (1999), doi:10.1103/PhysRevLett.82.1748. 12

[Bay02] M. Bayer, G. Ortner, O. Stern, A. Kuther, A. A. Gorbunov, A. Forchel, P. Hawrylak, S. Fafard, K. Hinzer, T. L. Reinecke, S. N. Walck, J. P. Reithmaier, F. Klopf, and F. Schäfer, Fine structure of neutral and charged excitons in self-assembled In(Ga)As/(Al)GaAs quantum dots, Phys. Rev. B **65**, 195315 (2002), doi:10.1103/PhysRevB.65.195315. 11

[Ber61] M. G. A. Bernard and G. Duraffourg, Laser Conditions in Semiconductors, Phys. Status Solidi B **1**, 699 (1961), doi:10.1002/pssb.19610010703. 47, 69

[Ber71] V. L. Berezinskii, Destruction of Long-range Order in One-dimensional and Two-dimensional Systems having a Continuous Symmetry Group I. Classical Systems, Sov. Phys. JETP **32**, 493 (1971). 71

[Bil09] V. Bilykh, M. Nguyen, N. Sibeldin, M. Skorikov, V. Tsvetkov, and A. Sharkov, Emission dynamics of a GaAs microcavity with embedded quantum wells under intense nonresonant excitation, JETP Lett. **89**, 579 (2009), doi:10.1134/S0021364009110113. 83

[Bjö91] G. Björk and Y. Yamamoto, Analysis of semiconductor microcavity lasers using rate equations, IEEE J. Quantum Electron. **27**, 2386 (1991), doi:10.1109/3.100877. 2, 48

[Bjö94] G. Björk, A. Karlsson, and Y. Yamamoto, Definition of a laser threshold, Phys. Rev. A **50**, 1675 (1994), doi:10.1103/PhysRevA.50.1675. 16

[Böc08] C. Böckler, S. Reitzenstein, C. Kistner, R. Debusmann, A. Löffler, T. Kida, S. Höfling, A. Forchel, L. Grenouillet, J. Claudon, and J. M. Gérard, Electrically driven high-Q quantum dot-micropillar cavities, Appl. Phys. Lett. **92**, 091107 (2008), doi:10.1063/1.2890166. 60

[Bry90] G. W. Bryant, Biexciton binding in quantum boxes, Phys. Rev. B **41**, 1243 (1990), doi:10.1103/PhysRevB.41.1243. 12

[Car76] H. J. Carmichael and D. F. Walls, A quantum-mechanical master equation treatment of the dynamical Stark effect, J. Phys. B: At. Mol. Phys. **9**, 1199 (1976), doi:10.1088/0022-3700/9/8/007. 102

[Car78] H. J. Carmichael, P. Drummond, P. Meystre, and D. F. Walls, Intensity Correlations in Resonance Fluorescence with Atomic Number Fluctuations, J. Phys. A: Math. Gen. **11**, L121 (1978), doi:10.1088/0305-4470/11/5/007. 62, 101

[Cha85] Y.-C. Chang and J. N. Schulman, Interband optical transitions in GaAs-$Ga_{1-x}Al_xAs$ and InAs-GaSb superlattices, Phys. Rev. B **31**, 2069 (1985), doi:10.1103/PhysRevB.31.2069. 9

[Che88] Y. Chen, R. Cingolani, L. Andreani, F. Bassani, and J. Massies, Photoluminescence in quantum well and bulk GaAs: a direct comparative study, Il Nuovo Cimento D **10**, 847 (1988), doi:10.1007/BF02450144. 10

[Cho97] K. D. Choquette and H. Q. Hou, Vertical-Cavity Surface Emitting Lasers: Moving from Research to Manufacturing, Proc. IEEE **85**, 1730 (1997), doi:10.1109/5.649649. 1, 47

[Chr07] S. Christopoulos, G. Baldassarri Höger von Högersthal, A. J. D. Grundy, P. G. Lagoudakis, A. V. Kavokin, J. J. Baumberg, G. Christmann, R. Butté, E. Feltin, J.-F. Carlin, and N. Grandjean, Room-Temperature Polariton Lasing in Semiconductor Microcavities, Phys. Rev. Lett. **98**, 126405 (2007), doi:10.1103/PhysRevLett.98.126405. 2

[Chr12] G. Christmann, G. Tosi, N. G. Berloff, P. Tsotsis, P. S. Eldridge, Z. Hatzopoulos, P. G. Savvidis, and J. J. Baumberg, Polariton ring condensates and sunflower ripples in an expanding quantum liquid, Phys. Rev. B **85**, 235303 (2012), doi:10.1103/PhysRevB.85.235303. 78

[Dar06] A. Daraei, A. Tahraoui, D. Sanvitto, J. A. Timpson, P. W. Fry, M. Hopkinson, P. S. S. Guimarães, H. Vinck, D. M. Whittaker, M. S. Skolnick, and A. M. Fox, Control of polarized single quantum dot emission in high-quality-factor microcavity pillars, Appl. Phys. Lett. **88**, 051113 (2006), doi:10.1063/1.2171803. 59

[Dav95] K. B. Davis, M.-O. Mewes, M. R. Andrews, N. J. van Druten, D. S. Durfee, D. M. Kurn, and W. Ketterle, Bose-Einstein Condensation in a Gas of Sodium Atoms, Phys. Rev. Lett. **75**, 3969 (1995), doi:10.1103/PhysRevLett.75.3969. 71

[Dem03] W. Demtröder, *Laser spectroscopy*, Springer, Berlin, third ed. (2003), ISBN 3-540-65225-6. 29

[Den02] H. Deng, G. Weihs, C. Santori, J. Bloch, and Y. Yamamoto, Condensation of Semiconductor Microcavity Exciton Polaritons, Science **298**, 199 (2002), doi:10.1126/science.1074464. 37, 82, 83

[Den03] H. Deng, G. Weihs, D. Snoke, J. Bloch, and Y. Yamamoto, Polariton lasing vs. photon lasing in a semiconductor microcavity, Proc. Natl. Acad. Sci. USA **100**, 15318 (2003), doi:10.1073/pnas.2634328100. 71, 83

[Den06] H. Deng, *Dynamic Condensation of Semiconductor Microcavity Polaritons*, Ph.D. thesis, Stanford University (2006). 35

[Den07] H. Deng, G. S. Solomon, R. Hey, K. H. Ploog, and Y. Yamamoto, Spatial Coherence of a Polariton Condensate, Phys. Rev. Lett. **99**, 126403 (2007), doi:10.1103/PhysRevLett.99.126403. 71

[Den10] H. Deng, H. Haug, and Y. Yamamoto, Exciton-polariton Bose-Einstein condensation, Rev. Mod. Phys. **82**, 1489 (2010), doi:10.1103/RevModPhys.82.1489. 13, 15, 69, 74

[Dud12] Y. O. Dudin, L. Li, F. Bariani, and A. Kuzmich, Observation of coherent many-body Rabi oscillations, Nat. Phys. **8**, 790 (2012), 10.1038/nphys2413. 1

[Ein24] A. Einstein, Quantentheorie des einatomigen idealen Gases, Sitzungsber. K. Preuss. Akad. Wiss. **261**, 3 (1924). 70

[Gam95] D. Gammon, S. Rudin, T. L. Reinecke, D. S. Katzer, and C. S. Kyono, Phonon broadening of excitons in GaAs/$Al_xGa_{1-x}As$ quantum wells, Phys. Rev. B **51**, 16785 (1995), doi:10.1103/PhysRevB.51.16785. 94

[Gap98] S. V. Gaponenko, *Optical Properties of Semiconductor Nanocrystals*, Cambridge Studies in Modern Optics, Cambridge Univ. Press, Cambridge (1998). 6, 8, 11

[Gay98] B. Gayral, J. M. Gérard, B. Legrand, E. Costard, and V. Thierry-Mieg, Optical study of GaAs/AlAs pillar microcavities with elliptical cross section, Appl. Phys. Lett. **72**, 1421 (1998), doi:10.1063/1.120582. 53

[Gér96] J. M. Gérard, D. Barrier, J. Y. Marzin, R. Kuszelewicz, L. Manin, E. Costard, V. Thierry-Mieg, and T. Rivera, Quantum boxes as active probes for photonic microstructures: The pillar microcavity case, Appl. Phys. Lett. **69**, 449 (1996), doi:10.1063/1.118135. 49, 52

[Gér98] J. M. Gérard, B. Sermage, B. Gayral, B. Legrand, E. Costard, and V. Thierry-Mieg, Enhanced Spontaneous Emission by Quantum Boxes in a Monolithic Optical Microcavity, Phys. Rev. Lett. **81**, 1110 (1998), doi:10.1103/PhysRevLett.81.1110. 37, 48, 49

[Gie07] C. Gies, J. Wiersig, M. Lorke, and F. Jahnke, Semiconductor model for quantum-dot-based microcavity lasers, Phys. Rev. A **75**, 013803 (2007), doi:10.1103/PhysRevA.75.013803. 12, 47, 53, 67

[Gla63] R. J. Glauber, Photon Correlations, Phys. Rev. Lett. **10**, 84 (1963), doi:10.1103/PhysRevLett.10.84. 25

[Gru06] M. Grundmann, *The Physics of Semiconductors*, Springer, Berlin Heidelberg (2006). 6, 8

[Gut98] T. Gutbrod, M. Bayer, A. Forchel, J. P. Reithmaier, T. L. Reinecke, S. Rudin, and P. A. Knipp, Weak and Strong Coupling of Photons and Excitons in Photonic Dots, Phys. Rev. B **57**, 9950 (1998), doi:10.1103/PhysRevB.57.9950. 15

[HB56] R. Hanbury-Brown and R. Q. Twiss, Correlation Between Photons in Two Coherent Beams, Nature **177**, 27 (1956), doi:10.1038/177027a0. 29

[Hen03] M. Hennrich, *Kontrollierte Erzeugung einzelner Photonen in einem optischen Resonator hoher Finesse*, Ph.D. thesis, LMU München (2003). 102

[Hin01] K. Hinzer, P. Hawrylak, M. Korkusinski, S. Fafard, M. Bayer, O. Stern, A. Gorbunov, and A. Forchel, Optical spectroscopy of a single $Al_{0.36}In_{0.64}As/Al_{0.33}Ga_{0.67}As$ quantum dot, Phys. Rev. B **63**, 075314 (2001), doi:10.1103/PhysRevB.63.075314. 12

[Hoh67] P. C. Hohenberg, Existence of Long-Range Order in One and Two Dimensions, Phys. Rev. **158**, 383 (1967), doi:10.1103/PhysRev.158.383. 71

[Hoh09] U. Hohenester, A. Laucht, M. Kaniber, N. Hauke, A. Neumann, A. Mohtashami, M. Seliger, M. Bichler, and J. J. Finley, Phonon-assisted transitions from quantum dot excitons to cavity photons, Phys. Rev. B **80**, 201311 (2009), doi:10.1103/PhysRevB.80.201311. 67

[Hou94a] R. Houdré, R. P. Stanley, U. Oesterle, M. Ilegems, and C. Weisbuch, Room-temperature cavity polaritons in a semiconductor microcavity, Phys. Rev. B **49**, 16761 (1994), doi:10.1103/PhysRevB.49.16761. 87

[Hou94b] R. Houdré, C. Weisbuch, R. P. Stanley, U. Oesterle, P. Pellandini, and M. Ilegems, Measurement of Cavity-Polariton Dispersion Curve from Angle-Resolved Photoluminescence Experiments, Phys. Rev. Lett. **73**, 2043 (1994), doi:10.1103/PhysRevLett.73.2043. 72

[Hou95] R. Houdré, J. L. Gibernon, P. Pellandini, R. P. Stanley, U. Oesterle, C. Weisbuch, J. O'Gorman, B. Roycroft, and M. Ilegems, Saturation of the Strong-Coupling Regime in a Semiconductor Microcavity: Free-Carrier Bleaching of Cavity Polaritons, Phys. Rev. B **52**, 7810 (1995), doi:10.1103/PhysRevB.52.7810. 86

[Hua91] D. Huang, E. A. Swanson, C. P. Lin, J. S. Schuman, W. G. Stinson, W. Chang, M. R. Hee, T. Flotte, K. Gregory, C. A. Puliafito, and J. G. Fujimoto, Optical Coherence Tomography, Science **254**, 1178 (1991), doi:10.1126/science.1957169. 29

[Ima96] A. Imamoğlu, R. J. Ram, S. Pau, and Y. Yamamoto, Nonequilibrium Condensates and Lasers Without Inversion: Exciton-Polariton Lasers, Phys. Rev. A **53**, 4250 (1996), doi:10.1103/PhysRevA.53.4250. 2, 69

[Jah96] F. Jahnke, M. Kira, S. W. Koch, G. Khitrova, E. K. Lindmark, J. T. R. Nelson, D. V. Wick, J. D. Berger, O. Lyngnes, H. M. Gibbs, and K. Tai, Excitonic Nonlinearities of Semiconductor Microcavities in the Nonperturbative Regime, Phys. Rev. Lett. **77**, 5257 (1996), doi:10.1103/PhysRevLett.77.5257. 22

[Kam12] E. Kammann, H. Ohadi, M. Maragkou, A. V. Kavokin, and P. G. Lagoudakis, Crossover from photon to exciton-polariton lasing, New J. Phys. **14**, 105003 (2012), doi:10.1088/1367-2630/14/10/105003. 80

[Kao66] C. K. Kao and G. A. Hockham, Dielectric-fibre Surface Waveguides for Optical Frequencies, Proceedings of the IEE **113**, 1151 (1966), doi:10.1049/piee.1966.0189. 1

[Kas06] J. Kasprzak, M. Richard, S. Kundermann, A. Baas, P. Jeambrun, J. M. Keeling, F. Marchetti, M. Szymańska, R. André, J. Staehli, V. Savona, P. B. Littlewood, B. Deveaud, and L. S. Dang, Bose-Einstein Condensation of Exciton Polaritons, Nature **443**, 409 (2006), doi:10.1038/nature05131. 71

[Kas08a] J. Kasprzak, M. Richard, A. Baas, B. Deveaud, R. André, J.-P. Poizat, and L. S. Dang, Second-Order Time Correlations within a Polariton Bose-Einstein Condensate in a CdTe Microcavity, Phys. Rev. Lett. **100**, 067402 (2008), doi:10.1103/PhysRevLett.100.067402. 37, 82

[Kas08b] J. Kasprzak, D. D. Solnyshkov, R. André, L. S. Dang, and G. Malpuech, Formation of an Exciton Polariton Condensate: Thermodynamic versus Kinetic Regimes, Phys. Rev. Lett. **101**, 146404 (2008), doi:10.1103/PhysRevLett.101.146404. 93, 97

[Kav07] A. V. Kavokin, J. J. Baumberg, G. Malpuech, and F. P. Laussy, *Microcavities*, Oxford University Press (2007). 12, 15, 17, 69

[Khi34] A. Khintchine, Korrelationstheorie der stationären stochastischen Prozesse, Math. Ann. **109**, 604 (1934), doi:10.1007/BF01449156, 10.1007/BF01449156. 24

[Khi06] G. Khitrova, H. M. Gibbs, M. Kira, S. W. Koch, and A. Scherer, Vacuum Rabi splitting in semiconductors, Nat. Phys. **2**, 81 (2006), doi:10.1038/nphys227. 2, 22

[Kir97] M. Kira, F. Jahnke, S. W. Koch, J. D. Berger, D. V. Wick, T. R. Nelson, G. Khitrova, and H. M. Gibbs, Quantum Theory of Nonlinear Semiconductor Microcavity Luminescence Explaining "Boser" Experiments, Phys. Rev. Lett. **79**, 5170 (1997), doi:10.1103/PhysRevLett.79.5170. 97

[Kli05] C. Klingshirn, *Semiconductor Optics*, Springer, Berlin Heidelberg, second ed. (2005). 6, 9, 18

[Kop07] K. Kopitzki and P. Herzog, *Einführung in die Festkörperphysik*, Teubner, Wiesbaden, 6 ed. (2007), doi:10.1007/978-3-8351-9127-3. 10

[Kos73] J. M. Kosterlitz and D. J. Thouless, Ordering, Metastability and Phase Transitions in Two-Dimensional Systems, J. Phys. C: Solid State Phys. **6**, 1181 (1973), doi:10.1088/0022-3719/6/7/010. 71

[Kri91] M. P. C. M. Krijn, Heterojunction band offsets and effective masses in III-V quaternary alloys, Semicond. Sci. Technol. **6**, 27 (1991), doi:10.1088/0268-1242/6/1/005. 5

[Kuk95] D. V. Kuksenkov, H. Temkin, and S. Swirhun, Polarization instability and relative intensity noise in vertical-cavity surface-emitting lasers, Appl. Phys. Lett. **67**, 2141 (1995), doi:10.1063/1.114746. 56

[Lag08] K. G. Lagoudakis, M. Wouters, M. Richard, A. Baas, I. Carusotto, R. Andre, L. Dang, and B. Deveaud-Plédran, Quantized Vortices in an Exciton-Polariton Condensate, Nat. Phys. **4**, 706 (2008), doi:10.1038/nphys1051. 71

[Lag09] K. G. Lagoudakis, T. Ostatnicky, A. V. Kavokin, Y. G. Rubo, R. Andre, and B. Deveaud-Plédran, Observation of Half-Quantum Vortices in an Exciton-Polariton Condensate, Science **326**, 974 (2009), doi:10.1126/science.1177980. 71

[Lau10] A. Laucht, M. Kaniber, A. Mohtashami, N. Hauke, M. Bichler, and J. J. Finley, Temporal monitoring of nonresonant feeding of semiconductor nanocavity modes by quantum dot multiexciton transitions, Phys. Rev. B **81**, 241302 (2010), doi:10.1103/PhysRevB.81.241302. 67

[Led11] N. N. Ledentsov, Quantum dot laser, Semiconductor Science and Technology **26**, 014001 (2011), doi:10.1088/0268-1242/26/1/014001. 1

[Leo94] D. Leonard, K. Pond, and P. M. Petroff, Critical layer thickness for self-assembled InAs islands on GaAs, Phys. Rev. B **50**, 11687 (1994), doi:10.1103/PhysRevB.50.11687. 11

[Leo98] R. Leon and S. Fafard, Structural and radiative evolution in quantum dots near the $In_xGa_{1-x}As/GaAs$ Stranski-Krastanow transformation, Phys. Rev. B **58**, R1726 (1998), doi:10.1103/PhysRevB.58.R1726. 11

[Li00] E. Li, Material parameters of InGaAsP and InAlGaAs systems for use in quantum well structures at low and room temperatures, Physica E **5**, 215 (2000), doi:10.1016/S1386-9477(99)00262-3. 10

[Löf05] A. Löffler, J. P. Reithmaier, G. Sek, C. Hofmann, S. Reitzenstein, M. Kamp, and A. Forchel, Semiconductor quantum dot microcavity pillars with high-quality factors and enlarged dot dimensions, Appl. Phys. Lett. **86**, 111105 (2005), doi:10.1063/1.1880446. 15, 49, 50

[Loh06] H. Lohmeyer, C. Kruse, K. Sebald, J. Gutowski, and D. Hommel, Enhanced spontaneous emission of CdSe quantum dots in monolithic II-VI pillar microcavities, Appl. Phys. Lett. **89**, 091107 (2006), doi:10.1063/1.2338800. 48

[Lou73] R. Loudon, *The Quantum Theory of Light*, Clarendon Press, Oxford (1973). 23

[Lou05] B. Lounis and M. Orrit, Single-photon sources, Rep. Prog. Phys. **68**, 1129 (2005), doi:10.1088/0034-4885/68/5/R04. 29, 36, 62

[Lov08] A. P. D. Love, D. N. Krizhanovskii, D. M. Whittaker, R. Bouchekioua, D. Sanvitto, S. A. Rizeiqi, R. Bradley, M. S. Skolnick, P. R. Eastham, R. André, and L. S. Dang, Intrinsic Decoherence Mechanisms in the Microcavity Polariton Condensate, Phys. Rev. Lett. **101**, 067404 (2008), doi:10.1103/PhysRevLett.101.067404. 37, 82

[Lu12] T.-C. Lu, Y.-Y. Lai, Y.-P. Lan, S.-W. Huang, J.-R. Chen, Y.-C. Wu, W.-F. Hsieh, and H. Deng, Room temperature polariton lasing vs. photon lasing in a ZnO-based hybrid microcavity, Opt. Express **20**, 5530 (2012), doi:10.1364/OE.20.005530. 2

[Mai60] T. H. Maiman, Stimulated Optical Radiation in Ruby, Nature **187**, 493 (1960), doi:10.1038/187493a0. 1

[Man95] L. Mandel and E. Wolf, *Optical Coherence and Quantum Optics*, Cambridge University Press (1995). 23

[Mar88] F. D. Martini and G. R. Jacobovitz, Anomalous Spontaneous-Stimulated-Decay Phase Transition and Zero Threshold Laser Action in a Microscopic Cavity, Phys. Rev. Lett. **60**, 1711 (1988), doi:10.1103/PhysRevLett.60.2811. 2. 48

[Mar10] M. Maragkou, A. J. D. Grundy, T. Ostatnicky, and P. G. Lagoudakis, Longitudinal optical phonon assisted polariton laser, Appl. Phys. Lett. **97**, 111110 (2010), doi:10.1063/1.3488012. 78, 79, 95

[McC92] S. L. McCall, A. F. J. Levi, R. E. Slusher, S. J. Pearton, and R. A. Logan, Whispering-gallery mode microdisk lasers, Appl. Phys. Lett. **60**, 289 (1992), doi:10.1063/1.106688. 16

[Mer66] N. D. Mermin and H. Wagner, Absence of Ferromagnetism or Antiferromagnetism in One- or Two-Dimensional Isotropic Heisenberg Models, Phys. Rev. Lett. **17**, 1133 (1966), doi:10.1103/PhysRevLett.17.1133. 71

[Mic00] P. Michler, A. Imamoğlu, M. D. Mason, P. J. Carson, G. F. Strouse, and S. K. Buratto, Quantum correlation among photons from a single quantum dot at room temperature, Nature **406**, 968 (2000), doi:10.1038/35023100. 63

[Moh94] U. Mohideen, R. E. Slusher, F. Jahnke, and S. W. Koch, Semiconductor Microlaser Linewidths, Phys. Rev. Lett. **73**, 1785 (1994), doi:10.1103/PhysRevLett.73.1785. 78, 91

[Mor01] E. Moreau, I. Robert, J. M. Gérard, I. Abram, L. Manin, and V. Thierry-Mieg, Single-mode solid-state single photon source based on isolated quantum dots in pillar microcavities, Appl. Phys. Lett. **79**, 2865 (2001), doi:10.1063/1.1415346. 56

[Muq11] M. M. K. Muqit, G. R. Marcellino, D. B. Henson, L. B. Young, G. S. Turner, and P. E. Stanga, Pascal panretinal laser ablation and regression analysis in proliferative diabetic retinopathy: Manchester Pascal Study Report 4, Eye **25**, 1447 (2011), doi:10.1038/eye.2011.188. 1

[Oze05] R. Ozeri, N. Katz, J. Steinhauer, and N. Davidson, *Colloquium*: Bulk Bogoliubov excitations in a Bose-Einstein condensate, Rev. Mod. Phys. **77**, 187 (2005), doi:10.1103/RevModPhys.77.187. 75

[Pan99] G. Panzarini, L. C. Andreani, A. Armitage, D. Baxter, M. S. Skolnick, V. N. Astratov, J. S. Roberts, A. V. Kavokin, M. R. Vladimirova, and M. A. Kaliteevski, Exciton-Light Coupling in Single and Coupled Semiconductor Microcavities: Polariton Dispersion and Polarization Splitting, Phys. Rev. B **59**, 5082 (1999), doi:10.1103/PhysRevB.59.5082. 14

[Phi96] R. T. Phillips, G. C. Nixon, T. Fujita, M. Y. Simmons, and D. A. Ritchie, Excitonic trions in undoped GaAs quantum wells, Solid State Commun. **98**, 287 (1996), doi:10.1016/0038-1098(96)00069-5. 95

[Por02] D. Porras, C. Ciuti, J. J. Baumberg, and C. Tejedor, Polariton dynamics and Bose-Einstein condensation in semiconductor microcavities, Phys. Rev. B **66**, 085304 (2002), doi:10.1103/PhysRevB.66.085304. 95

[Por03] D. Porras and C. Tejedor, Linewidth of a polariton laser: Theoretical analysis of self-interaction effects, Phys. Rev. B **67**, 161310 (2003), doi:10.1103/PhysRevB.67.161310. 81

[Pur46] E. M. Purcell, Spontaneous Emission Probabilities at Radio Frequencies, Phys. Rev. **69**, 681 (1946). 16, 37

[Rei06] S. Reitzenstein, A. Bazhenov, A. Gorbunov, C. Hofmann, S. Münch, A. Löffler, M. Kamp, J. P. Reithmaier, V. D. Kulakovskii, and A. Forchel, Lasing in high-Q quantum-dot micropillar cavities, Appl. Phys. Lett. **89**, 051107 (2006), doi:10.1063/1.2266231. 49, 53

[Rei07] S. Reitzenstein, C. Hofmann, A. Gorbunov, M. Strauss, S. H. Kwon, C. Schneider, A. Löffler, S. Höfling, M. Kamp, and A. Forchel, AlAs/GaAs Micropillar Cavities with Quality Factors Exceeding 150.000, Appl. Phys. Lett. **90**, 251109 (2007), doi:10.1063/1.2749862. 15, 52

[Rei08] S. Reitzenstein, T. Heindel, C. Kistner, A. Rahimi-Iman, C. Schneider, S. Höfling, and A. Forchel, Low threshold electrically pumped quantum dot-micropillar lasers, Appl. Phys. Lett. **93**, 061104 (2008), doi:10.1063/1.2969397. 16, 60

[Rei10] S. Reitzenstein and A. Forchel, Quantum Dot Micropillars, J. Phys. D: Appl. Phys. **43**, 033001 (2010), doi:10.1088/0022-3727/43/3/033001. 47, 50, 52

[Ric78] T. M. Rice, The Electron-Hole Liquid in Semiconductors: Theoretical Aspects, in *Advances in Research and Applications* (edited by H. Ehrenreich, F. Seitz, and D. Turnbull), vol. 32 of *Solid State Physics*, pp. 1 – 86, Academic Press (1978), doi:10.1016/S0081-1947(08)60438-5. 95

[Ric94] P. R. Rice and H. J. Carmichael, Photon Statistics of a Cavity-QED Laser: A Comment on the Laser–Phase-Transition Analogy, Phys. Rev. A **50**, 4318 (1994), doi:10.1103/PhysRevA.50.4318. 17, 48, 53

[Ric05] M. Richard, J. Kasprzak, R. Romestain, R. André, and L. S. Dang, Spontaneous Coherent Phase Transition of Polaritons in CdTe Microcavities, Phys. Rev. Lett. **94**, 187401 (2005), doi:10.1103/PhysRevLett.94.187401. 71, 78

[Rod12] R. Rodes, J. Estaran, B. Li, M. Mueller, J. B. Jensen, T. Gründl, M. Ortsiefer, C. Neumeyr, J. Rosskopf, K. J. Larsen, M.-C. Amann, and I. T. Monroy, 100 Gb/s single VCSEL data transmission link, in *Optical Fiber Communication Conference*, p. PDP5D.10, Optical Society of America (2012). 1

[Rou11] G. Roumpos, *Phase Fluctuations in Microcavity Exciton Polariton Condensation*, Ph.D. thesis, Stanford University (2011). 10

[Sab01] M. Saba, C. Ciuti, J. Bloch, V. Thierry-Mieg, R. Andre, L. S. Dang, S. Kundermann, A. Mura, G. Bongiovanni, J. L. Staehli, and B. Deveaud, High-temperature ultrafast polariton parametric amplification in semiconductor microcavities, Nature **414**, 731 (2001), doi:10.1038/414731a. 86

[San02] C. Santori, D. Fattal, J. Vučković, G. S. Solomon, and Y. Yamamoto, Indistinguishable photons from a single-photon device, Nature **419**, 594 (2002), doi:10.1038/nature01086. 66

[Sar08] D. Sarchi, P. Schwendimann, and A. Quattropani, Effects of Noise in Different Approaches for the Statistics of Polariton Condensates, Phys. Rev. B **78**, 073404 (2008), doi:10.1103/PhysRevB.78.073404. 83

[Sav95] V. Savona, L. C. Andreani, P. Schwendimann, and A. Quattropani, Quantum Well Excitons in Semiconductor Microcavities: Unified Treatment of Weak and Strong Coupling Regimes, Solid State Commun. **93**, 733 (1995), doi:10.1016/0038-1098(94)00865-5. 12, 73

[Sch08] P. Schwendimann and A. Quattropani, Statistics of the Polariton Condensate, Phys. Rev. B **77**, 085317 (2008), doi:10.1103/PhysRevB.77.085317. 83, 93

[Sch10] P. Schwendimann, A. Quattropani, and D. Sarchi, Stationary and time-dependent correlations in polariton condensates, Phys. Rev. B **82**, 205329 (2010), doi:10.1103/PhysRevB.82.205329. 93

[Sko02] M. S. Skolnick, R. M. Stevenson, A. I. Tartakovskii, R. Butté, M. Emam-Ismail, D. M. Whittaker, P. G. Savvidis, J. J. Baumberg, A. Lemaître, V. N. Astratov, and J. S. Roberts, Polariton-polariton interactions and stimulated scattering in semiconductor microcavities, Mater. Sci. Eng., C **19**, 407 (2002), doi:10.1016/S0928-4931(01)00433-7. 83

[Smi09] B. Smith, *Fundamentals of Fourier Transform Infrared Spectroscopy*, Taylor & Francis, second ed. (2009), ISBN 9781420069297. 29

[Sno08] D. Snoke, Predicting the ionization threshold for carriers in excited semiconductors, Solid State Commun. **146**, 73 (2008), doi:10.1016/j.ssc.2008.01.012. 95

[Sol01] G. S. Solomon, M. Pelton, and Y. Yamamoto, Single-mode Spontaneous Emission from a Single Quantum Dot in a Three-Dimensional Microcavity, Phys. Rev. Lett. **86**, 3903 (2001), doi:10.1103/PhysRevLett.86.3903. 48

[Stu11] C. Sturm, H. Hilmer, R. Schmidt-Grund, and M. Grundmann, Exciton–polaritons in a ZnO-based microcavity: polarization dependence and nonlinear occupation, New J. Phys. **13**, 033014 (2011), doi:10.1088/1367-2630/13/3/033014. 35

[Szc04] J. Szczytko, L. Kappei, J. Berney, F. Morier-Genoud, M. T. Portella-Oberli, and B. Deveaud, Determination of the Exciton Formation in Quantum Wells from Time-Resolved Interband Luminescence, Phys. Rev. Lett. **93**, 137401 (2004), doi:10.1103/PhysRevLett.93.137401. 97

[Tar00] A. I. Tartakovskii, M. Emam-Ismail, R. M. Stevenson, M. S. Skolnick, V. N. Astratov, D. M. Whittaker, J. J. Baumberg, and J. S. Roberts, Relaxation Bottleneck and its Suppression in Semiconductor Microcavities, Phys. Rev. B **62**, R2283 (2000), doi:10.1103/PhysRevB.62.R2283. 83, 95, 97

[Tas97] F. Tassone, C. Piermarocchi, V. Savona, A. Quattropani, and P. Schwendimann, Bottleneck Effects in the Relaxation and Photoluminescence of Microcavity Polaritons, Phys. Rev. B **56**, 7554 (1997), doi:10.1103/PhysRevB.56.7554. 95

[Tel90] B. Tell, Y. H. Lee, K. F. Brown-Goebeler, J. L. Jewell, R. E. Leibenguth, M. T. Asom, G. Livescu, L. Luther, and V. D. Mattera, High-power cw vertical-cavity top surface-emitting GaAs quantum well lasers, Appl. Phys. Lett. **57**, 1855 (1990), doi:10.1063/1.104038. 1

[Tsi08] S. I. Tsintzos, N. T. Pelekanos, G. Konstantinidis, Z. Hatzopoulos, and P. G. Savvidis, A GaAs Polariton Light-Emitting Diode Operating Near Room Temperature, Nature **453**, 372 (2008), doi:10.1038/nature06979. 86, 87

[Tsi09] S. I. Tsintzos, P. G. Savvidis, G. Deligeorgis, Z. Hatzopoulos, and N. T. Pelekanos, Room temperature GaAs exciton-polariton light emitting diode, Appl. Phys. Lett. **94**, 071109 (2009), doi:10.1063/1.3082093. 86, 87

[Tso12] P. Tsotsis, P. S. Eldridge, T. Gao, S. I. Tsintzos, Z. Hatzopoulos, and P. G. Savvidis, Lasing threshold doubling at the crossover from strong to weak coupling regime in GaAs microcavity, New J. Phys. **14**, 023060 (2012), doi:10.1088/1367-2630/14/2/023060. 91

[Ulr07] S. M. Ulrich, C. Gies, S. Ates, J. Wiersig, S. Reitzenstein, C. Hofmann, A. Löffler, A. Forchel, F. Jahnke, and P. Michler, Photon Statistics of Semiconductor Microcavity Lasers, Phys. Rev. Lett. **98**, 043906 (2007), doi:10.1103/PhysRevLett.98.043906. 36, 48, 67

[Uni05] D. C. Unitt, A. J. Bennett, P. Atkinson, D. A. Ritchie, and A. J. Shields, Polarization control of quantum dot single-photon sources via a dipole-dependent Purcell effect, Phys. Rev. B **72**, 033318 (2005), doi:10.1103/PhysRevB.72.033318. 56

[Uts08] S. Utsunomiya, L. Tian, G. Roumpos, C. W. Lai, N. Kumada, T. Fujisawa, M. Kuwata-Gonokami, A. Löffler, S. Höfling, A. Forchel, and Y. Yamamoto, Observation of Bogoliubov excitations in exciton-polariton condensates, Nat. Phys. **4**, 700 (2008), doi:10.1038/nphys1034. 75

[Vah03] K. J. Vahala, Optical microcavities, Nature **424**, 839 (2003), doi:10.1038/nature01939. 12, 47

[Vas99] F. T. Vasko and A. V. Kuznetsov, *Electronic States and Optical Transitions in Semiconductor Heterostructures*, Springer, New York (1999). 8

[Wan05] W. H. Wang, S. Ghosh, F. M. Mendoza, X. Li, D. D. Awschalom, and N. Samarth, Static and dynamic spectroscopy of (Al,Ga)As/GaAs microdisk lasers with interface fluctuation quantum dots, Phys. Rev. B **71**, 155306 (2005), doi:10.1103/PhysRevB.71.155306. 81

[Wei91] C. Weisbuch and B. Vinter, *Quantum semiconductor structures: Fundamentals and Applications*, Academic Press, London (1991). 6, 7, 8, 9

[Wei92] C. Weisbuch, M. Nishioka, A. Ishikawa, and Y. Arakawa, Observation of the coupled exciton-photon mode splitting in a semiconductor quantum microcavity, Phys. Rev. Lett. **69**, 3314 (1992), doi:10.1103/PhysRevLett.69.3314. 2

[Wer09] E. Wertz, L. Ferrier, D. D. Solnyshkov, P. Senellart, D. Bajoni, A. Miard, A. Lemaître, G. Malpuech, and J. Bloch, Spontaneous formation of a polariton condensate in a planar GaAs microcavity, Appl. Phys. Lett. **95**, 051108 (2009), doi:10.1063/1.3192408. 69, 71, 79, 93, 97

[Whi96] D. M. Whittaker, P. Kinsler, T. A. Fisher, M. S. Skolnick, A. Armitage, A. M. Afshar, M. D. Sturge, and J. S. Roberts, Motional Narrowing in Semiconductor Microcavities, Phys. Rev. Lett. **77**, 4792 (1996), doi:10.1103/PhysRevLett.77.4792. 14

[Wie09] J. Wiersig, C. Gies, F. Jahnke, M. Aßmann, T. Berstermann, M. Bayer, C. Kistner, S. Reitzenstein, C. Schneider, S. Höfling, A. Forchel, C. Kruse, J. Kalden, and D. Hommel, Direct observation of correlations between individual photon emission events of a microcavity laser, Nature **460**, 245 (2009), doi:10.1038/nature08126. 37, 48, 61, 62, 64, 65, 67

[Wie10] J. Wiersig, Microscopic theory of first-order coherence in microcavity lasers based on semiconductor quantum dots, Phys. Rev. B **82**, 155320 (2010), doi:10.1103/PhysRevB.82.155320. 48, 54, 56

[Win09] M. Winger, T. Volz, G. Tarel, S. Portolan, A. Badolato, K. J. Hennessy, E. L. Hu, A. Beveratos, J. Finley, V. Savona, and A. Imamoğlu, Explanation of Photon Correlations in the Far-Off-Resonance Optical Emission from a Quantum-Dot-Cavity System, Phys. Rev. Lett. **103**, 207403 (2009), doi: 10.1103/PhysRevLett.103.207403. 67

[Wit11] M. Witzany, R. Roßbach, W.-M. Schulz, M. Jetter, P. Michler, T.-L. Liu, E. Hu, J. Wiersig, and F. Jahnke, Lasing properties of InP/($Ga_{0.51}In_{0.49}$)P quantum dots in microdisk cavities, Phys. Rev. B **83**, 205305 (2011), doi: 10.1103/PhysRevB.83.205305. 36

[Wou07] M. Wouters and I. Carusotto, Excitations in a Nonequilibrium Bose-Einstein Condensate of Exciton Polaritons, Phys. Rev. Lett. **99**, 140402 (2007), doi: 10.1103/PhysRevLett.99.140402. 76

[Wou08] M. Wouters, I. Carusotto, and C. Ciuti, Spatial and spectral shape of inhomogeneous nonequilibrium exciton-polariton condensates, Phys. Rev. B **77**, 115340 (2008), doi:10.1103/PhysRevB.77.115340. 76, 78, 89

[Yam91] Y. Yamamoto, S. Machida, and G. Björk, Microcavity Semiconductor Laser with Enhanced Spontaneous Emission, Phys. Rev. A **44**, 657 (1991), doi: 10.1103/PhysRevA.44.657. 2, 17

[Yam92] Y. Yamamoto, S. Machida, and G. Björk, Micro-cavity semiconductor lasers with controlled spontaneous emission, Opt. Quantum Electron. **24**, S215 (1992), doi:10.1007/BF00625826. 48

[Yeh88] P. Yeh, *Optical Waves in Layered Media*, J. Wiley & Sons, New York (1988). 13

List of Figures

Index

Symbols and Abbreviations

Symbol	Meaning
a_B	Bohr radius of the hydrogen atom
α_{1s}	Exciton Bohr radius
β	Spontaneous emission factor
BEC	Bose-Einstein condensate
c	Speed of light (299792458 m/s)
C_k, H_k	Hopfield coefficients
CB, VB	Conduction band, valence band
CCD	Charge-coupled device
cw	Continuous wave
$D(E)$	Electronic density of states
d	Diameter
Δ_0	Cavity-exciton detuning
DBR	Distributed Bragg reflector
e	Electron, unit charge ($1.602176 \cdot 10^{-19}$ C)
E_b	Exciton binding energy
E_gap	Band-gap energy
E_Ry	Rydberg energy
F_P	Purcell factor
FM	Fundamental mode (of a microcavity)
$G^{(1)}, G^{(2)}$	General correlation function of first, second order
$g^{(1)}, g^{(2)}, \cdots, g^{(m)}$	Normalised correlation function of first, second, mth order
γ	Decay rate
g	Coupling factor
$\hbar$	$h/2\pi = 1.054571 \cdot 10^{-34}$ Js $= 6.582118 \cdot 10^{-16}$ eVs
H_k, C_k	Hopfield coefficients
HBT	Hanbury-Brown-Twiss

i/o	input-output
k_B	Boltzmann constant ($1.38062 \cdot 10^{-23}\,\mathrm{J/K}$)
$\vec{k}, k_{\|\|}$	Wave vector, in-plane wave vector
λ	Wavelength
L_eff	Effective cavity length
LP, UP	Lower, upper polariton
m_0	Free electron mass ($9.109381 \cdot 10^{-31}$ kg)
m^*	Effective mass of a (quasi-) particle in the solid state
MBE	Molecular beam epitaxy
MCP	Micro-channel plate
MI	Michelson interferometer
MO	Microscope objective
n	Refractive index or photon number of a light state, see context
$\hat{n}$	Photon-number operator
NA	Numerical aperture
P	Excitation power
PL	Photoluminescence
Q	Quality factor
QD, QW	Quantum dot, quantum well
R	Reflectivity
$\rho(\omega)$	Optical density of states
ρ_L	Degree of linear polarisation
τ_c	Coherence time, without index: delay time
t	Time
T	Temperature
θ	Emission angle
ϑ	Angle of polarisation
UP, LP	Upper, lower polariton
V	Visibility
VB, CB	Valence band, conduction band
VCSEL	Vertical-cavity surface-emitting laser
Ω_R	Rabi frequency

Publications

Parts of this work are or will be published as follows:

P1: M. Aßmann, F. Veit, **J.-S. Tempel**, T. Berstermann, H. Stolz, M. van der Poel, J. M. Hvam, and M. Bayer: "*Measuring the dynamics of second-order photon correlation functions inside a pulse with picosecond time resolution.*"
Opt. Express **18**, 20229-20241 (2010).
Available at http://dx.doi.org/10.1364/OE.18.020229

P2: M. Aßmann, **J.-S. Tempel**, F. Veit, M. Bayer, A. Rahimi-Iman, A. Löffler, S. Höfling, S. Reitzenstein, L. Worschech, and A. Forchel: "*From polariton condensates to highly photonic quantum degenerate states of bosonic matter.*"
Proc. Natl. Acad. Sci. U.S.A. **108**, 1804-1809 (2011).
Available at http://dx.doi.org/10.1073/pnas.1009847108

P3: **J.-S. Tempel**, I. A. Akimov, M. Aßmann, C. Schneider, S. Höfling, C. Kistner, S. Reitzenstein, L. Worschech, A. Forchel, and M. Bayer: "*Extrapolation of the intensity autocorrelation function of a quantum-dot micropillar laser into the thermal emission regime.*"
J. Opt. Soc. Am. B **28**, 1404-1408 (2011).
Available at http://dx.doi.org/10.1364/JOSAB.28.001404

P4: **J.-S. Tempel**, F. Veit, M. Aßmann, L. E. Kreilkamp, A. Rahimi-Iman, A. Löffler, S. Höfling, S. Reitzenstein, L. Worschech, A. Forchel, and M. Bayer: "*Characterization of two-threshold behavior of the emission from a GaAs microcavity.*"
Phys. Rev. B **85**, 075318 (2012).
Available at http://dx.doi.org/10.1103/PhysRevB.85.075318

P5: **J.-S. Tempel**, F. Veit, M. Aßmann, L. E. Kreilkamp, S. Höfling, M. Kamp, A. Forchel, and M. Bayer: "*Temperature dependence of pulsed polariton lasing in a GaAs microcavity.*"
New J. Phys. **14**, 083014 (2012).
Available at http://dx.doi.org/10.1088/1367-2630/14/8/083014

P6: J. Schmutzler, F. Veit, M. Aßmann, **J.-S. Tempel**, S. Höfling, M. Kamp, A. Forchel, and M. Bayer: "*Determination of operating parameters for a GaAs-based polariton laser.*"
Submitted for publication (2013).

Acknowledgements

At this point I would like to thank all those who contributed to the research projects presented in this dissertation.

First of all, I wish to thank my advisor Prof. Dr. Manfred Bayer for providing me the opportunity to conduct all the studies in his research group as well as for his ongoing and fruitful support.

I would like to thank all current and former members of the "Correlation Lab" for their support and the productive collaboration during all those project that we achieved together. I owe my deepest gratitude to Dr. Marc Aßmann for innumerable stimulating scientific discussions, support in many technical questions and guidance. Many thanks to Lars Erik Kreilkamp, Benjamin Siebers and Franziska Veit for the great and successful time we spend together on different experimental setups. Also, I am indebted to Johannes Schmutzler for stimulating conversations on the latest results as well as for proofreading.

It is a great pleasure to thank Dr. Ilya A. Akimov for his support and help in many physical and technical questions during the micropillar project. Furthermore, I like to thank very much Dr. Jörg Debus for his many useful advices in various aspects as well as for his professional proofreading of this thesis. Many thanks also to Christian Brüggemann, Lukas Langer and Alexandre René for helpful comments on parts of this thesis.

I gratefully acknowledge the collaboration with the group of Prof. Dr. Alfred Forchel at the university of Würzburg, who provided us excellent microcavity samples. Especially, I would like to thank Prof. Dr. Stephan Reitzenstein and Dr. Sven Höfling for fruitful discussions on our results and for their support during the preparation of publications.

Furthermore, I would like to thank all the colleagues from our research group, the Experimentelle Physik 2, for the open and collaborative environment.

Last but not least, I wish to thank my family for giving me their unequivocal support and care, especially during the last few years.